Microscopic Characterization of Relaxation Behavior in Metallic Glasses

by

Tianjiao Lei

A dissertation submitted in partial fulfillment
of the requirements for the degree of
Doctor of Philosophy
(Materials Science and Engineering)
in the University of Michigan
2020

Doctoral Committee:

Professor Michael Atzmon, Chair
Assistant Professor Yue Fan
Professor Amit Misra
Professor Michael Thouless

Tianjiao Lei

tianjlei@umich.edu

ORCID iD: 0000-0002-1166-2283

Acknowledgements

Even though pursuing a Ph.D. degree is challenging, I am glad that I decided to go on this journey because of the valuable knowledge and experience that I may not obtain from a different path. I am also very grateful for the support from people around me, without which I could not enjoy the journey as much as I have.

Firstly, I show my greatest appreciation to my advisor, Prof. Michael Atzmon, who is a brilliant scientist. During the past five years, he taught me not only the knowledge about my research but also details in English writing/speaking, effective communication/presentation, critical thinking, etc. I am always impressed by the attitude he has towards research – not chasing big topic but doing solid work, which will affect me for my whole life. His guidance is critical to make the project successful.

I am very grateful to my committee members, Prof. Yue Fan, Prof. Amit Misra, and Prof. Michael Thouless for providing valuable comments and suggestions, which are very helpful for improving the project. I also want to thank Prof. Kenneth Kozloff for letting me use the nanoindenter in his lab, Dr. Allen Hunter for his help with atom probe tomography, Ming Liu, Jie Shen, Dr. Yonghao Sun, Prof. Weihua Wang from Chinese Academy of Sciences and Professor A. Lindsay Greer from University of Cambridge for providing samples, performing mechanical tests, and giving insightful

suggestions. In addition, I appreciate Dr. JongDoo Ju's instruction and help at the beginning of this project.

I want to thank Luis Rangel DaCosta, a bright and kind undergraduate student who has been in our lab for more than three years. He helped me develop an automated image analysis and image fitting method, which is a major progress in the present study. In addition, he made a lot of efforts to check spectrum consistency. His contribution is very valuable to the project.

I also want to thank my dear friends – Dr. Qianying Shi, Dr. Feifei Zhang, Dr. Miao Song, Dr. Wenjun Kuang for helping me experimental techniques, Ruiming Lu, Dandan Wang, Jipu Wang, and Yuguo Zhong for giving me confidence, Prof. Shengfeng Guo for giving me advice on my research , and Xin Zhang for his support.

Finally, I would like to thank my family for their endless encouragement and support.

This work and my education were funded by U.S. National Science Foundation (NSF), Grant Nos. DMR-1307884 and DMR-1708043.

Table of Contents

Acknowledgements ii

List of Tables viii

List of Figures ix

List of Appendices xviii

Abstract xx

CHAPTER

1. Introduction 1

1.1 Overview of Relaxation Behavior in Metallic Glasses 1

1.2 References 8

2. Background 10

2.1 Anelastic Deformation 11

2.1.1 Quasi-Static Anelastic Relaxation of an $Al_{86.8}Ni_{3.7}Y_{9.5}$ MG 11

2.1.2 Nonlinearity 16

2.2 Structural Relaxation and Cryogenic Rejuvenation 16

2.3 β Relaxation in Metallic Glasses 19

2.4 References 22

3. Experimental and Analysis Details 24

3.1 Materials 24

3.2 Quasi-Static Anelastic Relaxation 25

3.2.1 Linear Regime at Room Temperature 25

3.2.2 Linear Regime with Thermomechanical Treatment 29

3.2.3 Nonlinear Regime at Room Temperature 30

3.3 Tensile Tests and Dynamic Mechanical Relaxation 32

3.4 Relaxation-Time Spectrum Computation 33

3.5 References 34

4. Shear Transformation Zone Analysis of Anelastic Relaxation of $La_{55}Ni_{20}Al_{25}$ Metallic Glass Reveals Distinct Properties of α and β Relaxations 36

4.1 Introduction 36

4.2 Background 38

4.3 Experimental and Analysis Procedure 40

4.4 Results and Discussion 42

4.5 Conclusions 54

4.6 References 55

5. Microscopic Characterization of Structural Relaxation and Cryogenic Rejuvenation in $La_{70}(Cu_xNi_{1-x})_{15}Al_{15}$, x=0 or 1 Metallic Glasses 57

5.1 Introduction 57

5.2 Experiment and Analysis Procedure 59

5.3 Results and Discussion 62

5.4 Conclusions 72

5.5 References 72

6. Composition Effect on α and β Relaxations for La-based Metallic Glasses from a Viewpoint of Shear Transformation Zone Properties 74

6.1 Introduction 74

6.2 Experimental Details 76

6.3 Results and Discussion 77

6.4 Conclusions 85

6.5 References 85

7. Activation Volume Details from Nonlinear Anelastic Deformation of a Metallic Glass 87

7.1 Introduction 87

7.2 Background 89

7.3 Experimental Details 92

7.4 Overview of the Data Analysis 97

7.5 Analysis Details 98

7.6 Conclusions 105

7.7 Appendix: Symbol Definitions 106

7.8 References 109

8. Summary and Future Work 111

8.1 Summary 111

8.2 Future Work 114

8.2.1 Structural Relaxation Kinetics 114

8.2.2 Effect of Ni vs. Cu on Mechanical Behavior in Different Alloy Systems 116

8.3 References 117

APPENDIX A. Large-Curvature Sample Constraining and Curvature Measurement After Its Release 119

A.1 Experimental Setup for Large-Curvature Constraint 119

A.2 Determination of the Radius of Curvature after Constraint Removal 120

APPENDIX B. MATLAB® Code Commands of Image Digitization for Obtaining the Radius of Curvature of Samples During Constraint-Free Relaxation in the Linear Anelastic Regime 125

B.1 Introduction 125

B.2 Code Commands and Explanation 126

B.3 References 130

APPENDIX C. Details of Time-Constant Spectrum Computation from Anelastic Strain Using CONTIN 131

C.1 Introduction 131

C.2 Overview of CONTIN 132

C.3 The Input File for Spectrum Computation Using CONTIN 135

C.3.1 Sample Input File for the Mandrel Measurements 136

C.3.2 Sample Input File for the Cantilever Bending 145

C.4 References 148

List of Tables

TABLE

4.1 Apparent and actual volume fraction of the largest *potential* STZ type, c_8, for $Al_{86.8}Ni_{3.7}Y_{9.5}$ and $La_{55}Ni_{20}Al_{25}$ MGs with different RT ageing times. τ_8 and c_8 (apparent) are the time constant of $m = 8$ STZs and volume fraction of $m = 8$ *potential* STZs, respectively, obtained from stress-free relaxation spectra following constraining for $2.0 \cdot 10^6$ s. c_8 (apparent) values are underestimated for ageing times $1.0 \cdot 10^7$ s and $2.9 \cdot 10^7$ s. c_8 (actual) is the volume fraction of $m = 8$ *potential* STZs that would be obtained from stress-free relaxation after reaching mechanical equilibrium under constraint. 52

7.1 Parameter definitions in the expression of shear strain rate and activation free energy 91

List of Figures

FIGURE

1.1 Elastic limit vs. Young's modulus for various metals, alloys, metal matrix composites and metallic glasses [11]. Reprinted from Ashby and Greer, Metallic glasses as structural materials, Scr. Mater. 54, 321 (2005), Copyright 2005, with permission from Elsevier. 2

1.2 Schematic illustration of one shear transformation zone with a volume Ω_f under an applied stress σ [15]. Reprinted from Argon, Plastic deformation in metallic glasses, Acta Metall. 27, 47 (1979), Copyright 1979, with permission from Elsevier. 3

1.3 Schematic illustration of the potential energy topography for α and β relaxations [23]. Reprinted from Stillinger, A topographic view of supercooled liquids and glass formation, Science 267, 1935 (1995), with permission from AAAS. 5

2.1 Stress-strain curves of $Zr_{59}Cu_{20}Al_{10}Ni_8Ti_3$ metallic glass at different strain rates under (a) compressive loading and (b) tensile loading [1]. Reprinted from Zhang and Schultz, Difference in compressive and tensile fracture mechanisms of $Zr_{59}Cu_{20}Al_{10}Ni_8Ti_3$ bulk metallic glass, Acta Mater. 51, 1167 (2003), Copyright 2002, with permission from Elsevier. 11

2.2 Normalized anelastic strain vs. time and their corresponding relaxation-time spectra. (a) Nanoindenter cantilever bending under a fixed load of 200 μN. (b) Mandrel measurement in a constraint-free condition after constraining for $2 \cdot 10^6$ s. Both spectra show distinct peaks, and each peak corresponds to one STZ type, numbered as m = 1,…,8 [6]. Reprinted from Ju *et al.*, An

atomically quantized hierarchy of shear transformation zones in a metallic glass, J. Appl. Phys. 109, 053522 (2011), with the permission of AIP publishing. Copyright 2011 AIP Publishing LLC. 13

2.3 Schematic illustration of the standard linear solid model. The spring with elastic modulus E_0 represents the elastic matrix, while each Voigt unit corresponds to one STZ type. E'_m and η'_m are the effective modulus and shear viscosity of *m*-type STZs, respectively [6]. Reproduced from Ju *et al.*, An atomically quantized hierarchy of shear transformation zones in a metallic glass, J. Appl. Phys. 109, 053522 (2011), with the permission of AIP Publishing. Copyright 2011 AIP Publishing LLC. 14

2.4. STZ properties for $Al_{86.8}Ni_{3.7}Y_{9.5}$ MG. (a) Time constants, τ_m, (b) STZ volume, Ω_m, normalized by the atomic volume of Al, V_{Al}, and (c) Volume fraction of *potential* STZs, c_m, for each STZ type *m* [6]. Reprinted from Ju *et al.*, An atomically quantized hierarchy of shear transformation zones in a metallic glass, J. Appl. Phys. 109, 053522 (2011), with the permission of AIP Publishing. Copyright 2011 AIP Publishing LLC. 14

2.5 Relaxation-time spectra for as-quenched and structurally relaxed $Al_{86.8}Ni_{3.7}Y_{9.5}$ MG, computed from normalized anelastic relaxation strain vs. time [16]. Reprinted with permission from Atzmon and Ju, Microscopic description of flow defects and relaxation in metallic glasses, Phys. Rev. E 90, 042313 (2014), Copyright 2014 by the American Physical Society. 17

2.6 Two scanning electron micrographs of (a) a notched sample and (b) an unnotched sample, both compressed to 0.2 axial strain for a Zr-based BMG. The scale bars in (a) and (b) are 200 μm and 500 μm, respectively [18]. Reprinted with permission from Pan *et al.*, Extreme rejuvenation and

softening in a bulk metallic glass, Nat. Commun. 9, 560 (2018), Copyright 2018 by Springer Nature. 18

2.7 Comparison of normalized loss modulus vs. temperature between different MGs. The newly developed La-MG exhibits a pronounced β relaxation [23]. Reprinted with permission from Yu *et al.*, Tensile plasticity in metallic glasses with pronounced β relaxations, Phys. Rev. Lett. 108, 015504 (2012), Copyright 2012 by the American Physical Society. 21

2.8 Normalized loss modulus as a function of temperature scaled by T_g [27]. (a) $La_{70}(Cu_xNi_{1-x})_{15}Al_{15}$, x=0, 0.5, 0.67, and 1, (b) $Pd_{40}(Cu_xNi_{1-x})_{30}Ni_{10}P_{20}$, x=0 or 1. Reprinted with permission from Yu *et al.*, Chemical influence on β-relaxations and the formation of molecule-like metallic glasses, Nat. Commun. 4, 2204 (2013), Copyright 2013 by Springer Nature. 22

3.1. (a) Schematic illustration of nanoindenter cantilever bending measurements. A fixed load *P* is applied, and the time-dependent vertical displacement, *h*(*t*), is monitored. The horizontal distance between the indent spot and clamp is *L*. Redrawn from Ref. [4]. (b) Loading function for one measurement cycle – a high load of 200 μN for 200 s to obtain the strain vs. time data, and a low load of 2 μN for another 200 s to check reversibility. 26

3.2. Schematic illustration of the bend-relaxation ("mandrel") measurements. A sample with an initial radius of curvature, r_0, is constrained around a mandrel with a radius *R* for $2.0 \cdot 10^6$ s, then relaxed constraint-free. The evolution in radius of curvature of the sample, *r*(*t*), is monitored. Redrawn from Ref. [4]. 27

3.3. (a) Photograph showing one sample during stress-free relaxation along with a stage micrometer for length calibration. (b) Nonlinear curve fit for the data points corresponding to the sample, obtained through image digitization. 28

3.4. Schematic illustration of the thermomechanical treatment and measurement sequence [6]. Reprinted from Lei *et al.*, Microscopic characterization of structural relaxation and cryogenic rejuvenation in metallic glasses, Acta Mater. 164, 165 (2019), Copyright 2018, with permission from Elsevier. 29

3.5 Constraining setup for the nonlinear-regime mandrel measurement. A vise is used to apply load on the constraining component – a sample placed between a mandrel and neoprene block, and a machined device to press the mandrel until two constraint-free ends of the sample just touching each other. A peephole on the side surface is used to observe the two touching ends during constraining, and one photograph showing the two touching ends of a sample under constraint is in the upper-right corner. 30

3.6. Sample geometry (a) under constraint (the small curvature of the free ends is neglected), (b) during unconstrained relaxation (not to scale). $\alpha(t)$ is used to determine the evolution of the curvature of the previously bent section during unconstrained relaxation. The length of constrained section (red) equals $(\pi+\varphi)\times(R+d/2)$, where R is the mandrel radius and d is the sample thickness. Dashed lines are fits to the unconstrained ends. 32

4.1. Schematic illustration of (a) nanoindenter cantilever bending and (b) bend relaxation ("mandrel"). For the former, a fixed load P is applied on the sample for 200 s. The vertical displacement, h, is monitored as a function of time. For the latter, the sample is constrained around a mandrel with a radius R for $2.0\cdot10^6$ s, then relaxed stress-free for up to $3.2\cdot10^7$ s, while monitoring the evolution of radius of curvature, $r(t)$. 41

4.2. Anelastic bending strain at the surface normalized by equilibrium elastic strain vs. measurement time, of $La_{55}Ni_{20}Al_{25}$ ribbons with different RT ageing times: a) nanoindenter

cantilever bending. Each curve corresponds to an average of all samples with the same ageing condition, and each point is an average of every 500 experimental data points, b) mandrel measurements. Data for all samples are shown, and dashed lines have the same slope. 43

4.3. Normalized anelastic strain from mandrel measurements at four measurement times, t_i, as a function of prior RT ageing time, t_a. 45

4.4. Relaxation-time spectra of $La_{55}Ni_{20}Al_{25}$ with different RT ageing times. Distinct peaks are observed and labeled m=1,…8. (a) Nanoindenter cantilever bending. Each curve corresponds to an average of all samples at the same ageing condition; (b) Mandrel measurements – two representative curves are shown for each RT ageing time. The spectra are shifted upwards for clarity. $m \leq 5$ peaks correspond to the β relaxation, and $m \geq 6$ to the α relaxation. 46

4.5 (a) Relaxation time constant (τ_m) of each STZ type (m) for different RT ageing times. (b) Relaxation time constants as a function of RT ageing time of different STZ types. Dashed lines are power-law fits. 48

4.6 STZ volume (Ω_m) as a function STZ type (m) for samples aged $2.9 \cdot 10^7$ s. The error bars, < 0.7%, are smaller than the symbols. The slopes correspond to the volume increment between two adjacent Ω_m values. The random error in these slopes is 2-3%. 49

4.7 Calculated evolution of shear modulus (μ) during RT structural relaxation. The abscissa is a sum of RT ageing time and half of measurement time, a rough estimate necessary since samples undergo structural relaxation during the measurement, and both the ageing time and measurement time are of similar orders of magnitude. 51

4.8. Volume fraction occupied by m-type *potential* STZs, Eq. (4.3), as a function of activation free energy ΔF_m, Eq. (4.1), divided by kT, for different RT ageing times. Each symbol corresponds to

one ageing-time value. The error bars for $\Delta F/kT$ are smaller than the symbols. Arrows show the direction of evolution with RT ageing for each m. m = 6-8 and beyond (not active at RT within the time range used) correspond to the α relaxation, and $m \leq 5$ correspond to the β relaxation. The last two data points for m = 8 STZs represent an underestimate due to lack of mechanical equilibration at the end of the constraining period for samples with long ageing time and associated long τ_8 values (see discussion). 51

5.1. Schematic illustration of the thermomechanical treatment and measurement sequence. 60

5.2. Normalized anelastic strain of $La_{70}Cu_{15}Al_{15}$ and $La_{70}Ni_{15}Al_{15}$ as a function of time for different ageing times prior to bending, as indicated. Open circles and filled squares correspond, respectively, to measurements without and with cryogenic cycling after ageing, prior to bending. Curves are not shifted. The dashed lines are all drawn with the same slope. Note that the entire strain is anelastic, as verified by annealing at temperature above RT (bold arrow). 62

5.3. Relaxation-time spectra for $La_{70}Cu_{15}Al_{15}$ and $La_{70}Ni_{15}Al_{15}$ with different ageing times, as indicated. For each condition, representative data for two independent samples are shown. Open circles and crosses, vs. filled squares and pluses, correspond to samples without, vs. with, cryogenic cycling, respectively. The curves are shifted vertically for clarity. 65

5.4. c_{total}, the integrated area of the entire spectrum plus the constant in the spectrum fit, $c_{5,6}$, the integrated area of the last two peaks and c_∞ vs. aging time for $La_{70}Cu_{15}Al_{15}$ and $La_{70}Ni_{15}Al_{15}$ MGs. Lines are a guide to the eye. 67

5.5 The evolution of time constants of different STZ types, m, with ageing time for $La_{70}Cu_{15}Al_{15}$ and $La_{70}Ni_{15}Al_{15}$ MGs. Arrows indicate the effect of cryogenic cycling. 69

6.1. Anelastic strain normalized by the corresponding equilibrium elastic strain vs. time for (a) cantilever bending and (b) mandrel measurements of $La_{70}Cu_{15}Al_{15}$ (crosses, circles and triangles) and $La_{70}Ni_{15}Al_{15}$ (pluses and squares) with a RT ageing time of $3.0 \cdot 10^7$ s. For nanoindenter cantilever, each curve is an average of all tests for the same composition, and each point is an average of every 500 experimental data points. For mandrel measurements, curves corresponding to all samples are shown. 77

6.2. Relaxation-time spectra computed from the normalized anelastic strain vs. time data in Fig. 6.1, of $La_{70}Cu_{15}Al_{15}$ (crosses, circles, and triangles) and $La_{70}Ni_{15}Al_{15}$ (pluses and squares) aged at RT for $3.0 \cdot 10^7$ s, for (a) cantilever bending, and (b) mandrel measurements. For cantilever bending, an average of all spectra is shown for each alloy, while all spectra are shown for mandrel measurements. Peaks are number as m=1,…,8, corresponding to different STZ types. 78

6.3. (a) Relaxation time constants (τ_m), obtained as median of the spectrum peak, for each STZ type (m) for $La_{70}Cu_{15}Al_{15}$ (crosses and circles) and $La_{70}Ni_{15}Al_{15}$ (pluses and squares) aged at RT for $3.0 \cdot 10^7$ s. (b) STZ volume (Ω_m) for each STZ type (m) for $La_{70}Cu_{15}Al_{15}$ and $La_{70}Ni_{15}Al_{15}$, aged at RT for $3.0 \cdot 10^7$ s. m = 1,…,4 (crosses and pluses) correspond to cantilever measurements, while m = 4,…,8 (circles and squares) correspond to mandrel measurements. 81

6.4. Volume fraction of *potential* STZs for $La_{70}Cu_{15}Al_{15}$ (crosses and circles) and $La_{70}Ni_{15}Al_{15}$ (pluses and squares) with a RT ageing time of $3.0 \cdot 10^7$ s as a function of activation free energy for shear transformation divided by kT. The error bars for ΔF/kT are smaller than the symbol. For m=4, the cantilever bending and mandrel measurements yield slightly different values of c_m and ΔF/kT, which may be due to the limitation of the standard linear solid model used for the analysis. 83

7.1. Schematic illustration of the standard linear solid model employed – a spring with Young's modulus E_0 in series with Voigt units, each of which represents one STZ size. E'_m and η'_m are the effective Young's modulus and effective viscosity, respectively, of *m*-type STZs, where m = 1-8 for the range of time values in the experiment [12]. Reproduced with permission from Ju *et al.*, J. Appl. Phys. 109, 053522 (2011). Copyright 2011 AIP Publishing LLC. 89

7.2 (a) Schematic illustration of the constraining method – the sample is placed between a mandrel and neoprene block, and a machined device is used to press the mandrel until two stress-free ends of the sample just touching each other. (b) Photograph showing the two touching ends of a sample under constraint. 93

7.3. Sample geometry (a) under constraint, (b) during unconstrained relaxation (not to scale). $\alpha(t)$ is used to determine the evolution of the curvature of the previously bent section during unconstrained relaxation. The length of the constrained section (red) is equal to $(\pi + \varphi) \times (R + d/2)$, where R is the mandrel radius, and d is the sample thickness. Dashed lines are fits to the unconstrained ends. The small curvature of the free ends is neglected in these plots. 95

7.4. Apparent anelastic strain after unconstrained relaxation for $t = 4\times10^6$ s as a function of the apparent elastic strain at the end of the constraining period for varying constraining radii. Both are computed for the sample surface. Each symbol represents one sample. Deviation from linearity occurs at high strain. The dashed line is a fit to the linear portion. 97

7.5. Data of Fig. 7.4 on a log-log scale. Comparison between the two-parameter fit (dotted) and two-step fit (dashed). The latter yields a better fit for the small-strain data than the former. 103

A.1 Constraining setup for the nonlinear-regime mandrel measurement. A vise is used to apply load on the constraining component – a sample placed between a mandrel and neoprene block, and

a machined device to press the mandrel until two constraint-free ends of the sample just touching each other. A peephole on the side surface is to observe the two touching ends during constraining. One photograph of the two touching ends of one sample under constraint is shown in the upper-right corner. 120

A.2 Sample geometry (a) under constraint (the small curvature of the free ends is neglected), (b) during constraint-free relaxation (not to scale). $\alpha(t)$ is used to determine the evolution of the radius of curvature of the previously bent section during constraint-free relaxation. The length of the constrained section (red) is equal to $(\pi + \varphi) \times (R + d/2)$, where R is the mandrel radius, and d is the sample thickness. Dashed lines are fits to the free ends. 120-121

B.1 Schematic illustration of mandrel measurements. A sample was constrained around a mandrel of a radius R for $2.0 \cdot 10^6$ s, then relaxed constraint-free for up to one year. The evolution of radius of curvature at time t after constraint removal, $r(t)$, was monitored. 126

C.1 Screenshot of one sample output file. 142

List of Appendices

APPENDIX

A. Large-Curvature Sample Constraining Method and Curvature Measurement After Its Release 119

A.1 Experimental Setup for Large-Curvature Constraint 119

A.2 Determination of the Radius of Curvature after Constraint Removal 120

B. MATLAB® Code Commands of Image Digitization for Obtaining the Radius of Curvature of Samples During Constraint-Free Relaxation in the Linear Anelastic Regime 125

B.1 Introduction 125

B.2 Code Commands and Explanation 126

B.3 References 130

C. Details of Time-Constant Spectrum Computation from Anelastic Strain Using CONTIN 131

C.1 Introduction 131

C.2 Overview of CONTIN 132

C.3 The Input File for Spectrum Computation Using CONTIN 135

C.3.1 Sample Input File for the Mandrel Measurements 136

C.3.2 Sample Input File for the Cantilever Bending 145

C.4 References 148

Abstract

Metallic glasses (MGs) show high strength and elastic limit, but they also exhibit little macroscopic plasticity, which limits their structural applications. The main reason is strain localization within dominant shear bands. Because of the amorphous structure of MGs, it is challenging to define defects that accommodate deformation. Observations in physical analogs have shown that macroscopic deformation of MGs is accommodated by cooperative shearing of atomic clusters, termed shear transformation zones (STZs). At small strains, STZs are isolated. They can be reversed by back stress in the elastic matrix upon removal of the applied stress, which results in anelastic behavior.

The common observation of a main (α) relaxation, and high-frequency (β) relaxation in mechanical spectroscopy is readily explained in molecular glasses, but their microscopic mechanisms in MGs are still not clear. Recently, the intensity of the β relaxation has been correlated with macroscopic plasticity of MGs. One goal of the present project is to use anelasticity to characterize the STZ spectra of La-based MGs with and without a pronounced β relaxation, and to study the α vs. β relaxation and structural relaxation vs. cryogenic cycling from a microscopic view. $La_{55}Ni_{20}Al_{25}$ and $La_{70}(Ni_xCu_{1-x})_{15}Al_{15}$, x=0,1 MGs have been investigated. The results suggest that the chemical composition of STZs corresponding to α vs. β relaxation is different, indicated by two regimes of STZ activation volume. Room-temperature structural relaxation only affects the larger/slower STZs (corresponding to α relaxation) by decreasing the number of the corresponding *potential*

STZs (i.e., atomic clusters capable of shear transformation) while increasing the relaxation time constants. A detailed description of structural relaxation emerges: its dominant effect is on the largest, and therefore slowest, STZs observed in the present kinetics window. Cycling between liquid-nitrogen temperature and room temperature reverses the increasing time constants due to structural relaxation in $La_{70}(Ni_xCu_{1-x})_{15}Al_{15}$, x=0,1, pointing to a rejuvenation effect. However, cycling does not significantly affect the anelastic behavior. The pronounced β peak observed in normalized loss modulus of $La_{70}Ni_{15}Al_{15}$ but not $La_{70}Cu_{15}Al_{15}$ is a result of *both* larger volume fraction of fast and small *potential* STZs *and* smaller volume fraction of slow and larger *potential* STZs in $La_{70}Ni_{15}Al_{15}$ vs. $La_{70}Cu_{15}Al_{15}$.

Another focus of the present project is the nonlinear anelastic relaxation in MGs under high stress, for which the viscosity is non-Newtonian, and therefore the rate of anelastic relaxation is not linear in the applied stress. In this regime, the details of the activation volume, not available in the linear regime, can be obtained. Despite the complicated stress state due to nonlinearity, bending allows for stable measurements for a long period. A method of controlled sample bending to a strain of up to ~ 0.0155 has been developed, and applied to $Al_{86.8}Ni_{3.7}Y_{9.5}$ MG. Significant nonlinearity of the anelastic strain in the stress was observed, which is mainly associated with the largest and slowest active STZs not reaching mechanical equilibrium at the end of the constraining period. Combining nonlinear kinetics under constraint and zero bending moment after constraint removal, the volume of the largest active STZs and the transformation shear strain were obtained independently for the inherent state – their most likely values are 4.8×10^{-28} m^3 and 0.18, respectively.

CHAPTER 1
Introduction

1.1 Overview of Relaxation Behavior in Metallic Glasses

Metallic glasses (MGs) are amorphous alloys cooled from the melt by bypassing crystallization. They exhibit attractive properties, such as low coercivity [1], good corrosion resistance [2], and high room-temperature strength and elastic limit [3], which have considerably potential applications [4]. Early MGs were obtained from the liquid at high cooling rates, ~ 10^5 to 10^7 K/s, and therefore only thin ribbons with thickness less than 0.05 mm were produced [5]. In the past, the main technique to produce them was melt-spinning, during which a molten alloy was injected onto a rapidly rotating substrate surface, resulting in a cooling rate on the order of 10^5 to 10^6 K/s [6].

Alloy systems with easy MG formability can give rise to large-dimension samples – bulk metallic glasses (BMGs) [7]. The maximum achievable sample thickness increases with increasing ratio of glass transition temperature (T_g) to melting temperature (T_m) [8]. Empirical rules for easy glass-forming systems have been reported [9]: 1) three or more alloying elements, 2) significant atomic size mismatch that gives rise to higher packing density and smaller free volume, 3) negative heat of mixing among the main elements, and 4) alloy composition close to a deep eutectic. Following these rules, the required cooling rate was reduced to 10^{-1}-10^2 K/s, and BMGs with experimental

diameter as large as 80 mm have been successfully produced [10]. The development of BMGs is significant for both fundamental studies and engineering applications.

One promising application for MGs is as structural materials because of their high elastic limit and strength, as shown in Fig. 1.1 [11]. However, they show little macroscopic plasticity due to strain localization within dominant shear bands, which is a major limitation. Extensive studies have been conducted to investigate the deformation behavior of MGs [12,13,14]. Unlike crystalline materials, in which the deformation mechanism is well studied in terms of the lattice defects with the help of electron microscopy techniques, it is challenging to directly observe the atomic structure of MGs due to their amorphous nature, let alone correlating it to their mechanical properties. Based on physical analogs [15,16], the deformation of MGs is believed to be accommodated by cooperative shearing of atomic clusters termed shear transformation zones (STZs) (Fig. 1.2). At small strain,

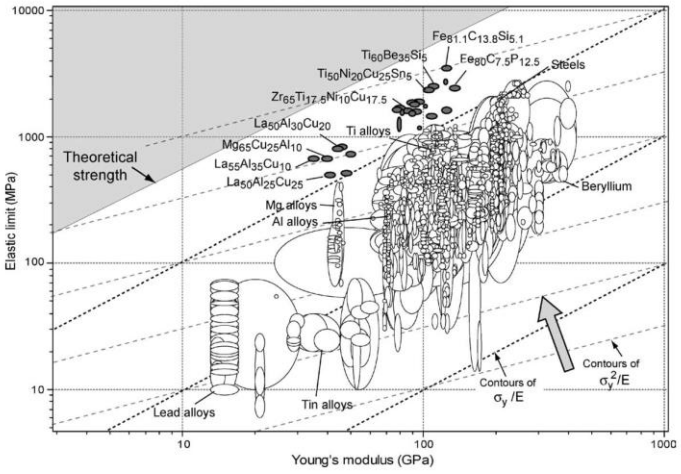

Figure 1.1. Elastic limit vs. Young's modulus for various metals, alloys, metal matrix composites and metallic glasses [11]. Reprinted from Ashby and Greer, Metallic glasses as structural materials, Scr. Mater. 54, 321 (2005), Copyright 2005, with permission from Elsevier.

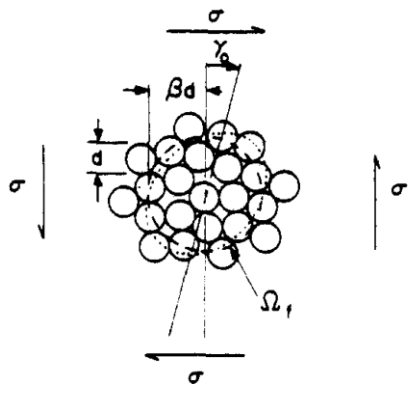

Figure 1.2. Schematic illustration of one shear transformation zone with a volume Ω_f under an applied stress σ [15]. Reprinted from Argon, Plastic deformation in metallic glasses, Acta Metall. 27, 47 (1979), Copyright 1979, with permission from Elsevier.

STZs are isolated, and the overall strain can be reversed upon removal of the external applied stress, due to back stress in the elastic matrix, which leads to anelastic deformation. For a sufficiently small applied stress, the anelastic strain rate and equilibrium anelastic strain are linear in it. With increasing stress, nonlinear anelastic deformation, i.e., non-Newtonian behavior, occurs, which offers a chance to independently obtain the STZ volume and transformation shear strain [17]. Above a stress threshold, STZs begin to interact with each other as a result of their decreasing separation, and back stress in the elastic matrix is lost, resulting in plastic deformation.

Although the STZ theory is commonly employed when describing plastic deformation for MGs, the properties for STZs are still under debate. Various STZ sizes, ranging from a few to several hundred of atoms, have been reported from both experiments and simulations. Choi *et al.* [18] performed nanoindentation measurements with a fixed loading rate at room temperature (RT) on a Zr-based BMG, and obtained an STZ size of ~ 25 atoms using a cooperative shear model proposed by Johnson and Samwer [19]. Ju *et al.* [20] conducted RT quasi-static anelastic relaxation

measurements on an Al-based MG by employing nanoindenter cantilever bending and bend relaxation techniques. Relaxation-time spectra were computed from the anelastic strain vs. time data, which yielded a quantized hierarchy of STZs ranging from 14 to 21 atoms in size, based on a standard linear solid model. On the other hand, also using nanoindentation measurements, Pan *et al.* [21] reported STZ sizes of hundreds of atoms for various MG systems by using the cooperative shear model [19]. However, their result was an overestimate due to strain localization and shear band formation in their measurements. In addition, we speculate that the universal macroscopic yield strain in the cooperative shear model is smaller than the theoretical limit, which results in a larger STZ size. For simulations, Fan *et al.* [22] employed an activation-relaxation technique, and showed an STZ size of typically less than ten atoms under thermally activated deformation. Therefore, the identification of STZ size is still elusive.

When cooling through T_m sufficiently rapidly, the liquid becomes supercooled, and continuing cooling leads to freezing at T_g. Stillinger [23] pointed out that during the cooling process, a single peak in frequency of (e.g., mechanical, electrical, thermal, optical) relaxation in the equilibrium liquid (and moderately supercooled regime) splits into a pair of maxima when approaching T_g, corresponding to primary α and secondary faster β relaxations. He further interpreted these two relaxations in term of the potential energy landscape – suggesting that the β relaxation corresponds to the elementary relaxations between neighboring basins, whereas the α relaxation is the transition between two metabasins, as shown in Fig. 1.3. For molecular glasses, Johari and Goldstein [24] attributed α vs. β relaxations to intermolecular vs. intramolecular processes. However, such a distinction is inapplicable in MGs. As a result, the nature of the α and β relaxations in MGs is still poorly understood.

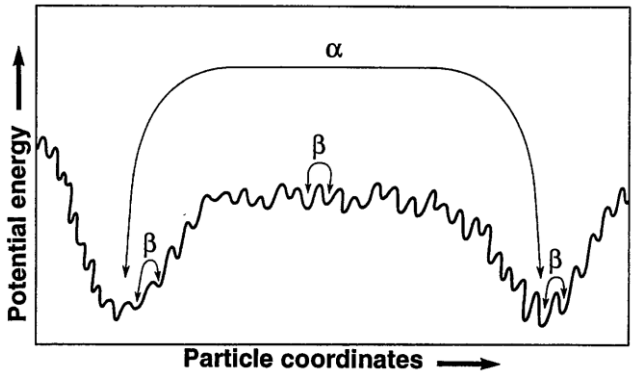

Figure 1.3. Schematic illustration of the potential energy topography for α and β relaxations [23]. Reprinted from Stillinger, A topographic view of supercooled liquids and glass formation, Science 267, 1935 (1995), with permission from AAAS.

In general, the α relaxation is described as the mechanism of viscous flow, which defines the glass transition, and is commonly believed to be kinetically frozen below T_g. However, recent work [20] shows that it can be observed below T_g when employing a sufficient long timescale. The β relaxation is essential to understand fundamental processes in the sub-T_g regime [25]. To study the β relaxation, dynamic mechanical analysis (DMA) [26] is the most commonly used technique, which determines the loss modulus, the imaginary part of complex modulus, at either a fixed temperature with varying frequency or vice versa. In DMA, the α relaxation manifests as a dominant peak in the loss modulus at high temperature and/or low frequency, while the β relaxation exhibits as either an excess wing/shoulder or a distinct peak at low temperature and/or high frequency. The β relaxation has been argued to originate from a different mechanism than that of the α relaxation [27], based on a discrepancy between experimental data and a stretched exponential relaxation–Kohlrausch-Williams-Watts (KWW) function [28]. However, the application of KWW to anelastic relaxation well below T_g is phenomenological, and often results in inconsistent fitting parameters [29]. For an Al-based MG, Ju and Atzmon showed that both the

α and β relaxations can be explained with a single, atomically quantized STZ hierarchy: the former results from large and slow STZs, while small and fast STZs lead to the latter [30]. A similar conclusion was obtained for the dynamic-mechanical response of a Zr-based alloy [31].

Since MGs are metallic solids with frozen-in melt structure, they undergo thermally activated structural relaxation toward an internal equilibrium state. Many physical properties change during structural relaxation, such as decreasing atomic diffusivity [32], increasing viscosity [33] and Young's modulus [34]. Some of the changes are undesirable from the viewpoint of applications. For example, Kumar *et al.* [35] reported annealing-induced embrittlement for a Zr-based MG – the fracture strain decreased from 7.5% to 2% after sub-T_g annealing for 1 h. This makes structural applications of MGs more challenging, given that many as-quenched MGs do not possess much plasticity. On the other hand, the plasticity can be improved by rejuvenation through various methods, such as constrained loading [36], irradiation [37], and cryogenic cycling [38]. Therefore, understanding the mechanism of structural relaxation and rejuvenation is essential for both fundamental and practical reasons.

This dissertation focuses on the microscopic mechanism of α vs. β relaxation in La-based MGs by using anelastic relaxation measurements combined with the standard linear solid model analysis [39]. Then, these are used to characterize room-temperature structural relaxation and its reversal – rejuvenation by cryogenic cycling. In addition, the nonlinear anelastic deformation for an Al-based MG is also studied. The two main experimental techniques employed are nanoindenter cantilever bending for short-time measurements and bend relaxation for longer-time measurements, to

observe RT quasi-static anelastic strain relaxation over ten orders of magnitude in time. Subsequently, time-constant spectra are computed from the strain data. Both the measurement techniques and computation methods are discussed in Chapter 3.

As in the previous study for an-Al based MG by Ju *et al.* [20], for the present La-based MGs, distinct peaks emerge from the spectra, corresponding to a quantized hierarchy of STZs. While the STZ volume exhibits a smooth transition between the regimes corresponding to α and β relaxations, the properties of STZs associated with α vs. β are different: The latter exhibits a smaller volume increment than the former, indicating a possible chemical composition difference between the STZs corresponding to the two relaxation modes, as discussed in Chapter 4. After charactering the α and β relaxations by employing the time-constant spectrum, the effects of both RT ageing and cryogenic cycling have been studied using similar approaches. The results show that RT ageing does not significantly affect the properties of the STZs corresponding to β relaxation. However, it increases the relaxation time constants of the STZs corresponding to α relaxation, while decreasing the volume fractions of their corresponding *potential* STZs (PSTZs), i.e., atomic clusters that are capable of shear transformation. The increased time constants are reversed by cryogenic cycling, pointing to a rejuvenation effect, but the volume fractions are unaffected. The details of RT structural relaxation and cryogenic rejuvenation are discussed in terms of STZ properties in Chapter 5. By comparing two alloy systems with and without a pronounced β relaxation, it is proposed that the relative strong β relaxation peak is associated with *both* larger volume fraction of fast and small PSTZs *and* smaller volume fraction of slow and large PSTZs, as elaborated in Chapter 6.

All the anelastic relaxation measurements in Chapters 4-6 are in the linear regime, i.e., the shear strain rate is linear in the applied stress. At higher strain, the viscosity is non-Newtonian under constraint, and an independent determination of the STZ volume and transformation shear strain is obtained in Chapter 7. Chapter 8 includes conclusions and suggestions for future work.

1.2 References

[1.1] T. D. Shen and R. B. Schwarz, *Appl. Phys. Lett.* **75**, 49 (1999).

[1.2] S. J. Pang, T. Zhang, K. Asami, and A. Inoue, *Acta Mater.* **50**, 489 (2002).

[1.3] A. Inoue, B. Shen, H. Koshiba, H. Kato, and A. R. Yavari, *Nat. Mater.* **2**, 661 (2003).

[1.4] G. Kumar, A. Desai, and J. Schroers, *Adv. Mater.* **23**, 461 (2011).

[1.5] A. Inoue and A. Takeuchi, *Mater. Trans.* **43**, 1892 (2002).

[1.6] H. H. Liebermann, *Mater. Sci. Eng.* **43**, 203 (1980).

[1.7] Z. P. Lu, Y. Li, and S. C. Ng, *J. Non-Cryst. Solids* **270**, 103 (2000).

[1.8] A. Inoue, *Mater. Trans. JIM* **36**, 866 (1995).

[1.9] A. Inoue, *Acta Mater.* **48**, 279 (2000).

[1.10] A. Inoue, N. Nishiyama, and H. Kimura, *Mater. Trans. JIM* **38**, 179 (1997).

[1.11] M. F. Ashby and A. L. Greer, *Scr. Mater.* **54**, 321 (2006).

[1.12] W. J .Wright, R. Saha, and W. D. Nix, *Mater. Trans.* **42**, 642 (2001).

[1.13] J. Lu, G. Ravichandran, and W. L. Johnson, *Acta Mater.* **51**, 3429 (2003).

[1.14] U. Ramamurty, S. Jana, Y. Kawamura, and K. Chattopadhyay, *Acta Mater.* **53**, 705 (2005).

[1.15] A. S. Argon, *Acta Metall.* **27**, 47 (1979).

[1.16] P. Schall, D. A. Weitz, and F. Spaepen, *Science* **318**, 1895 (2007).

[1.17] A. S. Argon and L. T. Shi, *Acta Metall.* **31**, 499 (1983).

[1.18] I.-C. Choi, Y. Zhao, Y. -J. Kim, B. -G. Yoo, J.-Y Suh, U. Ramamurty, and J. -I Jang, *Acta Mater.* **60**, 6862 (2012).

[1.19] W. L. Johnson and K. Samwer, *Phys. Rev. Lett.* **95**, 195501 (2005).

[1.20] J. D. Ju, D. Jang, A. Nwankpa, and M. Atzmon, *J. Appl. Phys.* **109**, 053522 (2011).

[1.21] D. Pan, A. Inoue, T. Sakurai, and M. W. Chen, *Proc. Natl. Acad. Sci. U.S.A.* **105**, 14769 (2008).

[1.22] Y. Fan, T. Iwashita, and T. Egami, *Nat. Commun.* **5**, 5083 (2014).

[1.23] F. H. Stillinger, *Science* **267**, 1935 (1995).

[1.24] G. P. Johari and M. Goldstein, *J. Chem. Phys.* **53**, 2372 (1970).

[1.25] H. B. Yu, W. H. Wang, H. Y. Bai, and K. Samwer, *Mater. Today* **16**, 183 (2013).

[1.26] J. C. Qiao and J. M. Pelletier, *J. Mater. Sci. Technol.* **30**(6), 523 (2014).

[1.27] Q. Wang, S. T. Zhang, Y. Yang, Y. D. Dong, C.T. Liu, and J. Lu, *Nat. Commun.* **6**, 7876 (2015).

[1.28] B. Ruta, Y. Chushkin, G. Monaco, L. Cipelletti, V. M. Giordano, E. Pineda, and P. Bruna, *AIP Conf. Proc.* **1518**, 181 (2013).

[1.29] M. Atzmon, *J. Appl. Phys.* **123**, 065103 (2018).

[1.30] J. D. Ju and M. Atzmon, *MRS Commun.* **4**, 63 (2014).

[1.31] J. D. Ju and M. Atzmon, *Acta Mater.* **74**, 183 (2014).

[1.32] H. S. Chen, L. C. Kimerling, J. M. Poate, and W. L. Brown, *Appl. Phys. Lett.* **32**, 461 (1978).

[1.33] S. S. Tsao and F. Spaepen, *Acta Metall.* **33**, 881 (1985).

[1.34] H. S. Chen, *J. Appl. Phys.* **49**, 3289 (1978).

[1.35] G. Kumar, D. Rector, R. D. Conner, and J. Schroers, *Acta Mater.* **57**, 3572 (2009).

[1.36] J. Pan, Y. X. Wang, Q. Guo, D. Zhang, A. L. Greer, and Y. Li, *Nat. Commun.* **9**, 560 (2018).

[1.37] J. Heo, S. Kim, S. Ryu, and D. Jang, *Scientific Reports* **6**, 165 (2014).

[1.38] S. V. Ketov, Y. H. Sun, S. Nachum, Z. Lu, A. Checchi, A. R. Beraldin, H. Y. Bai, W. H. Wang, D. V. Louzguine-Luzgin, M. A. Carpenter, and A. L. Greer, *Nature* **524**, 200 (2015).

[1.39] A. S. Nowick and B. S. Berry, Anelastic relaxation in crystalline solids, Academic Press, New York and London, 1972.

CHAPTER 2
Background

Plasticity improvement has been a long-standing focus for metallic glass (MG) studies, since macroscopic brittleness is the major limitation for their structural applications. MGs exhibit little plasticity in compression and almost zero in tension, as shown in Fig. 2.1 [1], and the main reason is shear localization within dominant shear bands due to shear softening [2]. Recently, Greer *et al.* [3] wrote a comprehensive review of shear-banding, including topics such as the shear band initiation and the structural evolution inside shear bands.

While shear-banding has been studied in detail, microscopic details of MG deformation have not been fully explored. In crystalline metals, at low temperature, dislocation gliding is responsible for their plastic deformation. However, the nature of defects in MGs is difficult to determine because of their amorphous structure. Based on experiments with a two-dimensional bubble raft, Argon [4] proposed that the shear of MGs is accommodated by cooperative shearing of atomic clusters, termed shear transformation zones (STZs) [5]. In order to study STZ properties, small-strain anelastic deformation is an ideal regime, since STZs are in the dilute limit and do not interact with each other. Therefore, this section begins with a review of a previous study by Ju *et al.* [6] on linear anelastic relaxation of an Al-based MG, which revealed a quantized hierarchy of STZs and their properties. Then, nonlinear anelastic deformation under higher strain is introduced.

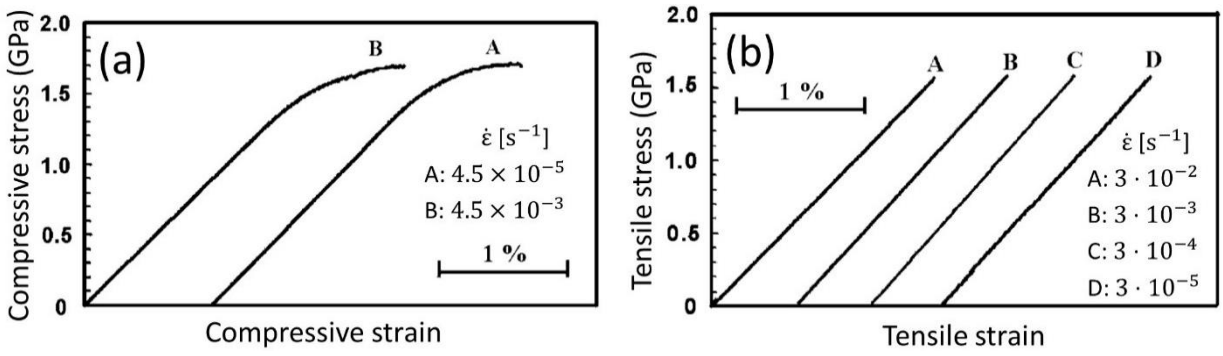

Figure 2.1. Stress-strain curves of $Zr_{59}Cu_{20}Al_{10}Ni_8Ti_3$ metallic glass at different strain rates under (a) compressive loading and (b) tensile loading [1]. Reprinted from Zhang and Schultz, Difference in compressive and tensile fracture mechanisms of $Zr_{59}Cu_{20}Al_{10}Ni_8Ti_3$ bulk metallic glass, Acta Mater. 51, 1167 (2003), Copyright 2002, with permission from Elsevier.

Subsequently, the concepts of structural relaxation and cryogenic rejuvenation are reviewed, motivated by annealing-induced embrittlement [7] and improved plasticity due to cryogenic cycling [8], respectively. Lastly, the two relaxation modes in glasses, α and β, are discussed, motivated by the recent discovery of the correlation among β relaxation, STZ dynamics, and plasticity in MGs [9].

2.1 Anelastic Deformation

2.1.1 Quasi-Static Anelastic Relaxation of an $Al_{86.8}Ni_{3.7}Y_{9.5}$ MG

In a previous study, Ju *et al.* [6] performed quasi-static anelastic relaxation measurements at RT on an $Al_{86.8}Ni_{3.7}Y_{9.5}$ MG by employing both nanoindenter cantilever bending for short-time measurements (~ 1 s to 200 s) and bend relaxation ("mandrel") for longer time (~ 10^3 s to $3 \cdot 10^7$ s). For the former, a fixed load (= 200 μN) was applied for 200 s, during which the vertical displacement was monitored as a function of time. The strain reversibility was confirmed by

following with a small load (= 2 μN). The maximum bending strain at time *t* is attained on the sample surface at the clamp, and expressed as [6],

$$\varepsilon(t) = 3d \cdot h(t)/2L^2, \tag{2.1}$$

where *d* is the cantilever thickness, *h*(*t*) is the time-dependent vertical displacement, and *L* is the effective length. The equilibrium elastic strain, ε_{el}^{0}, is determined from the instantaneous displacement upon loading.

In bend relaxation ("mandrel") measurements, samples were constrained around mandrels of radii ranging from 0.35 to 0.49 cm for a standard time of $2 \cdot 10^6$ s, then relaxed constraint-free for up to $3 \cdot 10^7$ s. The evolution in radius of curvature, *r*(*t*), during constraint-free relaxation was monitored using a digital camera and determined by a visual fitting. The nominal equilibrium elastic strain, reached at the end of the constraining period, and maximum anelastic strain at time *t* after constraint removal, both attained at the surface [6], are

$$\varepsilon_{el}^{0} = d/2 \cdot [1/R - 1/r(0)], \tag{2.2}$$

and,

$$\varepsilon_{an}(t) = d/2 \cdot [1/r(t) - 1/r_0], \tag{2.3}$$

respectively. *d* is the sample thickness, *R* is the mandrel radius, and r_0 is the initial radius of curvature of the sample before constraint.

In Ref. [6], the time-dependent anelastic strain data were used to compute relaxation-time spectra, $f(\tau)$, as a function of relaxation time, τ_i. Figure 2.2 shows the anelastic strain normalized by its corresponding equilibrium elastic strain vs. time from both experimental techniques, along with the corresponding spectra, which exhibited distinct peaks [6]. Each peak was associated with one STZ type, numbered as m = 1,…,8. To analyze the relaxation behavior, a standard linear solid model was employed, as illustrated in Fig. 2.3, which consists of several Voigt units, each corresponding to a spectrum peak and therefore to one STZ type, in series with each other and with a spring. The latter represents the elastic matrix.

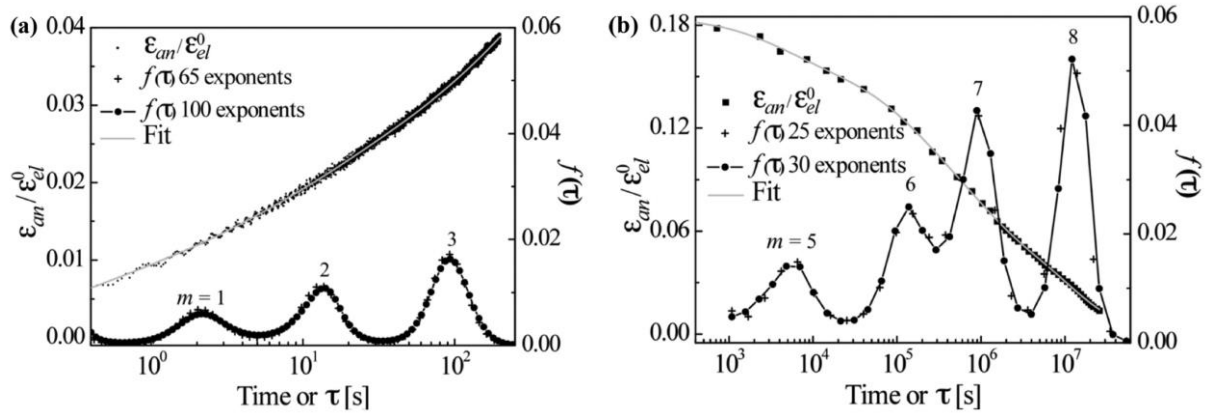

Figure 2.2. Normalized anelastic strain vs. time and their corresponding relaxation-time spectra. (a) Nanoindenter cantilever bending under a fixed load of 200 μN. (b) Mandrel measurement in a constraint-free condition after constraining for $2 \cdot 10^6$ s. Both spectra show distinct peaks, and each peak corresponds to one STZ type, numbered as m = 1,…,8 [6]. Reprinted from Ju *et al.*, An atomically quantized hierarchy of shear transformation zones in a metallic glass, J. Appl. Phys. 109, 053522 (2011), with the permission of AIP Publishing. Copyright 2011 AIP Publishing LLC.

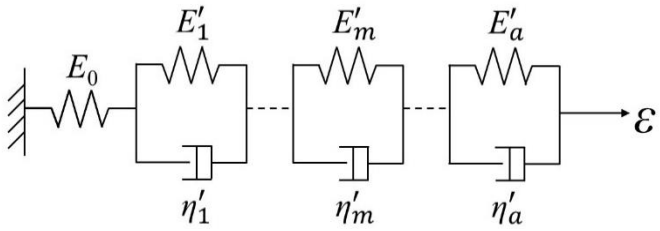

Figure 2.3. Schematic illustration of the standard linear solid model. The spring with elastic modulus E_0 represents the elastic matrix, while each Voigt unit corresponds to one STZ type. E_m' and η_m' are the effective modulus and shear viscosity of *m*-type STZs, respectively [6]. Reproduced from Ju *et al.*, An atomically quantized hierarchy of shear transformation zones in a metallic glass, J. Appl. Phys. 109, 053522 (2011), with the permission of AIP Publishing. Copyright 2011 AIP Publishing LLC.

Figure 2.4 shows the STZ properties, including the relaxation time constant, STZ volume, and volume fraction of *potential* STZs for each STZ type. The relaxation time constant for *m*-type STZs, τ_m, taken as the median of the corresponding spectrum peak, is shown in Fig. 2.4a. Combining the expression for the macroscopic shear strain rate due to *m*-type STZs [4],

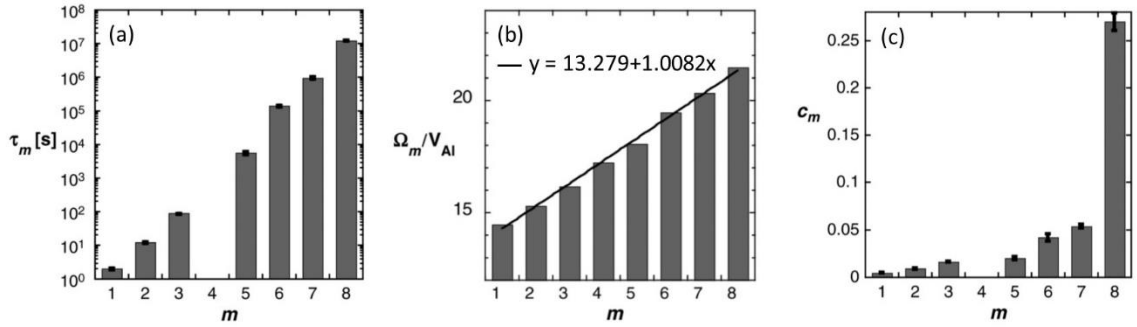

Figure 2.4. STZ properties for $Al_{86.8}Ni_{3.7}Y_{9.5}$ MG. (a) Time constants, τ_m, (b) STZ volume, Ω_m, normalized by the atomic volume of Al, V_{Al}, and (c) Volume fraction of *potential* STZs, c_m, for each STZ type *m* [6]. Reprinted from Ju *et al.*, An atomically quantized hierarchy of shear transformation zones in a metallic glass, J. Appl. Phys. 109, 053522 (2011), with the permission of AIP Publishing. Copyright 2011 AIP Publishing LLC.

$$\dot{\gamma}_m = 2c_m\gamma_o^c\nu_G\exp\left(-\frac{\Delta F_m}{kT}\right)\sinh\left(\frac{\sigma\gamma_0^T\Omega_m}{2kT}\right), \tag{2.4}$$

and the corresponding activation free energy of shear transformation [10],

$$\Delta F_m = \left[\left(\frac{(7-5\nu)}{30(1-\nu)} + \frac{2(1+\nu)}{9(1-\nu)}\bar{\beta}^2\right)\gamma_0^T + \frac{1}{2}\frac{\overline{\sigma_{STZ}}}{\mu}\right]\mu\gamma_0^T\Omega_m, \tag{2.5}$$

τ_m can be expressed as [11],

$$\tau_m = \frac{3\eta_m'}{E_m'} = \frac{1}{\Omega_m\gamma_0^T}\cdot\frac{3kT}{2\mu(1+\nu)\gamma_0^c\nu_G}\cdot\exp\left(\mu\Omega_m\left\{\frac{\gamma_0^T}{kT}\left[\left(\frac{(7-5\nu)}{30(1-\nu)} + \frac{2(1+\nu)}{9(1-\nu)}\bar{\beta}^2\right)\gamma_0^T + \frac{1}{2}\frac{\overline{\sigma_{STZ}}}{\mu}\right]\right\}\right). \tag{2.6}$$

η_m' and E_m' are the effective shear viscosity and effective Young's modulus, respectively, of *m*-type STZs (Fig. 2.3). $\gamma_0^c = [2(4-5\nu)/15(1-\nu)]\gamma_0^T$ is the constrained transformation shear strain, with γ_0^T being the unconstrained value. $\Omega_m\gamma_0^T$ is the activation volume. Based on physical analogs [4,12], $\gamma_0^T = 0.2$ was assumed for all STZs to obtain the *m*-type STZ volume, Ω_m, as shown in Fig. 2.4b. ν_G is the attempt frequency, *k* is the Boltzmann constant, and *T* is the temperature. ν is Poisson's ratio, and $\bar{\beta}^2 \sim 1$ is the dilatancy factor. $\overline{\sigma_{STZ}}$ is the shear resistance of STZs, μ is the shear modulus, and $\overline{\sigma_{STZ}}/\mu = 0.025$ [13].

The volume fraction of *potential* *m*-type STZs, c_m, is equal to the area of the corresponding spectrum peak *m* [6],

$$c_m = \int_m f(\tau)\mathrm{d}\ln\tau = \varepsilon_{an}^m/\varepsilon_{el}^0. \tag{2.7}$$

ε_{an}^m and ε_{el}^0 are the nominally equilibrated anelastic strain due to *m*-type STZs and the equilibrium elastic strain, respectively. For the Al-based MG, c_m increases with *m* (Fig. 2.4c).

2.1.2 Nonlinearity

In Ref. [6], the applied strain is less than 0.005 (< the yield point of MGs, ~ 0.02 [14]), and a linear dependence of the anelastic strain on the applied stress is observed, which implies Newtonian viscosity and therefore a linear anelastic strain profile across the sample thickness. Consequently, there is no residual stress upon constraint removal. In this linear regime, $(\gamma_0^T)^2\Omega_m$ can be determined, but not γ_0^T and Ω_m independently. In Ref. [6], an estimated value of $\gamma_0^T = 0.2$, based on physical analogs [4,12], was used to determine Ω_m values for the Al-based MG, which correspond to 14 to 21 Al atoms for the measurement range. In order to determine γ_0^T and Ω_m independently, it is necessary to perform measurements at higher stress, in the non-Newtonian regime, where the strain rate in Eq. (2.4) is not linear in the applied stress, σ. Such an approach has been reported for $Pd_{80}Si_{20}$ MG for the activated flow state [10]. The authors computed the product of $\gamma_0^T\Omega_f$ from the stress exponent value, m, measured above $0.6T_g$ [15],

$$m = \frac{\sigma\gamma_0^T\Omega_f}{kT}\coth\left(\frac{\sigma\gamma_0^T\Omega_f}{kT}\right), \tag{2.8}$$

and obtained $\gamma_0^T\Omega_f = 1.05 \times 10^{-28}$ m^3. Substituting this value into Eq. (2.5) yielded $\gamma_0^T = 0.135$, and therefore $\Omega_f = 7.77 \times 10^{-28}$ m^3. In Chapter 7, γ_0^T and Ω_m are obtained independently from nonlinear anelasticity measurements, where the STZs are still isolated, unlike in Ref. [10].

2.2 Structural Relaxation and Cryogenic Rejuvenation

Since MGs are metastable, they undergo structural relaxation upon annealing at temperatures below T_g, accompanied by changes in many properties. Due to the disordered atomic structure, it is challenging to characterize structural relaxation in microscopic terms. Recently, Atzmon and Ju

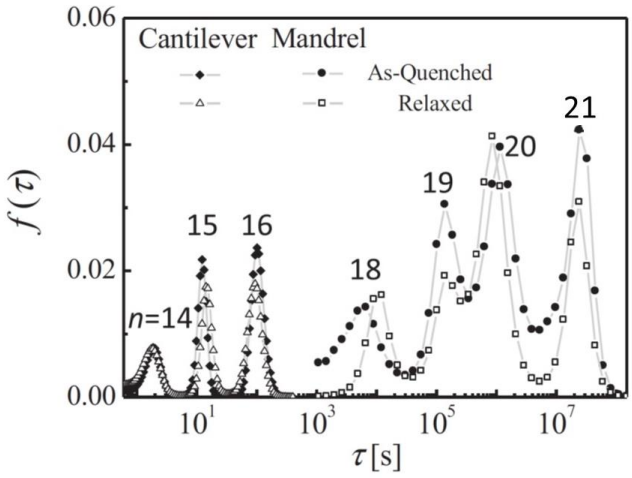

Figure 2.5. Relaxation-time spectra for as-quenched and structurally relaxed $Al_{86.8}Ni_{3.7}Y_{9.5}$ MG, computed from normalized anelastic relaxation strain vs. time [16]. Reprinted with permission from Atzmon and Ju, Microscopic description of flow defects and relaxation in metallic glasses, Phys. Rev. E 90, 042313 (2014), Copyright 2014 by the American Physical Society.

[16] reported that for an $Al_{86.8}Ni_{3.7}Y_{9.5}$ MG, annealing treatment prior to anelastic relaxation measurements only reduced the peak areas of the time-constant spectrum, but left their peak positions unchanged, as shown in Fig. 2.5. They concluded that structural relaxation only decreased the number of *potential* STZs, without changing their properties.

One undesirable effect of the structural relaxation is embrittlement due to annihilation of the "defects" responsible for plastic deformation [17]. On the other hand, plasticity can be enhanced by a rejuvenation process – a reversal of structural relaxation, during which MGs transform to a higher-energy state. Rejuvenation can be achieved by various methods, as reviewed below.

Constrained loading is one approach for plasticity improvement. Pan *et al.* [18] performed compressive tests at RT on notched cylindrical Zr-based BMG samples, and obtained a strain value of up to 0.4. Comparing the scanning electron micrographs of one notched sample and one unnotched sample, both compressed to 0.2 axial strain (Fig. 2.6), the surface of the unnotched sample exhibited shear bands, while the notched sample did not. Differential scanning calorimetry results showed that the maximum stored energy in the deformed notched samples was 66% greater than any previously achieved by plastic deformation.

Plasticity rejuvenation can also be achieved by irradiation. For example, Pt-based MG nanowires exhibit tensile plasticity and quasi-homogeneous plastic deformation after ion irradiation, as compared to brittle-like fracture before irradiation [19]. The authors suggested that ion irradiation increases the fictive temperatures, at which the equilibrium liquid has the same atomic

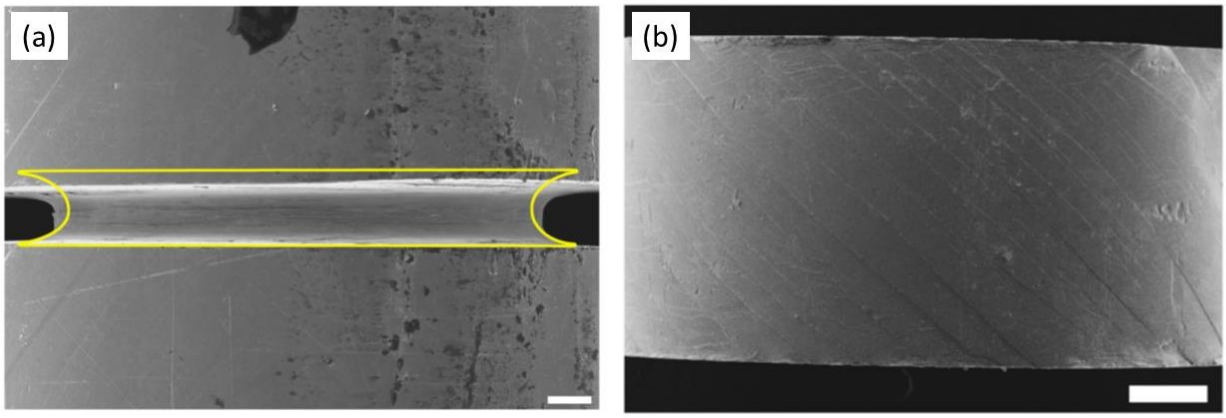

Figure 2.6. Two scanning electron micrographs of (a) a notched sample and (b) an unnotched sample, both compressed to 0.2 axial strain for a Zr-based BMG. The scale bars in (a) and (b) are 200 μm and 500 μm, respectively [18]. Reprinted with permission from Pan *et al.*, Extreme rejuvenation and softening in a bulk metallic glass, Nat. Commun. 9, 560 (2018), Copyright 2018 by Springer Nature.

configuration as that of a glass [20], by tens of degrees – the equivalent of an increase by ten orders of magnitude in cooling rate. Heo *et al.* [21] reported a more than 0.3 uniaxial compressive plastic strain for a Zr-based MG nanopillar after proton irradiation, as compared to catastrophic failure without noticeable plasticity before irradiation. They speculated that the atomistic origin of this improved plasticity results from the change in icosahedral network by irradiation.

Recently, Ketov *et al*. [8] performed thermal cycling treatment between liquid nitrogen temperature and RT on different MGs, and obtained improved compressive plasticity. The authors attributed this rejuvenation to internal stress, which results from nonuniform thermal expansion coefficients due to heterogeneous glass structure. However, an atomic-scale characterization of the rejuvenation has not been obtained. Chapter 5 discusses both the RT structural relaxation and cryogenic rejuvenation effects through STZ characterization.

2.3 β Relaxation in Metallic Glasses

DMA [22] is a widely employed and highly sensitive technique to study the β relaxation for MGs, during which a sinusoidal stress is applied as,

$$\sigma = \sigma_0 \sin(\omega t), \tag{2.9}$$

where σ_0 is the amplitude, ω is the angular frequency, t is the time. The resulting strain is

$$\varepsilon = \varepsilon_0 \sin(\omega t - \delta). \tag{2.10}$$

δ is the phase lag between the stress and resulting strain. Then, the ratio of the stress to the strain results in a complex modulus [22],

$$E^* = \sigma/\varepsilon = E' + iE'',$$

where E' represents the storage modulus, and E'' represents the loss modulus, and are expressed as,

$$E' = (\sigma_0/\varepsilon_0) \cdot \cos(\delta), \quad (2.11)$$

and,

$$E'' = (\sigma_0/\varepsilon_0) \cdot \sin(\delta), \quad (2.12)$$

respectively.

In DMA, the loss modulus is measured at either a fixed temperature with varying frequency or vice versa. For many MGs, the β relaxation exhibits a broad hump/excess wing in the loss modulus at high frequency/low temperature, close to the broad α relaxation. A recently developed $La_{68.5}Ni_{16}Al_{14}Co_{1.5}$ MG exhibits a strong and separate β relaxation peak, as shown in Fig. 2.7 [23]. This La-based MG shows pronounced tensile plasticity at RT with a strain rate of $1.6 \cdot 10^{-6}$ s^{-1}, and at increasing temperature with increasing strain rates. The result suggests that the β relaxation may correlate with macroscopic plasticity. In addition, from the DMA testing frequency vs. corresponding peak temperature of the β relaxation data, Yu *et al.* [24] obtained that the activation energy of the β relaxation for $La_{55}Al_{15}Ni_{10}Cu_{10}Co_{10}$ MG approximately equals 89±6 kJ/mol. This value is close to the estimated value of potential-energy barrier for an STZ based on the cooperative shear model [25]. Therefore, the authors proposed that STZs and the beta relaxations are directly related due to a common structural origin. However, the results of Ju *et al.* [11,26] and the present work show that both the α and β relaxations are consistent with the STZ model.

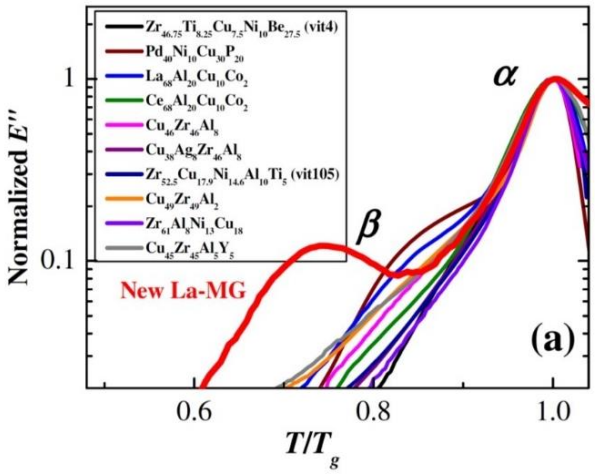

Figure 2.7. Comparison of normalized loss modulus vs. temperature between different MGs. The newly developed La-MG exhibits a pronounced β relaxation [23]. Reprinted with permission from Yu *et al.*, Tensile plasticity in metallic glasses with pronounced β relaxations, Phys. Rev. Lett. 108, 015504 (2012), Copyright 2012 by the American Physical Society.

A long-standing question has been why some MGs show a strong β relaxation peak while others do not. The answer is still inconclusive, but one known factor is the chemical composition, as discussed below. Figure 2.8 shows normalized loss modulus as a function of normalized temperature for La-based and Pd-based MGs [27]. In the La-based MGs, by substituting Ni with Cu atoms, which have similar atomic size, the β relaxation transitions from a pronounced peak to an excess wing. Therefore, it seems that the Ni atoms promotes the β relaxation, while Cu atoms reduce it. However, for the Pd-based MGs shown in Fig. 2.8b, the opposite trend happens – substituting Ni with Cu atoms promotes the β relaxation. Figure 2.8(a)&(b) suggest that 1) the chemical composition has a strong effect on the β relaxation behavior, and 2) the effect of the same element on the β relaxation behavior varies for different alloy compositions. By estimating the enthalpy of mixing for these two alloy systems, Yu *et al.* [27] speculated that large similar negative enthalpy of mixing among all constituting atoms results in a pronounced β relaxation, while

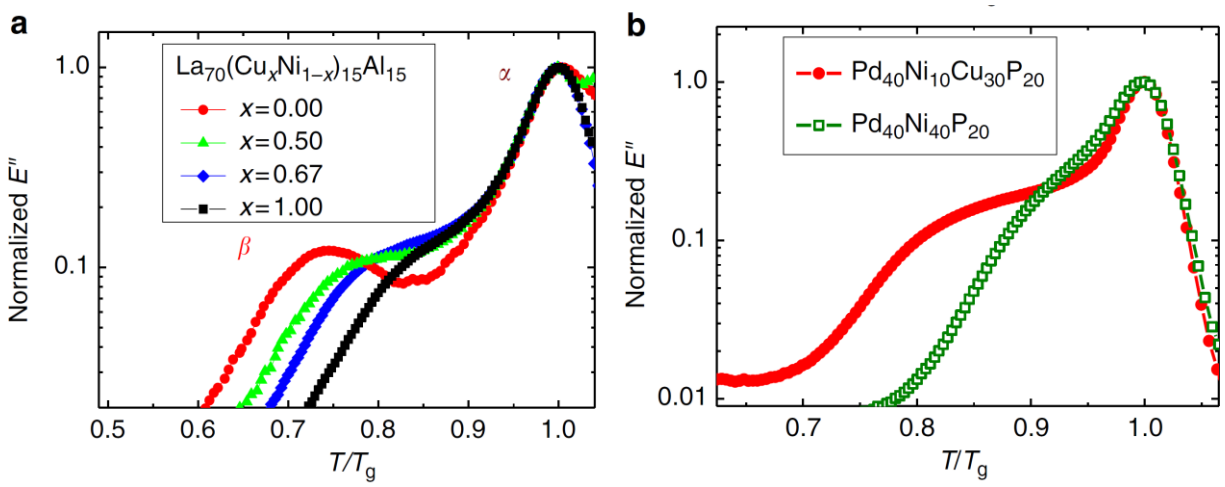

Figure 2.8. Normalized loss modulus as a function of temperature scaled by T_g [27]. (a) $La_{70}(Cu_xNi_{1-x})_{15}Al_{15}$, x=0, 0.5, 0.67, and 1, (b) $Pd_{40}(Cu_xNi_{1-x})_{30}Ni_{10}P_{20}$, x=0 or 1. Reprinted with permission from Yu *et al.*, Chemical influence on β-relaxations and the formation of molecule-like metallic glasses, Nat. Commun. 4, 2204 (2013), Copyright 2013 by Springer Nature.

positive or significantly varying pairwise values of mixing enthalpy suppress the β relaxation, and usually associate with excess wings. This correlation is consistent with both examples and offers a semi-quantitative way to predict the β relaxation. However, the underlying mechanism of the chemical composition effect on β relaxation is still not clear. Chapter 4 offers a microscopic picture for the α vs. β relaxation in terms of STZ properties, and Chapter 6 further discusses the composition effect on both the α and β relaxations.

2.4 References

[2.1] Z. F. Zhang, J. Eckert, and L. Schultz, *Acta Mater.* **51**, 1167 (2003).

[2.2] H. Bei, S. Xie, and E. P. George, *Phys. Rev. Lett.* **96**, 105503 (2006).

[2.3] A. L. Greer, Y. Q. Cheng, and E. Ma, *Mater. Sci. Eng. R* **74**, 71 (2013).

[2.4] A. S. Argon, *Acta Metall.* **27**, 47 (1979).

[2.5] M. L. Falk and J. S. Langer, *Phys. Rev. E* **57**, 7192 (1998).

[2.6] J. D. Ju, D. Jang, A. Nwankpa, and M. Atzmon, *J. Appl. Phys.* **109**, 053522 (2011).

[2.7] C. H. Rycroft and E. Bouchbinder, *Phys. Rev. Lett.* **109**, 194301 (2012).

[2.8] S. V. Ketov, Y. H. Sun. S. Nachum, Z. Lu, A. Checchi, A. R. Beraldin, H. Y. Bai, W. H. Wang, D. V. Louzguine-Luzgin, M. A. Carpenter, and A. L. Greer, *Nature* **524**, 200 (2015).

[2.9] H. B. Yu, W. H. Wang, and K. Samwer, *Mater. Today* **16**, 183 (2013).

[2.10] A. S. Argon and L. T. Shi, *Acta Metall.* **31**, 499 (1983).

[2.11] J. D. Ju and M. Atzmon, *MRS Commun.* **4**, 63 (2014).

[2.12] P. Schall, D. A. Weitz, and F. Spaepen, *Science* **318**, 1895 (2007).

[2.13] H. Kato, H. Igarashi, and A. Inoue, *Mater. Lett.* **62**, 1592 (2008).

[2.14] F. Shimizu, S. Ogata, and J. Li, *Acta Mater.* **54**, 4293 (2006).

[2.15] J. Megusar, A. S. Argon, and N. J. Grant, *Mater. Sci. Eng.* **38**, 63 (1979).

[2.16] M. Atzmon and J. D. Ju, *Phys. Rev. E* **90**, 042313 (2014).

[2.17] P. Murali and U. Ramamurty, *Acta Mater.* **53**, 1467 (2005).

[2.18] J. Pan, Y. X. Wang, Q. Guo, D. Zhang, A. L. Greer, and Y. Li, *Nat. Commun.* **9**, 560 (2018).

[2.19] D. J. Magagnosc, G. Kumar, J. Schroers, P. Felfer, J. M. Cairney, and D. S. Gianola, *Acta Mater.* **74**, 165 (2014).

[2.20] A. Q. Tool and C. G. Eichlin, *J. Am. Ceram. Soc.* **14**, 276 (1931).

[2.21] J. Heo, S. Kim, S. Ryu, and D. Jang, *Sci. Rep.* **6**, 23244 (2016).

[2.22] J. C. Qiao and J. M. Pelletier, *J. Mater. Sci. Technol.* **30(6)**, 523 (2014).

[2.23] H. B. Yu, X. Shen, Z. Wang, L. Gu, W. H. Wang, and H. Y. Bai, *Phys. Rev. Lett.* **108**, 015504 (2012).

[2.24] H. B. Yu, W. H. Wang, and H. Y. Bai, *Phys. Rev. B* **81**, 220201(R) (2010).

[2.25] W. L. Johnson and K. Samwer, *Phys. Rev. Lett.* **95**, 195501 (2005).

[2.26] J. D. Ju and M. Atzmon, *Acta Mater.* **74**, 183 (2014).

[2.27] H. B. Yu, K. Samwer, W. H. Wang, and H. Y. Bai, *Nat. Commun.* **4**, 2204 (2013).

CHAPTER 3
Experimental and Analysis Details

3.1 Materials

The metallic glasses (MGs) investigated in the present study are $La_{55}Ni_{20}Al_{25}$, $La_{70}Ni_{15}Al_{15}$, $La_{70}Cu_{15}Al_{15}$, and $Al_{86.8}Ni_{3.7}Y_{9.5}$ (at.%), the glass transition temperatures of which are 475 K [1], 431 K [2], 391 K [2], and ~ 520 K [3], respectively. The La-based MGs used for anelastic relaxation measurements were prepared by Dr. Ming Liu and Prof. Wei-Hua Wang of Chinese Academy of Sciences (CAS). The purity of each element, measured by inductively coupled plasma atomic absorption spectroscopy using IRIS Intrepid II mass spectrometer at Chinese Academy of Sciences, is higher than ~ 99 wt.%, and the composition of each alloy was verified by energy-dispersive X-ray spectroscopy using Thermo Fisher Nova 200 Nanolab SEM/FIB at MC2 center at the University of Michigan. The Al-based MG was prepared by Dr. F. Pinkerton of General Motors R&D Center. Because the La-based MGs are easy to oxidize, they were stored in argon-gas environment. All samples were in the form of thin ribbons about 20-40 μm thick and 1 mm wide, obtained through single-wheel melt-spinning using a Cr-coated Cu wheel, at a tangential velocity of 3 m/s (for the La-based MGs) or 40 m/s (for the Al-based MG) in vacuum. X-ray diffraction was employed to confirm the amorphous structure. Since the as-received La-based alloys aged at RT for a short time (~ $6 \cdot 10^5$ s) and underwent noticeable structural relaxation afterwards, samples with different RT ageing times were examined – a) for $La_{55}Ni_{20}Al_{25}$, the RT ageing times range from $2.6 \cdot 10^6$ s to $6.3 \cdot 10^7$ s, b) for $La_{70}(Cu_xNi_{1-x})_{15}Al_{15}$, x = 0 or 1, samples

were aged at RT from $1.9 \cdot 10^6$ s to $2.9 \cdot 10^7$ s. The RT ageing time for the examined Al-based MG is over two years.

3.2 Quasi-Static Anelastic Relaxation

3.2.1 Linear Regime at Room Temperature

To study the RT quasi-static anelastic relaxation over a wide time range, two techniques – nanoindenter cantilever bending for short-time measurements and bend relaxation ("mandrel") for long-time measurements were employed, as reviewed below.

Nanoindenter cantilever bending was performed by using a Hysitron TI 950 TriboIndenter in Prof. Kenneth Kozloff's lab of the Department of Orthopaedic Surgery at the University of Michigan. Figure 3.1(a) is a schematic illustration of the nanoindenter cantilever bending for measurements from ~ 0 s to 200 s. One sample was glued between two glass slides using epoxy, and different mounting compounds were tested to rule out their effect on the measurements in a previous study [4]. A fixed load, P, is applied, which results in a vertical displacement, $h(t)$, at the indent spot. The horizontal distance between the indent spot and clamp is L. The maximum bending strain, attained at the clamp on the surface [4], is

$$\varepsilon_{an}(t) = 3d \cdot h(t)/2L^2, \tag{3.1}$$

where d is the sample thickness. The equilibrium elastic strain at the sample surface, ε_{el}^0, is determined from the instant deflection upon loading [4]. Figure 3.1(b) shows the loading function of one measurement cycle. A fixed load, P=200 μN, was applied for 200 s, during which the

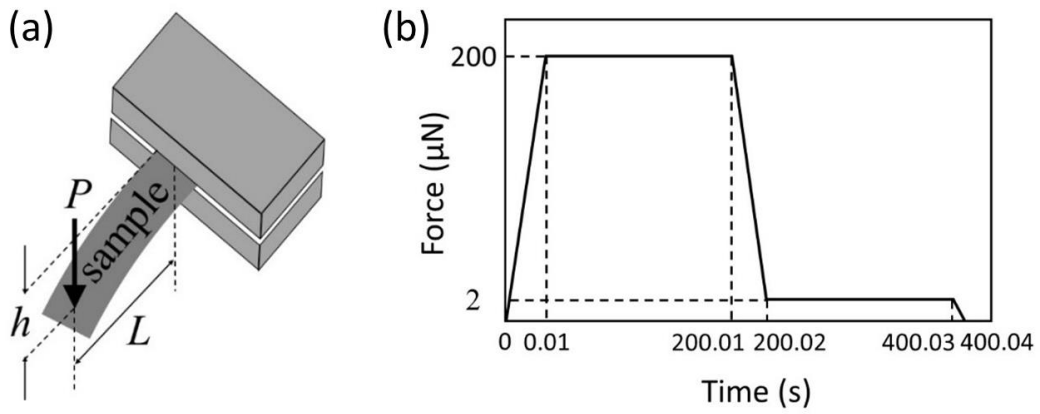

Figure 3.1. (a) Schematic illustration of nanoindenter cantilever bending measurements. A fixed load *P* is applied, and the time-dependent vertical displacement, *h*(*t*), is monitored. The horizontal distance between the indent spot and clamp is *L*. Redrawn from Ref. [4]. (b) Loading function for one measurement cycle – a high load of 200 μN for 200 s to obtain the strain vs. time data, and a low load of 2 μN for another 200 s to check reversibility.

anelastic strain vs. time data were collected at a rate of 300 pts/s. A subsequent small load of 2 μN for 200 s was used to check the displacement reversibility. For each alloy composition, at least three samples with the same thermal history were examined with 20 cycles for each sample.

Figure 3.2 is a schematic illustration of the mandrel technique in linear regime for longer measurement time over one year. Firstly, one sample with an initial radius of curvature, r_0, was selected (see details of curvature determination below). Then, it was constrained around a mandrel with radius *R* ranging from 0.345 cm to 0.802 cm for $2.0 \cdot 10^6$ s. Subsequently, the sample was relaxed constraint-free at RT for up to $3.2 \cdot 10^7$ s, with a time-dependent radius of curvature, *r*(*t*), where *t* is the time after constraint removal. The evolution in *r*(*t*) was monitored using a digital camera. Care was taken to make sure that the optical axis is perpendicular to the sample plane, and a stage micrometer was used for calibration. Diffuse backlight was employed for optimal image

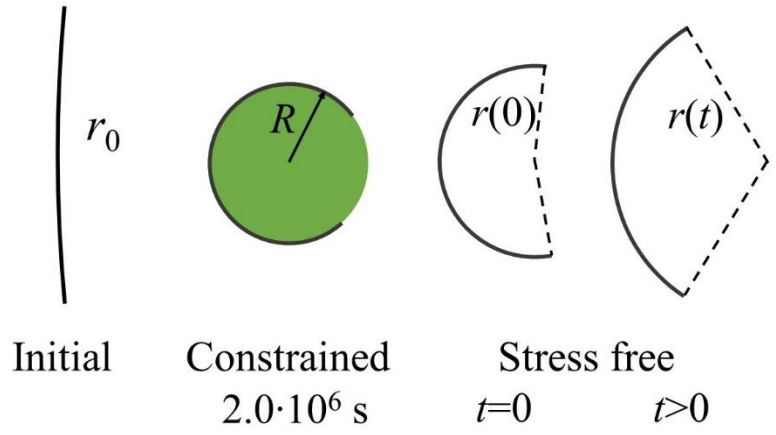

Figure 3.2. Schematic illustration of the bend-relaxation ("mandrel") measurements. A sample with an initial radius of curvature, r_0, is constrained around a mandrel with a radius R for $2.0 \cdot 10^6$ s, then relaxed constraint-free. The evolution in radius of curvature of the sample, $r(t)$, is monitored. Redrawn from Ref. [4].

quality. At each t value, four or five photographs were taken, and the final $r(t)$ value was determined as the average of all the images. To obtain $r(t)$ for each image, an automated image analysis method was developed in the present study with the help of an undergraduate student Luis Rangel DaCosta. The MATLAB® code commands of image digitization are explained in Appendix B. One example of the image analysis method is shown in Fig. 3.3. Figure 3.3(a) is a photograph of one sample at time t after constraint removal, along with a stage micrometer for length calibration. The photograph was digitized using MATLAB®, so that the coordinates of the data points corresponding to the sample were obtained. Then, a nonlinear curve fit with an equation,

$$y = (C^2 + (x - A)^2)^{0.5} + B, \tag{3.2}$$

where C the radius, and A and B the coordinates of the center, was performed on these data points, as shown in Fig. 3.3(b). An Orthogonal Distance Regression Iteration Algorithm [5] in OriginPro program was employed. This automated image analysis method significantly reduces the error bars in the strain vs. time curves relative to the on-screen visual fitting in the previous study [4].

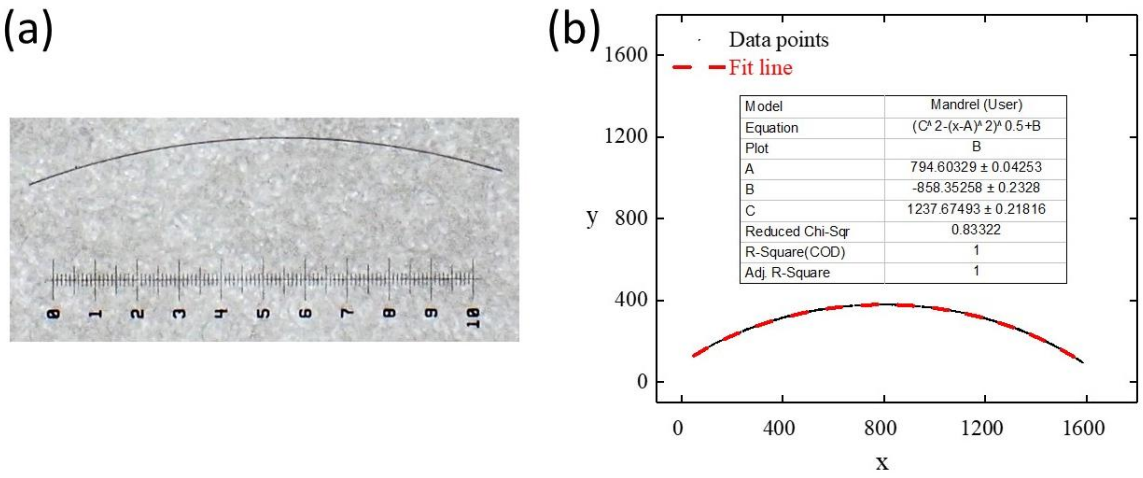

Figure 3.3. (a) Photograph showing one sample during constraint-free relaxation along with a stage micrometer for length calibration. (b) Nonlinear curve fit for the data points corresponding to the sample, obtained through image digitization.

In the mandrel measurements, the total constraining strain at sample surface is [4],

$$\varepsilon_{constr} = d/2 \cdot [1/R - 1/r_0], \tag{3.3}$$

where d is the sample thickness. It consists of two components – equilibrium elastic strain and anelastic strain, which at the end of the constraining period are [4],

$$\varepsilon_{el}^{0} = d/2 \cdot [1/R - 1/r(0)], \tag{3.4}$$

and,

$$\varepsilon_{an}(t) = d/2 \cdot [1/r(t) - 1/r_0], \tag{3.5}$$

respectively.

3.2.2 Linear Regime with Thermomechanical Treatment

To microscopically characterize the effect of structural relaxation and cryogenic rejuvenation, a thermomechanical treatment (Fig. 3.4) was applied to $La_{70}(Cu_xNi_{1-x})_{15}Al_{15}$, x=0 or 1, as detailed below. Firstly, samples were aged at RT for different durations from $1.9\cdot10^6$ s to $2.9\cdot10^7$ s, and three to eight sample were used for each condition. Subsequently, for samples with a RT ageing time of $1.0\cdot10^7$ s, they were cycled between liquid nitrogen temperature and RT for ten times, with 1 min and 3-min holding time, respectively. Then, bend-relaxation measurements were performed by constraining samples around mandrels with radii R for a standard time of $2.0\cdot10^6$ s. At last, the evolution in radius of curvature at time t after constraint removal, $r(t)$, was monitored using a digital camera.

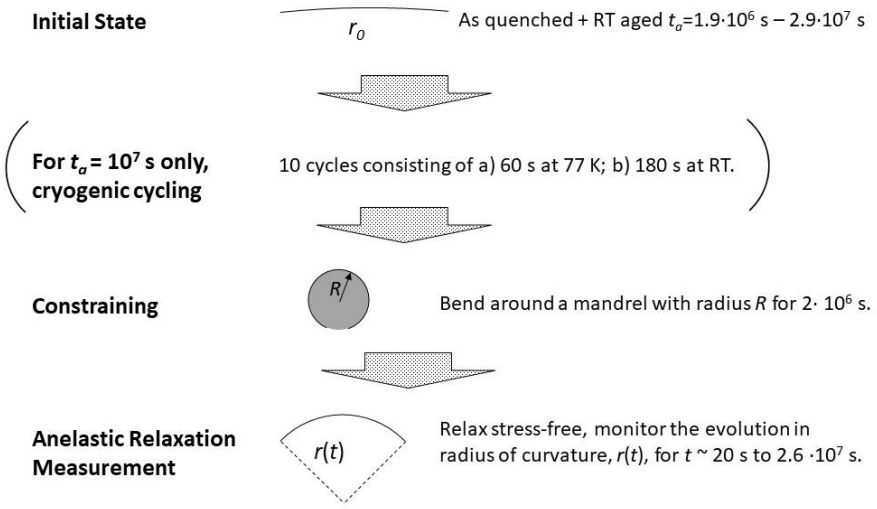

Figure 3.4. Schematic illustration of the thermomechanical treatment and measurement sequence [6]. Reprinted from Lei *et al.*, Microscopic characterization of structural relaxation and cryogenic rejuvenation in metallic glasses, Acta Mater. 164, 165 (2019), Copyright 2018, with permission from Elsevier.

3.2.3 Nonlinear Regime at Room Temperature

In order to conduct mandrel measurements in the nonlinear regime, higher applied stresses are needed. To achieve the goal, a new constraining method by using mandrels with smaller radius of curvature, 0.09 cm or 0.11 cm, was developed and is shown in Fig. 3.5. A vise was used to apply load on the constraining components, which include a machined device, a mandrel, a neoprene block, and a sample. The sample was placed between the mandrel and neoprene block. The machined device was used to press the mandrel until two free ends of the sample just touching each other, so that a well-characterized geometry was obtained, as discussed below. A peephole on the side surface of the machined device was to observe the two touching ends during constraining. Figure 3.5 includes one photograph showing the two touching ends of a sample under

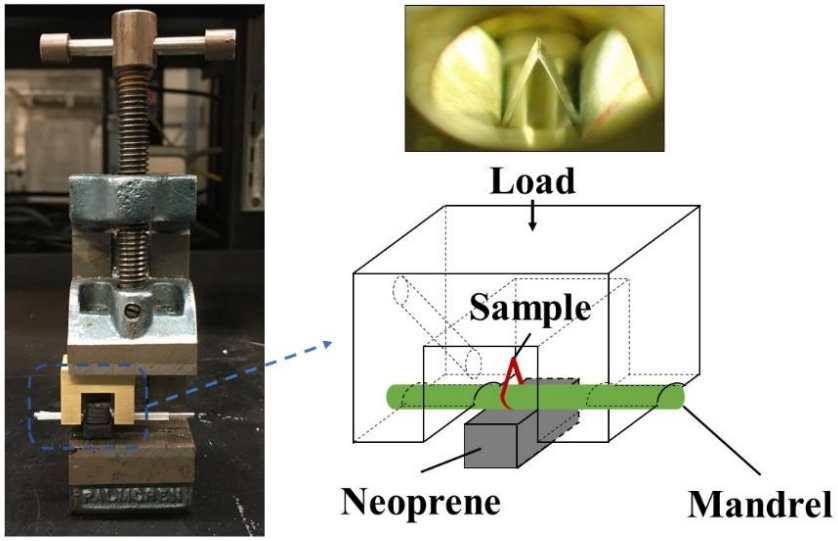

Figure 3.5. Constraining setup for the nonlinear-regime mandrel measurement. A vise is used to apply load on the constraining component – a sample placed between a mandrel and neoprene block, and a machined device to press the mandrel until two constraint-free ends of the sample just touching each other. A peephole on the side surface is used to observe the two touching ends during constraining, and a photograph showing the two touching ends of one sample under constraint is in the upper-right corner.

constraint. Because of the low modulus of the neoprene, the pressure on the sample was negligible compared to the bending stress. A lubricant was applied between the sample and neoprene to confirm that friction played a negligible role. It should be noted that, contrary to the linear-regime constraining method in Section 3.2.1, where the whole sample was under constraint, in the nonlinear case, only a small section of the sample was under constraint, with the two ends being constraint-free.

The expression of the total constraining strain at the sample surface for the nonlinear regime is same as Eq. (3.3). Because the strain rate is not linear in the stress, there is residual stress in the sample, and the strain distribution is no longer linear. Therefore, Eqs. (3.4)&(3.5) now represent the apparent elastic strain and apparent anelastic strain on the surface, respectively, and not their actual values as in the linear regime. The details of the apparent vs. actual strain in the nonlinear regime is discussed in Chapter 7. Since only a small section of the sample was under constraint, it is challenging to directly measure the time-dependent radius of curvature of the constrained section, $r(t)$, during constraint-free relaxation. However, as mentioned before, the constraining method leads to a well characterized geometry, which allows for a reliable determination of $r(t)$. Figure 3.6(a)&(b) show the sample geometry under constraint and after constraint removal, respectively. The red curve corresponds to the constrained section, while the blue lines represent the constraint-free ends. The yellow dashed lines are fit lines to the free ends. The time-dependent radius of curvature of the previously constrained section at time t after constraint removal is,

$$r(t) = [(\pi + \varphi) \times (R + d/2)] \times$$

$$\times \left[4 \arcsin\left(\frac{L'}{2r_0}\right) + 2 \arccos\left(\frac{L'}{2r_0}\right) + \frac{(\pi+\varphi)\times(R+d/2)}{r_0} - \frac{L_{total}}{r_0} - \alpha(t)\right]^{-1}, \quad (3.6)$$

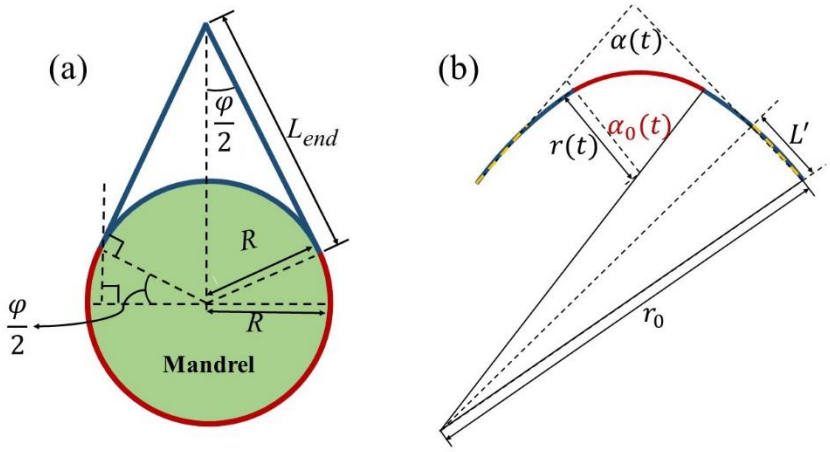

Figure 3.6. Sample geometry (a) under constraint (the small curvature of the free ends is neglected), (b) during unconstrained relaxation (not to scale). $\alpha(t)$ is used to determine the evolution of the curvature of the previously bent section during unconstrained relaxation. The length of constrained section (red) equals $(\pi+\varphi)\times(R+d/2)$, where R is the mandrel radius and d is the sample thickness. Dashed lines are fits to the unconstrained ends.

where φ is the angle between two constraint-free ends under constraint, L' is the length of the fit line, and $\alpha(t)$ is the time-dependent angle between the two fit lines during constraint-free relaxation. A detailed derivation of Eq. (3.6) is given in Appendix A.

3.3 Tensile Tests and Dynamic Mechanical Relaxation

To examine the effect of RT ageing and cryogenic cycling on mechanical properties, e.g., Young's modulus, RT tensile tests at a strain rate of 10^{-3} s^{-1} were performed on $La_{70}Cu_{15}Al_{15}$ and $La_{70}Ni_{15}Al_{15}$ aged at RT for 1) different durations, and 2) the same amount of time with and without ten subsequent cryogenic cycles. The tensile tests were performed using a TA Instruments RSA III Dynamic Mechanical Analyzer at the University of Michigan. At least four adjacent pieces from the same ribbon were used for each alloy composition and thermal history so that variations among samples were minimized.

To compare the plasticity of La-based MGs with Cu vs. Ni, RT tensile tests at strain rates of 10^{-4} s^{-1}, 10^{-5} s^{-1}, and $1.6 \cdot 10^{-6}$ s^{-1} were performed on $La_{70}(Ni_xCu_{1-x})_{15}Al_{15}$ and $La_{68.5}(Ni_xCu_{1-x})_{16}Co_{1.5}Al_{14}$, x=0 or 1. In addition, dynamic mechanical relaxation measurements with temperature-sweeping mode were performed on $La_{70}Cu_{15}Al_{15}$ and $La_{68.5}Cu_{16}Co_{1.5}Al_{14}$ to examine their β relaxation behavior. The samples were prepared by Jie Shen and Prof. Yonghao Sun from Chinese Academy of Sciences, who also performed the tensile tests at different strain rates and the dynamic mechanical relaxation measurements.

3.4 Relaxation-Time Spectrum Computation

Relaxation-time spectra were computed from the anelastic strain vs. time using a software package, CONTIN [7,8], which yields stable and consistent fitting of $\varepsilon_{an}(t)/\varepsilon_{el}^0$. Based on the standard linear solid model (Section 2.1.1), two fitting equations were obtained [4],

$$\varepsilon_{an}(t)/\varepsilon_{el}^0 = c_\infty + A \cdot t + \sum_{i=1}^{N_1} \varepsilon_i \cdot [1 - \exp(-t/\tau_i)], \quad (3.7)$$

and,

$$\varepsilon_{an}(t)/\varepsilon_{el}^0 = c_\infty + \sum_{i=1}^{N_2} \varepsilon_i \exp(-t/\tau_i), \quad (3.8)$$

for cantilever bending and mandrel measurements, respectively. N_1 and N_2 are less than the number of data points. For cantilever bending data, N_1 = 100 for all alloy compositions, while for mandrel measurements, N_2 = 50 for $La_{70}(Cu_xNi_{1-x})_{15}Al_{15}$, x = 0 or 1, and N_2 = 65 for $La_{55}Ni_{20}Al_{25}$. c_∞, A, and ε_i are fitting parameters. τ_i are fixed, logarithmically spaced relaxation time values. The linear term in Eq. (3.7) and the constant term in Eq. (3.8) account for the anelastic processes with time constants longer than the measurement duration.

The continuous spectra were approximated as:

$$f(\tau_i) = \varepsilon_i / \Delta \ln \tau, \tag{3.9}$$

and,

$$\Delta \ln \tau = \ln[\tau_{max}/\tau_{min}] \,/(N-1), \tag{3.10}$$

where τ_{min} and τ_{max} are minimum and maximum relaxation time values, respectively, and equal 10 s vs. $6.4 \cdot 10^7$ s and 10 s vs. $5.2 \cdot 10^7$ s for $La_{70}(Cu_xNi_{1-x})_{15}Al_{15}$, x = 0 or 1 and $La_{55}Ni_{20}Al_{25}$, respectively. A regularization term [7,8], which penalizes a solution due to deviations from behavior expected on the basis of statistical *a prior* knowledge or the principle of parsimony, was added in the nonlinear least-squares fit. The advantage of the regularization term is to eliminate sharp, unphysical, variations due to numerical artifacts [7,8]. Similar regularization parameters were used for all tests/samples for consistency. Within a range of regularization parameter values, the spectrum does not change significantly. Ref. [4] includes more detailed fitting and consistency checks, i.e., a) Different values of N_1 and N_2 in Eqs. (3.7)&(3.8) yielded consistent spectrum. b) Different ranges of τ_i led to consistent results if the range of τ_i values is larger than that of the measurement time. Peak properties were determined from an average over all samples with the same condition. The error bars are the standard deviations of the mean. Code commands to perform spectrum computation using CONTIN are detailed in Appendix C.

3.5 References

[3.1] S. V. Ketov, Y. H. Sun, S. Nachum, Z. Lu, A. Checchi, A. R. Beraldin, H. Y. Bai, W. H. Wang, D. V. Louzguine-Luzgin, M. A. Carpenter, and A. L. Greer, *Nature* **524**, 200 (2015).

[3.2] X. D. Wang, B. Ruta, L. H. Xiong, D. W. Zhang, Y. Chushkin, H. W. Sheng, H. B. Lou, Q. P. Cao, and J. Z. Jiang, *Acta Mater.* **99**, 290 (2015).

[3.3] A. Inoue, K. Ohtera, A. -P. Tsai, H. Kimura, and T. Masumoto, *Jpn. J. Appl. Phys.* **27**, L1579 (1988).

[3.4] J. D. Ju, D. Jang, A. Nwankpa, and M. Atzmon, *J. Appl. Phys.* **109**, 053522 (2011).

[3.5] W. Gander, G. H. Golub, and R. Strebel, *BIT Numer. Math.* **34(4)** 558 (1994).

[3.6] T. J. Lei, L. Rangel DaCosta, M. Liu, W. H. Wang, Y. H. Sun, A. L. Greer, and M. Atzmon, *Acta Mater.* **164**, 165 (2019)

[3.7] S. W. Provencher, *Comput. Phys. Commun.* **27**, 213 (1982).

[3.8] S. W. Provencher, *Comput. Phys. Commun.* **27**, 229 (1982).

CHAPTER 4

Shear Transformation Zone Analysis of Anelastic Relaxation of $La_{55}Ni_{20}Al_{25}$ Metallic Glass Reveals Distinct Properties of α and β Relaxations

Reprinted with permission from T. J. Lei, L. Rangel DaCosta, M. Liu, W. H. Wang, Y. H. Sun, A. L. Greer, and M. Atzmon, "Shear transformation zone analysis of anelastic relaxation on a metallic glass reveals distinct properties of α and β relaxations," Phys. Rev. E 100, 033001 (2019). DOI: https://doi.org/ 10.1103/PhysRevE.100.033001.

4.1 Introduction

Metallic glasses (MGs) are known to exhibit high strength and elastic limit, making them attractive for structural applications. However, a main limitation on their applications is their very limited macroscopic plasticity due to catastrophic failure resulting from strain localization within dominant shear bands [1,2]. Much work has been conducted to improve MG plasticity, but the deformation mechanism has yet to be fully understood [1,3,4]. The deformation of MGs is believed to be accommodated by shear transformation of atomic clusters, termed shear transformation zones (STZs) [5,6]. At small strain, STZs are few and isolated, and can be reversed to their original configuration due to back stress in the elastic matrix, which gives rise to anelastic behavior. At high strain, the larger number of STZs leads to loss of back stress, resulting in plastic deformation.

Johari and Goldstein identified two relaxation processes in supercooled liquids and glasses: a main α relaxation and a secondary β relaxation at higher frequency/lower temperature [7]. In molecular glasses, these two modes can be attributed to intermolecular vs. intramolecular motion. However, they have also been observed in metallic glasses, where such a distinction is not possible [8]. Even when it is less distinguishable as a tail in the loss modulus vs. temperature/frequency, the β relaxation has been argued to originate from a different mechanism than that of the α relaxation [9], based on a discrepancy between experimental data and a stretched exponential relaxation – Kohlrausch-Williams-Watts (KWW) function [10]. However, the application of KWW to anelastic relaxation well below the glass transition temperature (T_g) is phenomenological, and often results in inconsistent fitting parameters [11]. For an Al-based MG, Ju and Atzmon showed that both the main peak (α) in the loss modulus and the tail (β) can be explained with a single, atomically quantized, STZ hierarchy: the former (latter) results from large and slow (small and fast) STZs [12]. A similar conclusion applies to our analysis of the dynamic-mechanical response of a Zr-based alloy [13]. While conventional wisdom holds that the α relaxation is irreversible and occurs only above T_g, Refs. 12,14,15 show that it is reversible at small strain and can be observed well below T_g if a sufficiently long timescale is employed. This is a reminder that T_g is defined kinetically. Recently, Yu *et al.* reported that MGs with a distinct and pronounced β relaxation exhibit relatively high tensile plasticity [16]. They also suggested that the STZ mechanism underlies the β relaxation [17].

In the present study, the microscopic origin of the α and β relaxations and the microscopic effect of structural relaxation (ageing) on them have been investigated in amorphous $La_{55}Ni_{20}Al_{25}$, which exhibits a distinct and pronounced β relaxation [18]. RT quasi-static anelastic relaxation

measurements were performed after RT ageing for varying amounts of time. The range of time constants has been extended by orders of magnitude compared to Ref. 15 to include the β relaxation. Similar to Refs. 14,15, the time-constant spectra consist of distinct peaks, corresponding to an *atomically quantized STZ hierarchy*. By employing a standard linear solid model and STZ-based constitutive law, size-resolved STZ properties are obtained. Two different regimes are identified, corresponding to α and β relaxations. While the STZ hierarchy exhibits a smooth transition between the regimes, the main new result is the striking difference between the properties of STZs associated with the α vs. β relaxation: The latter exhibits a smaller atomic-volume increment in the STZ hierarchy than the former, and is independent of prior ageing.

4.2 Background

Purely anelastic deformation is an ideal regime in which to study STZ properties, since STZs occupy a small volume fraction and do not interact with each other. Ju *et al.* [14,19] performed quasi-static anelastic relaxation measurements on an Al-based MG at RT, using a combination of nanoindenter cantilever bending and bend relaxation, over time ranging from 1.0 s to 200 s and from ~ 10^3 s to $1.1 \cdot 10^8$ s, respectively. The evolution of anelastic strain was used to compute the corresponding relaxation-time spectra, $f(\tau)$, as a function of relaxation time, τ. A series of distinct peaks were observed in the spectra. The data were analyzed using a standard linear solid model consisting of Voigt units, each corresponding to a peak, in series with each other and with a spring representing the elastic component. The peaks were shown to correspond to a quantized hierarchy of STZs, with their volume values spaced by the atomic volume of Al, the majority element. STZs with time constants within the measured range comprised 14 to 22 atoms. The spectra also yielded

the size-density distribution of *potential* STZs, i.e., atomic clusters capable of undergoing shear transformations, as reviewed below.

The relaxation time constant for each *m*-type STZ, τ_m, was taken as the median of the corresponding spectrum peak. Combining the expression for the macroscopic shear strain rate [5], and the activation free energy of shear transformation for *m*-type STZs [20],

$$\Delta F_m = \left[\left(\frac{(7-5\nu)}{30(1-\nu)} + \frac{2(1+\nu)}{9(1-\nu)}\bar{\beta}^2\right)\gamma_0^T + \frac{1}{2}\frac{\overline{\sigma_{STZ}}}{\mu}\right]\mu\gamma_0^T\Omega_m, \tag{4.1}$$

τ_m can be expressed as [12],

$$\tau_m = \frac{3\eta_m'}{E_m'} = \frac{1}{\Omega_m\gamma_0^T}\cdot\frac{3kT}{2\mu(1+\nu)\gamma_0^c\nu_G}\cdot\exp\left(\mu\Omega_m\left\{\frac{\gamma_0^T}{kT}\left[\left(\frac{(7-5\nu)}{30(1-\nu)} + \frac{2(1+\nu)}{9(1-\nu)}\bar{\beta}^2\right)\gamma_0^T + \frac{1}{2}\frac{\overline{\sigma_{STZ}}}{\mu}\right]\right\}\right). \tag{4.2}$$

η_m' and E_m' are the effective viscosity and effective Young's modulus, respectively, of the *m*-type STZs. Ω_m is the *m*-type STZ volume. $\gamma_0^c = [2(4-5\nu)/15(1-\nu)]\gamma_0^T$ is the constrained transformation shear strain, with γ_0^T being the unconstrained value. $\Omega_m\gamma_0^T$ is the activation volume. Following Ref. 14, a γ_0^T = 0.2 is assumed. ν_G is the attempt frequency, *k* is the Boltzmann constant, and *T* is the temperature. ν is Poisson's ratio, $\bar{\beta}^2 \sim 1$ is the dilatancy factor. $\overline{\sigma_{STZ}}$ is the shear resistance of STZs, μ is the shear modulus, and $\overline{\sigma_{STZ}}/\mu$ = 0.025 [21].

The size-density distribution, i.e. the volume fraction occupied by *m*-type *potential* STZs [14], c_m, is equal to the area of the corresponding spectrum peak *m*,

$$c_m = \int_m f(\tau)\mathrm{d}\ln\tau = \varepsilon_{an}^m/\varepsilon_{el}^0. \tag{4.3}$$

ε_{an}^{m} and ε_{el}^{0} are the nominally equilibrated anelastic strain due to *m*-type STZs and the corresponding equilibrium elastic strain, respectively (see experimental details below). Deviations from mechanical equilibrium for the largest and slowest active STZ type at the end of the constraining period are accounted for in the discussion below.

4.3 Experimental and Analysis Procedure

Amorphous $La_{55}Ni_{20}Al_{25}$ (at. %) ribbons ~ 22 μm thick and 1 mm wide were obtained by single-wheel melt-spinning, using a Cr-coated Cu wheel at a tangential velocity of 3 m/s in vacuum. The glass transition temperature of the alloy is 475 K [3]. X-ray diffraction was employed to confirm the amorphous structure. To study the RT structural relaxation effect, samples were first aged at RT for durations of $2.6 \cdot 10^6$ s to $2.9 \cdot 10^7$ s. Following the ageing treatment, two techniques, nanoindenter cantilever bending for short measurement time and bend relaxation ("mandrel") for longer time [14], as shown in Fig. 4.1 and described below, were performed to monitor RT quasi-static anelastic relaxation. All results shown originate from a single batch. Samples were kept under inert atmosphere during ageing and relaxation.

For nanoindenter cantilever bending, each measurement cycle consisted of a fixed load of 200 μN for a duration of 200 s, during which the vertical displacement was monitored as a function of time, and a small load of 2 μN for 200 s to verify reversibility. Three samples were examined for each ageing time, with 20 measurement cycles for each sample. The elastic and anelastic strain, ε_{el}^{0} and $\varepsilon_{an}(t)$, were determined from the instant and time-dependent deflection following load application, respectively [14].

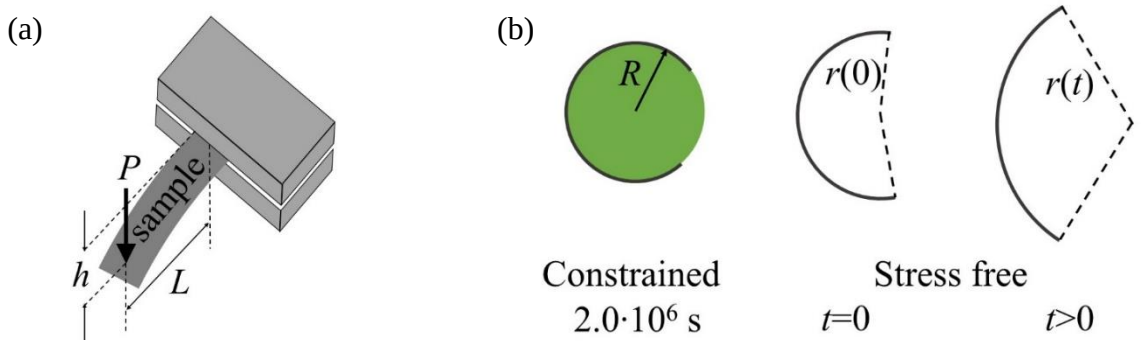

Figure 4.1. Schematic illustration of (a) nanoindenter cantilever bending and (b) bend relaxation ("mandrel"). For the former, a fixed load P is applied on the sample for 200 s. The vertical displacement, h, is monitored as a function of time. For the latter, the sample is constrained around a mandrel with a radius R for $2.0 \cdot 10^6$ s, then relaxed stress-free for up to $3.2 \cdot 10^7$ s, while monitoring the evolution of radius of curvature, $r(t)$.

For mandrel measurements, samples were constrained around mandrels of radii R ranging from 0.348 cm to 0.802 cm for $2.0 \cdot 10^6$ s, then relaxed stress-free for up to $3.2 \cdot 10^7$ s. 1-7 samples were used for each value of RT ageing time. The evolution of radius of curvature, $r(t)$, during stress-free relaxation, was monitored using a digital camera. The camera's optical axis was aligned perpendicular to the sample plane, and a stage micrometer was used for calibration. Diffuse backlight was employed for optimal image quality. An automated image analysis and curvature fitting method was developed, which significantly limits the error in the strain. The equilibrium elastic strain at the end of the constraining period, and the maximum bending strain at time t after constraint removal, both attained at the surface, were determined from the curvature evolution [14].

Relaxation-time spectra were computed from the anelastic strain data using CONTIN, a portable package for inverse problems that yields stable and consistent fitting of $\varepsilon_{an}(t)/\varepsilon_{el}^0$ [22,23]. Based on the standard linear solid model used, two fitting equations are obtained,

$$\varepsilon_{an}(t)/\varepsilon_{el}^{0} = c_{\infty} + A \cdot t + \sum_{i=1}^{N_1} \varepsilon_i [1 - \exp(-t/\tau_i)], \quad (4.4)$$

and,

$$\varepsilon_{an}(t)/\varepsilon_{el}^{0} = c_{\infty} + \sum_{i=1}^{N_2} \varepsilon_i \exp(-t/\tau_i), \quad (4.5)$$

corresponding to nanoindenter cantilever bending and mandrel measurements, respectively, where c_∞, A, and the ε_i are fitting parameters. Fixed, logarithmically spaced relaxation-time values, τ_i, were used, N_1 = 100 ranging from 0.0015 s to 400 s for the cantilever bending data, and N_2 = 65 ranging from 10 s to $6.4 \cdot 10^7$ s for the mandrel data. A regularization term is included in the CONTIN fitting – it eliminates sharp, unphysical, variations in the spectra that may arise due to numerical artifacts [7,8]. For consistency, similar regularization parameter values were used for all samples. Within a range of values, the computed spectrum does not change significantly. Further details, e.g., on consistency checks, are provided in Ref. 14. Peak properties were determined from an average over all samples for each ageing condition. The standard deviation of the mean was used as an estimate of the random error.

4.4 Results and Discussion

Figure 4.2 shows the normalized anelastic bending strain, $\varepsilon_{an}(t)/\varepsilon_{el}^{0}$, as a function of time. The data are obtained from both cantilever bending and mandrel measurements for $La_{55}Ni_{20}Al_{25}$ ribbons with different RT ageing times. For cantilever bending with time ranging from ~ 0.003 s to 200 s, each curve is an average of all samples with the same ageing time. Due to the large number of experimental data points (~ 60000) for each measurement cycle, the curves displayed consist of an average of every 500 data points. All data points were used in the analysis. For

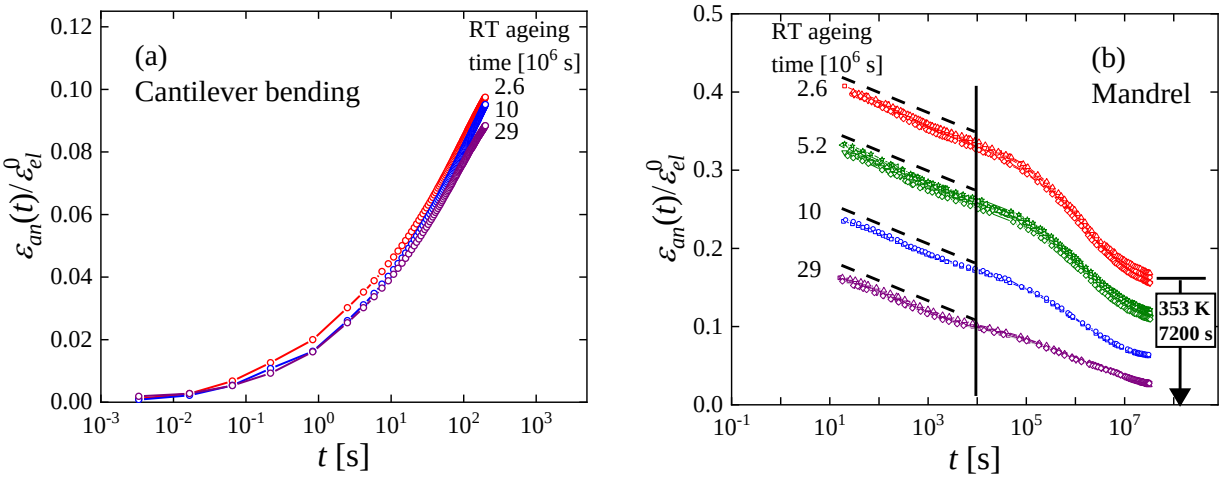

Figure 4.2. Anelastic bending strain at the surface normalized by equilibrium elastic strain vs. measurement time, of $La_{55}Ni_{20}Al_{25}$ ribbons with different RT ageing times: a) nanoindenter cantilever bending. Each curve corresponds to an average of all samples with the same ageing condition, and each point is an average of every 500 experimental data points, b) mandrel measurements. Data for all samples are shown, and dashed lines have the same slope.

mandrel measurements, from ~ 20 s to $3.2 \cdot 10^7$ s, data corresponding to all samples for each ageing condition are displayed, and show sample-to-sample reproducibility. The time ranges for the two measurement techniques overlap. The final strain for cantilever bending is much lower than the initial strain in mandrel measurement, since samples do not mechanically equilibrate in the former case. It is noted that samples from different batches, for which the strain data are not as extensive, exhibit different anelastic behavior, indicating variations among nominally identical samples, likely due to cooling-rate differences or minor composition differences.

For cantilever bending with short measurement time, RT ageing does not significantly affect the anelastic strain magnitude and evolution (Fig. 4.2a). However, a dramatic effect of prior RT ageing is observed at longer time (Fig. 4.2b). The overall strain magnitude decreases with increasing ageing time, and two regimes of strain evolution are observed. For measurement time up to ~ 10^4-

10^5 s, the absolute strain relaxation rate is the same for all ageing times (see dashed lines in Fig. 4.2b); for $t > 10^4$-10^5 s, the strain evolution varies with prior ageing time: "younger" samples have higher strain that decreases at a higher absolute rate. It is apparent that the difference in the strain magnitude among different ageing times is mainly due to processes with large time constants. The time at which the transition between the two regimes occurs, ~ 10^4-10^5 s, is much shorter than the shortest ageing time ($2.6 \cdot 10^6$ s). This indicates that the processes of structural relaxation and anelastic relaxation have different mechanisms. Two additional observations are made: a) The strain of the "oldest" sample approaches zero at long measurement time; b) While the "youngest" sample still exhibits high normalized anelastic strain after being relaxed stress-free for one year at RT, its strain drops to zero after annealing at 353 K for 3600 s. Both observations indicate that the strain measured is fully reversible, i.e., anelastic. Cryogenic cycling between liquid-nitrogen temperature and RT, applied after ageing, does not obviously affect the magnitude of the subsequently induced anelastic strain. The effect of RT ageing and cryogenic cycling on the time-constant spectra is discussed below.

In order to examine the evolution of both fast and slow processes more directly, strain values obtained from mandrel measurements at four measurement times, $t = 0$ s, 10^4 s, 10^6 s and $2 \cdot 10^7$ s, are shown in Fig. 4.3 as a function of prior RT ageing time (t_a). From $t = 0$ s to 10^4 s, the strain values decrease by a similar absolute amount (0.065 ± 0.001) for all t_a values, indicating that fast processes are not significantly affected by RT ageing, as also seen in Fig. 4.2. However, the decrease at long measurement time varies with t_a, e.g. the strain decreased by 0.07 from $t = 10^6$ s to $2 \cdot 10^7$ s for $t_a = 2.6 \cdot 10^6$ s, but only by 0.027 in the same measurement time range for $t_a = 2.9 \cdot 10^7$ s. As further discussed below, this indicates that the volume fraction occupied by large and slow

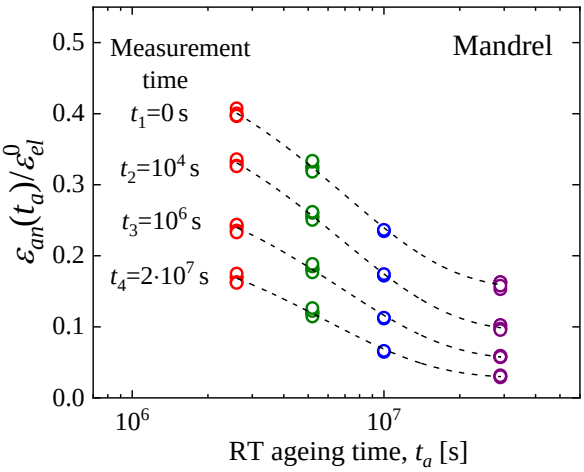

Figure 4.3. Normalized anelastic strain from mandrel measurements at four measurement times, t_i, as a function of prior RT ageing time, t_a.

potential STZs is affected by RT ageing. We note that practical constraints prevented us from accessing shorter ageing times to determine whether the small and fast STZs are affect by ageing in the early stages.

The relaxation-time spectra computed from Fig. 4.2 are shown in Fig. 4.4. An average spectrum of all samples for each ageing condition is shown for cantilever bending, while two representative spectra for each ageing condition are included for mandrel measurements. The two techniques allow a time-constant range from 0.0015 s to 6.4·10^7 s to be studied. All spectra consist of distinct peaks, which we associate with different STZ types, labeled with m = 1, …, 8. For each ageing condition, the set of peak areas exhibits two maxima as a function of m, as becomes clearer below (Fig. 4.8). These maxima correspond to α and β relaxation, at long and short time, respectively. Each α and β involves several STZ sizes. At room temperature, the maximum α peak likely corresponds to a τ value longer than the duration of the experiment. If the present spectra are used

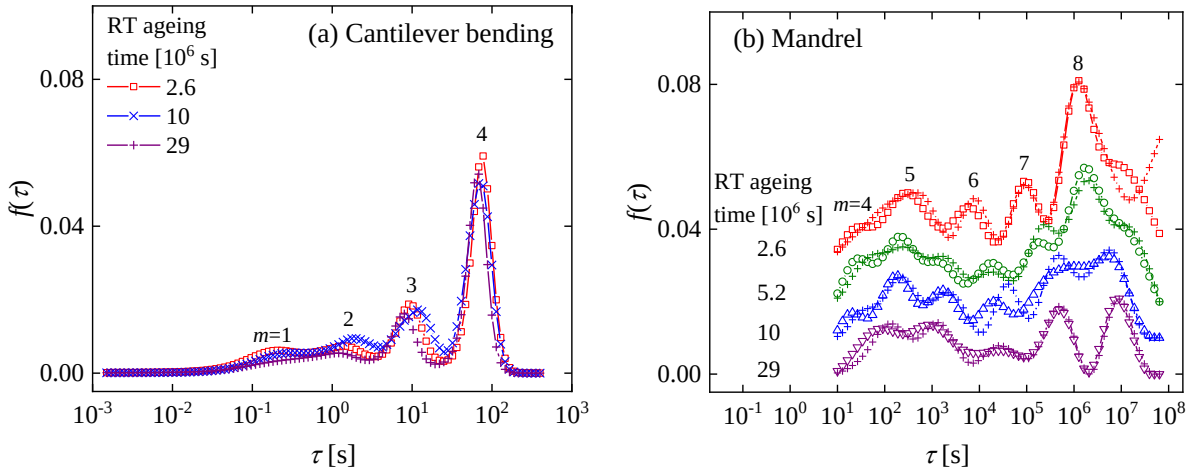

Figure 4.4. Relaxation-time spectra of $La_{55}Ni_{20}Al_{25}$ with different RT ageing times. Distinct peaks are observed and labeled m=1,…8. (a) Nanoindenter cantilever bending. Each curve corresponds to an average of all samples at the same ageing condition; (b) Mandrel measurements – two representative curves are shown for each RT ageing time. The spectra are shifted upwards for clarity. $m \leq 5$ peaks correspond to the β relaxation, and $m \geq 6$ to the α relaxation (see discussion).

to compute the loss modulus, as measured by dynamic mechanical analysis, the α and β peaks in the spectrum envelope correspond directly to those in dynamic-mechanical analysis (DMA): large/small τ corresponds to low/high frequency, respectively, as fixed temperature (or high/low temperature at fixed frequency). Because even a single time constant in the spectrum results in a Cauchy-shaped loss modulus as a function of frequency, the atomically-quantized hierarchy cannot be discerned in the loss-modulus. However, for data sufficiently small scatter, the spectrum can be obtained using a computational approach similar to that employed in the present work [13].

It is noticed that, for the same ageing condition, the intensity of the last peak from cantilever bending is different from that of the first peak from mandrel measurement, even though they are expected to correspond to the same process. A possible explanation is that the standard linear solid

model employed does not adequately describe the difference between fixed-load and stress-free relaxation. Differences in the peak medians obtained by the two measurement techniques are within sample-to-sample variability. With increasing ageing time, peak positions for small time constants do not vary significantly, while the position of the last peak obviously shifts to longer time. A similar observation was reported in Ref. 24 for a far narrower range of time constants. The peak intensities for small time constants are not visibly affected by RT ageing either. However, the $m = 8$ peak area, c_8, decreases dramatically with increasing ageing time. This is a manifestation of the observations in Figs. 4.2 & 4.3 that the difference in the strain magnitude among different ageing conditions is mainly due to processes with larger time constants. Ten cryogenic cycles between liquid-nitrogen temperature and RT, performed after ageing for $5.2 \cdot 10^6$ s and prior to anelastic relaxation measurements, did not change the peak positions and intensities. It slightly broadened the last two peaks.

To further study the microscopic effect of structural relaxation, STZ properties are now examined as a function of ageing time. Figure 4.5 shows the evolution with RT ageing time of relaxation time constants, τ_m, taken as the corresponding peak medians: Fig. 4.5(a) shows τ_m as a function of STZ type, m, for varying RT ageing times. One observes two different regimes for each ageing time: the slope for large time constants is larger than for smaller time constants. Furthermore, RT ageing does not affect the small time constants significantly as the slopes are very similar for small τ_m values. However, large time constants are influenced by ageing by up to a factor of 10, as seen by the increasing slope with increasing ageing time. This behavior corresponds to the shift in the peak position with increasing ageing time for large time constants in Fig. 4.4. Fig. 4.5(b) shows each τ_m as a function of ageing time, dashed lines are power-law fits. It is clear that the slope is

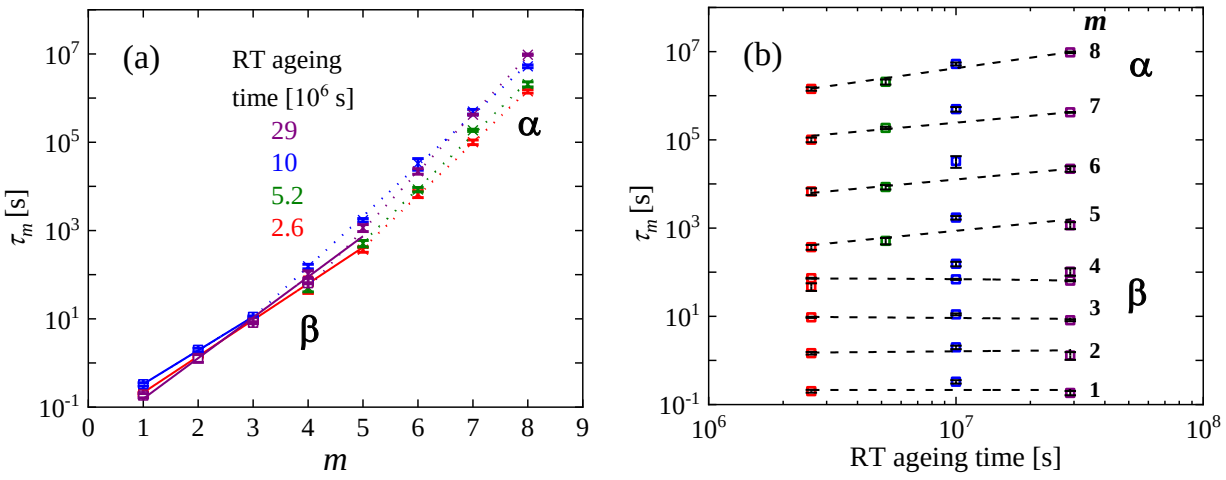

Figure 4.5. (a) Relaxation time constant (τ_m) of each STZ type (m) for different RT ageing times. (b) Relaxation time constants as a function of RT ageing time of different STZ types. Dashed lines are power-law fits.

very small for m = 1-4, and higher and similar for m = 5-8. As detailed below, we attribute the evolution of τ_m to an increasing shear modulus during structural relaxation.

In the following analysis, we first assume that the same constitutive law, and therefore Eq. (4.2), applies to all STZ types. Using Eq. (4.2) with a shear modulus value μ = 16.6 GPa [3], γ_0^T = 0.2 [14,15], and Poisson's ratio = 0.326 [25], we obtained the STZ volume values, Ω_m, as a function of peak index, m (Fig. 4.6), for samples aged $2.9 \cdot 10^7$ s, assumed to have stabilized. The random error in these values is less than 0.7% because Ω_m appears in the exponent in the strain-rate expression [20]. Note that the activation volume is $\gamma_0^T \Omega_m$. The present experiments do not offer an independent determination of μ, γ_0^T, and Ω_m, but the latter two are determined independently in a separate study [26]. As in Fig. 4.5(a), two different linear regimes are observed, indicated by two fit lines. The fit quality is good, with R^2 values of 0.999 for each. The slope in Fig. 4.6 corresponds

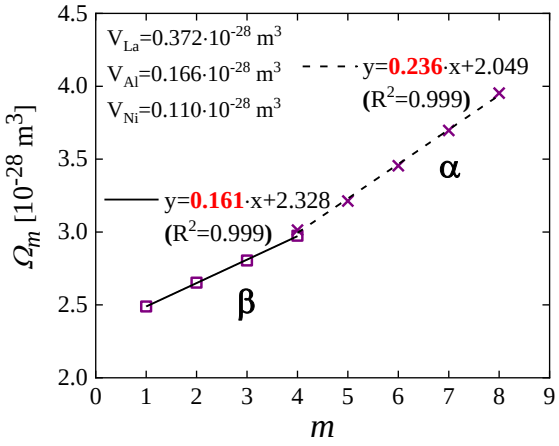

Figure 4.6. STZ volume (Ω_m) as a function STZ type (m) for samples aged 2.9·10^7 s. The error bars, < 0.7%, are smaller than the symbols. The slopes correspond to the volume increment between two adjacent Ω_m values. The random error in these slopes is 2-3%.

to the volume increment between two adjacent Ω_m values. The slope for the first regime, which corresponds to the β relaxation, is 0.161·10^{-28} m^3, close to the atomic volume of elemental Al, 0.166·10^{-28} m^3. For comparison, the atomic volumes of elemental Ni and La are 0.110·10^{-28} m^3 and 0.372·10^{-28} m^3, respectively. For the second regime, the slope, corresponding to the α relaxation, is 0.236·10^{-28} m^3, close to the average atomic volume of the alloy, 0.267·10^{-28} m^3. The random error in these slopes is 2-3%. These results suggest that Al atoms are more likely involved in the β relaxation, while the α relaxation involves all constituent elements. One could argue that the transformation shear strain, γ_0^T, may be smaller for small STZs. However, the opposite trend is expected if a shear transformation involves atomic displacements to the nearest potential well. For comparison, Ju *et al.* [14] observed the same volume increment for all STZs corresponding to either α or β relaxations in an alloy with 86.8% Al. The two regimes we observe suggest a possible chemical composition dependence between the STZs corresponding to the two relaxation modes.

To explore the reason for the increase in relaxation time constants with ageing time, we employ Eq. (4.2) for the relaxation time constant of *m*-type STZs [12]. In it, the only parameter expected to evolve significantly with ageing time is the shear modulus, μ. The contribution of the last term ($\overline{\sigma_{STZ}}/\mu$) is insignificant [20]. Since the effect of structural relaxation on STZ volume is expected to be negligible, the same STZ volume values as in Fig. 4.6 are now assumed for all ageing times in the computation of μ. Its evolution with ageing time, obtained from mandrel measurements, is shown in Fig. 4.7. It exhibits a ~ 5% increase during RT structural relaxation, which is consistent with other reports [15,27]. It is important to note that the trend in μ is not observed for small and fast STZs from cantilever bending, for which the time constants are unaffected by ageing. This suggests that the STZ continuum elastic model may not apply for smaller and faster STZs [5]. In such a case, an alternative interpretation of the smaller slope in Fig. 4.6 becomes necessary. In this context, we note that Lerner and Bouchbinder [28], using molecular dynamics, observed that relaxation dynamics of local strain dipoles are a function of the local modulus instead of its bulk-averaged value.

Figure 4.8 shows the volume fraction occupied by *m*-type *potential* STZs, c_m (Eq. 4.3),as a function of activation free energy ΔF_m (Eq. 4.1), for different RT ageing times. Recall that $\Delta F_m \propto \Omega_m$, and note that ΔF_m evolves with ageing, as it is a function of the shear modulus. The trend for each STZ type is indicated by a dashed line with arrows. The random error is small, indicating high reproducibility. With increasing ageing time, c_m does not vary significantly up to m = 7, but c_8 decreases dramatically. One possible artifact needs to be addressed here: For RT ageing time up to $5.2 \cdot 10^6$ s, the time constants of all active STZs are smaller than the constraining time, so mechanical equilibrium at the end of the constraining period can be assumed, and c_8 values are

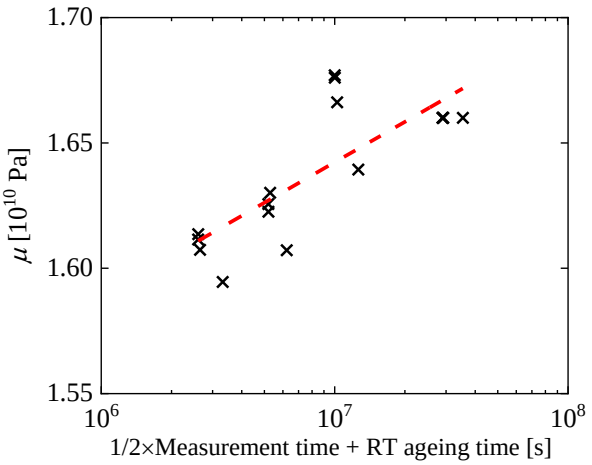

Figure 4.7. Calculated evolution of shear modulus (μ) during RT structural relaxation. The abscissa is a sum of RT ageing time and half of measurement time, a rough estimate necessary since samples undergo structural relaxation during the measurement, and both the ageing time and measurement time are of similar orders of magnitude.

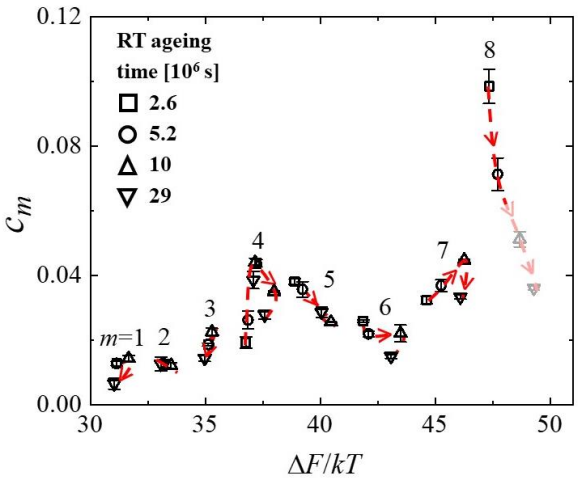

Figure 4.8. Volume fraction occupied by *m*-type *potential* STZs, Eq. (4.3), as a function of activation free energy ΔF_m, Eq. (4.1), divided by k*T*, for different RT ageing times. Each symbol corresponds to one ageing-time value. The error bars for ΔF/k*T* are smaller than the symbols. Arrows show the direction of evolution with RT ageing for each *m*. *m* = 6-8 and beyond (not active at RT within the time range used) correspond to the α relaxation, and $m \leq 5$ correspond to the β relaxation. The last two data points for *m* = 8 STZs represent an underestimate due to lack of mechanical equilibration at the end of the constraining period for samples with long ageing time and associated long τ_8 values (see discussion).

reliable. However, since τ_8 increases with ageing time, it becomes larger than the constraining time for RT ageing times equal to and greater than $1.0 \cdot 10^7$ s, which makes it important to consider the absence of mechanical equilibration for $m = 8$ at the end of the constraining period.

Table 4.1 lists τ_8 values for different ageing times in the present study and Ref. [14]. It is seen that τ_8 is greater than the constraining time for $La_{55}Ni_{20}Al_{25}$ aged for $t_a = 1.0 \cdot 10^7$ s and $2.9 \cdot 10^7$ s, causing an underestimation in the corresponding c_8 values. Ju *et al*. calculated the correction to c_8 for $Al_{86.8}Ni_{3.7}Y_{9.5}$ MG, but later measurement with longer constraining time showed that the magnitude of this correction was overestimated [14,19]. In Ref. [15], Lei *et al*. concluded for

Table 4.1. Apparent and actual volume fraction of the largest *potential* STZ type, c_8, for $Al_{86.8}Ni_{3.7}Y_{9.5}$ [14,19] and $La_{55}Ni_{20}Al_{25}$ MGs with different RT ageing times. τ_8 and c_8 (apparent) are the time constant of $m = 8$ STZs and volume fraction of $m = 8$ *potential* STZs, respectively, obtained from stress-free relaxation spectra following constraining for $2.0 \cdot 10^6$ s. c_8 (apparent) values are underestimated for ageing times $1.0 \cdot 10^7$ s and $2.9 \cdot 10^7$ s. c_8 (actual) is the volume fraction of $m = 8$ *potential* STZs that would be obtained from stress-free relaxation after reaching mechanical equilibrium under constraint.

MGs	RT Ageing Time [s]	τ_8 [s]	τ_8 > Constraining Time = $2.0 \cdot 10^6$ s	c_8 (apparent), obtained after constraining for $2.0 \cdot 10^6$ s	c_8 (actual)
$Al_{86.8}Ni_{3.7}Y_{9.5}$	*	$1.25 \cdot 10^7$	Yes	0.06	0.12**
$La_{55}Ni_{20}Al_{25}$	$2.6 \cdot 10^6$	$1.46 \cdot 10^6$	No	0.1	0.1
	$5.2 \cdot 10^6$	$2.0 \cdot 10^6$	No	0.072	0.072
	$1.0 \cdot 10^7$	$5.2 \cdot 10^6$	Yes	0.051	
	$2.9 \cdot 10^7$	$9.6 \cdot 10^6$	Yes	0.036	<0.072***

* RT ageing does not affect this MG.

** Obtained after a constraining time of $4.4 \cdot 10^7$ s.

*** Estimated – see discussion.

$La_{70}(Ni_xCu_{1-x})_{15}Al_{15}$, x = 0, 1, that the underestimation for the *c* values of un-equilibrated largest STZs was insignificant, based on additional information from cryogenically cycled samples. Presently, even though the c_8 values for RT ageing times $1.0 \cdot 10^7$ s and $2.9 \cdot 10^7$ s in Fig. 4.8 are underestimated, we argue that the decreasing trend of c_8 persists with increasing ageing time, as shown in the column "c_8 (actual)" in Table 4.1. The following details the reasoning: In Ref. 19, for $Al_{86.8}Ni_{3.7}Y_{9.5}$ MG with $\tau_8 = 1.25 \cdot 10^7$ s, the actual c_8 value, obtained for longer constraining time, is twice that of the apparent value obtained from stress-free relaxation following constraining for $2.0 \cdot 10^6$ s (Table 4.1) [14]. In the present study, for $La_{55}Ni_{20}Al_{25}$ MG with RT ageing time $2.9 \cdot 10^7$ s, $\tau_8 = 9.6 \cdot 10^6$ s is smaller than that of the Al-based MG while the constraining time is the same. As a result, the apparent value of c_8 is closer to its actual value for the La-based MG than for the Al-based MG [14]. Therefore, the actual c_8 value for $La_{55}Ni_{20}Al_{25}$ should be smaller than twice that of the apparent value, as shown in Table 4.1. We conclude that the decrease of c_8 with increasing ageing time persists for RT ageing time $2.6 \cdot 10^6$ s, $5.2 \cdot 10^6$ s, and $2.9 \cdot 10^7$ s. It is unlikely that c_8 for the RT ageing time $1.0 \cdot 10^7$ s deviates from this trend. In summary, we observe that among all *m* values, RT ageing increases τ_8, and reduces c_8, the most.

Atzmon and Ju reported that for $Al_{86.8}Ni_{3.7}Y_{9.5}$ MG, c_m increased monotonically with *m*, and annealing decreased c_m without affecting τ_m [19]. Structural relaxation only decreased the number of *potential* STZs while leaving their properties unchanged. Presently, for $La_{55}Ni_{20}Al_{25}$, c_m is not monotonic in *m* (Fig. 4.8), reflecting the fact that the β relaxation is more pronounced. The peak in Fig. 4.8 at $\Delta F/kT \sim$ 31-40, associated with small and fast STZs, corresponds to the high-frequency/low-temperature β relaxation in the loss modulus [18]. The role of small and fast STZs in the β relaxation was also observed in atomistic simulations [29]. Some studies suggest that only

the β relaxation occurs by shear transformations [30], but our data and analysis show consistency with the STZ model for both α and β relaxations [12], albeit with likely different compositions. In contrast to Ref. 19, we observe ageing to not only decrease c_m, but also increase τ_m, as we also observed in two other La-based alloys [15].

A main motivation for the present work has been to understand alloy plasticity. We propose the following as a preliminary conclusion: a large concentration of *potential* STZs favors simultaneous shear transformations in the entire sample and therefore homogeneous strain. In contrast, when the concentration of *potential* STZs is smaller, increasing local stress favors athermal, autocatalytic, strain evolution, shear bands and catastrophic failure. Such a scenario explains why structural relaxation leads to embrittlement [31]. Along the same lines, separate from a temperature effect on relaxation or rejuvenation, an increasing temperature under isoconfigurational conditions [32] allows activation of additional, larger, STZs, explaining the increase in plasticity with temperature [16]. In fact, extrapolation of Fig. 4.8 suggests a further increasing volume fraction with increasing STZ size. Similarly, with decreasing strain rate, larger and slower STZs contribute to the strain, also in agreement with Ref. 16. Finally, the origin of the correlation between the relative intensity of the β relaxation and plasticity is still open and the subject of further work.

4.5 Conclusions

The $La_{55}Ni_{20}Al_{25}$ metallic glass studied has offered an opportunity to compare the properties of α and β relaxations in unprecedented detail. While an atomically quantized hierarchy of shear transformation zones is observed for the entire range of anelastic relaxation, there is a distinct

difference between α and β regime. For the former, the time constants increase, and the number of the largest and slowest *potential* STZs decreases, upon structural relaxation. No effect of structural relaxation is observed for the latter. The effect of structural relaxation on the α relaxation can be explained on the basis of an increase in shear modulus, leaving open question as to the absence of such an effect for the small and fast STZs corresponding to β relaxation. The activation-volume increment in the hierarchy is smaller for β relaxation than for α relaxation, suggesting that Al atoms dominate the STZs associated with β relaxation, whereas all constituent elements possibly participate in STZs associated with α relaxation.

4.6 References

[4.1] C. C. Hays, C. P. Kim, and W. L. Johnson, *Phys. Rev. Lett.* **84**, 2901 (2000).

[4.2] M. M. Trexler and N. N. Thadhani, *Prog. Mater. Sci.* **55**, 759 (2010).

[4.3] S. V. Ketov, Y. H. Sun, S. Nachum, Z. Lu, A. Checchi, A. R. Beraldin, H. Y. Bai, W. H. Wang, D. V. Louzguine-Luzgin, M. A. Carpenter, and A. L. Greer, *Nature* **524**, 200 (2015).

[4.4] D. Jang and J. R. Greer, *Nat. Mater.* **9**, 215 (2010).

[4.5] A. S. Argon, *Acta Metall.* **27**, 47 (1979).

[4.6] M. L. Falk and J. S. Langer, *Phys. Rev. E* **57**, 7192 (1998).

[4.7] G. P. Johari and M. Goldstein, *J. Chem. Phys.* **53**, 2372 (1970).

[4.8] Z. Wang, H. B. Yu, P. Wen, H. Y. Bai, and W. H. Wang, *J. Phys.: Condens. Matter* **23**, 142202 (2011).

[4.9] Q. Wang, S. T. Zhang, Y. Yang, Y. D. Dong, C. T. Liu, and J. Lu, *Nat. Commun.* **6**, 7876 (2015).

[4.10] B. Ruta, Y. Chushkin, G. Monaco, L. Cipelletti, V. M. Giordano, E. Pineda, and P. Bruna, *AIP Conf. Proc.* **1518**, 181 (2013).

[4.11] M. Atzmon, *J. Appl. Phys.* **123**, 065103 (2018).

[4.12] J. D. Ju and M. Atzmon, *MRS Commun.* **4**, 63 (2014).

[4.13] J. D. Ju and M. Atzmon, *Acta Mater.* **74**, 183 (2014).

[4.14] J. D. Ju, D. Jang, A. Nwankpa, and M. Atzmon, *J. Appl. Phys.* **109**, 053522 (2011).

[4.15] T. J. Lei, R. Rangel DaCosta, M. Liu, W. H. Wang, Y. H. Sun, A. L. Greer, and M. Atzmon, *Acta Mater.* **164**, 165 (2019).

[4.16] H. B. Yu, X. Shen, Z. Wang, L. Gu, W. H. Wang, and H. Y. Bai, *Phys. Rev. Lett.* **108**, 015504 (2012).

[4.17] H. B. Yu, W. H. Wang, and H. Y. Bai, *Phys. Rev. B* **81**, 220201(R) (2010).

[4.18] H. Okumura, H. S. Chen, A. Inoue, and T. Masumoto, J. *Non-Cryst. Solids* **130**, 304 (1991).

[4.19] M. Atzmon and J. D. Ju, *Phys. Rev. E* **90**, 042313 (2014).

[4.20] A. S. Argon and L. T. Shi, *Acta Metall.* **31**, 499 (1983).

[4.21] H. Kato, H. Igarashi, and A. Inoue, *Mater. Lett.* **62**, 1592 (2008).

[4.22] S. W. Provencher, *Comput. Phys. Commun.* **27**, 213 (1982).

[4.23] S. W. Provencher, *Comput. Phys. Commun.* **27**, 229 (1982).

[4.24] A. Castellero, B. Moser, D. I. Uhlenhaut, F. H. Dalla Torre, and J. F. Löffler, *Acta Mater.* **56,** 3777 (2008).

[4.25] S. T. Liu, Z. Wang, H. L. Peng, H. B. Yu, and W. H. Wang, *Scr. Mater.* **67**, 9 (2012).

[4.26] T. J. Lei and M. Atzmon, *J. Appl. Phys.* **126**, 18 (2019).

[4.27] H. S. Chen, *J. Appl. Phys.* **49**, 3289 (1978).

[4.28] E. Lerner and E. Bouchbinder, *J. Chem. Phys.* **148**, 214502 (2018).

[4.29] Y. Fan, T. Iwashita, and T. Egami, *Nat. Commun.* **5**, 5083 (2014).

[4.30] J. Chao, J.-M. Pelletier, and R. Casalini, *J. Phys. Chem. B* **117**, 13658 (2013).

[4.31] R. Raghavan, P. Murali, U. Ramamurty, *Acta Mater.* **57**, 3332 (2009).

[4.32] A. I. Taub and F. Spaepen, *Acta Metall.* **28**, 1781 (1980).

CHAPTER 5

Microscopic Characterization of Structural Relaxation and Cryogenic Rejuvenation in $La_{70}(Cu_xNi_{1-x})_{15}Al_{15}$, x=0 or 1 Metallic Glasses

Reprinted with permission from T. J. Lei, L. Rangel DaCosta, M. Liu, W. H. Wang, Y. H. Sun, A. L. Greer, and M. Atzmon, "Microscopic characterization of structural relaxation and cryogenic rejuvenation in metallic glasses," Acta Mater. 164, 165 (2019).

5.1 Introduction

Metallic glasses (MGs) have been considered as potential structural materials owing to their high strength and elastic limit [1]. However, they exhibit little macroscopic plasticity due to shear band formation, which limits their practical applications [2]. Rejuvenation is one approach to enhancing the plasticity of MGs, which involves structural excitation and an increase in stored energy [3]. Different methods are used for rejuvenation, such as cyclic elastic loading [4], constrained loading [5], and irradiation [6,7]. The recent discovery of improved mechanical properties of MGs resulting from cryogenic cycling between room temperature (RT) and liquid nitrogen temperature has attracted much attention, since this method is non-destructive, isotropic and controllable [8,9,10,11]. The authors attributed the effect to a non-uniform structure and associated thermal expansion coefficient. However, microscopic details are still missing.

Due to their disordered atomic structure, it is challenging to define flow defects in MGs. Based on observation of two-dimensional bubble rafts, Argon [12] proposed that atomic clusters, termed shear transformation zones (STZs) [13], accommodate inelastic deformation of MGs. At small strain, STZs are isolated and can be reversed upon removal of the stress due to the back stress in the elastic matrix, which results in anelasticity. With increasing strain, STZs begin to interact with each other, back stress in the elastic matrix is lost, and the strain is permanent. Numerous experiments and simulations [14,15,16] have been conducted to characterize STZs, with some ambiguous results.

Recently, Ju *et al.* [17] analyzed relaxation-time spectra, $f(\tau)$, obtained from quasi-static anelastic relaxation measurements for an Al-based MG at RT. Since the strain was small, within the nominally elastic regime, STZs were in the dilute limit and did not interact with each other. Two techniques, nanoindenter cantilever bending for short-time measurements and bend relaxation for longer time, were employed to observe the anelastic strain evolution. For the latter, samples were constrained around a mandrel for $2 \cdot 10^6$ s, then relaxed stress-free. The evolution in radius of curvature was then monitored from ~ 10^3 s to $3.1 \cdot 10^7$ s. Nonlinear least-squares fits were employed to obtain relaxation-time spectra, which exhibited distinct peaks corresponding to different STZ types. The time constant of each type is an increasing function of its volume. Surprisingly, an atomically quantized hierarchy of STZs was observed: the STZ volume values computed for the peaks were spaced by the atomic volume of Al, the majority element.

In this chapter, we use a similar approach to study the effect of RT ageing and cryogenic cycling on two La-based MGs by characterizing their anelastic time-constant spectra at RT. The magnitude of the anelastic strain induced after ageing decreases with increasing ageing time, at a relative rate that varies with the corresponding time constant. Cryogenic cycling, after ageing and prior to anelastic deformation, does *not* change the magnitude of the strain. Ageing also increases the relaxation time constants and results in more-distinct spectrum peaks – trends that *are* reversed by cycling. These observations are discussed in terms of STZ properties.

5.2 Experiment and Analysis Procedure

Two alloy compositions, $La_{70}Cu_{15}Al_{15}$ and $La_{70}Ni_{15}Al_{15}$ (at.%), have been investigated. Their glass transition temperatures are 391 K and 431 K, respectively [18]. Ribbons ~ 40 μm thick and 1 mm wide, were obtained by single-wheel melt-spinning, using a Cr-coated Cu wheel, at a tangential velocity of ~ 3 m/s in an argon atmosphere with a pressure of 20 kPa. X-ray diffraction was employed to confirm the amorphous structure. Since these alloys undergo structural relaxation at RT, samples with RT (293.0 ± 1 K) ageing time ranging from $1.9 \cdot 10^6$ s to $2.9 \cdot 10^7$ s were used, 3-8 samples for each condition. Samples aged for $1.0 \cdot 10^7$ s were also subsequently cycled between RT and liquid nitrogen temperature ten times, with 3 minutes and 1-minute holding time, respectively.

The following thermomechanical treatment and measurement sequence was applied to 1 cm long ribbon segments, as also illustrated in Fig. 5.1: After ageing with or without subsequent cryogenic cycling, bend-relaxation measurements were performed at RT. Samples were constrained around mandrels of radii R ranging from 0.348 cm to 0.802 cm for a standard time of $2.0 \cdot 10^6$ s.

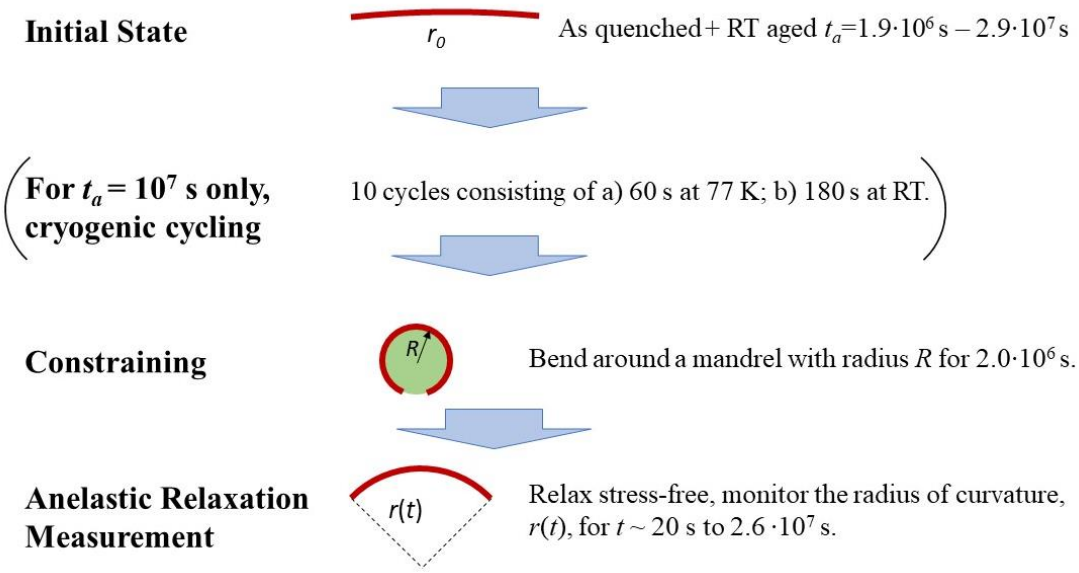

Figure 5.1. Schematic illustration of the thermomechanical treatment and measurement sequence.

Subsequently, the stress-free evolution of radius of curvature, $r(t)$, was monitored for up to $2.6 \cdot 10^7$ s using a digital camera, taking care to align its optical axis perpendicular to the sample plane. An automated image analysis method was developed for curvature determination, significantly reducing the error bars in the strain vs. time curves. The maximum equilibrium elastic strain at the end of the constraining period, and the anelastic strain at time t after constraint removal, both attained at the surface, are $\varepsilon_{el}^0 = d/2 \cdot [1/R - 1/r(0)]$ and $\varepsilon_{an}(t) = d/2 \cdot [1/r(t) - 1/r_0]$, respectively, where d is the sample thickness and r_0 is the radius of curvature before constraint [17].

In order to estimate the effect of cryogenic treatment on elastic properties, Young's modulus was measured. RT tensile tests were performed at a strain rate of 10^{-3} s^{-1}, using a TA Instruments RSA III Dynamic Mechanical Analyzer. Pairs of neighboring ribbon segments with identical ageing time were used. One segment of each pair was also subjected to 10 cryogenic cycles after ageing.

Uncertainty in sample dimensions was thus essentially canceled out in the relative difference in modulus. Four sample pairs were used for each alloy type and ageing time.

To obtain relaxation-time spectra $f(\tau)$, CONTIN, a portable package for inverse problems, was employed to yield stable and consistent fitting of $\varepsilon_{an}(t)/\varepsilon_{el}^{0}$ [19,20]: based on a linear solid model [17], $\varepsilon_{an}(t)/\varepsilon_{el}^{0} = c_{\infty} + \sum_{i=1}^{N} \varepsilon_i \exp(-t/\tau_i)$, where c_{∞} and ε_i are fitting parameters. The relaxation-time values, τ_i, i=1, …, N=50, less than the number of data points, are logarithmically spaced. The continuous spectra were approximated as:

$$f(\tau_i) = \varepsilon_i/\Delta \ln \tau, \tag{5.1}$$

where $\Delta \ln \tau = \ln[\tau_{max}/\tau_{min}]\ /(N-1)$ with $\tau_{min} = 10$ s and $\tau_{max} = 5.2 \cdot 10^{7}$s. The additive term, c_{∞}, was included in the fits to account for processes with time constants longer than τ_{max}. A regularization term was used in the optimization procedure [19,20], which eliminates sharp, unphysical, variations in the spectrum due to numerical artifacts. For consistency, similar regularization parameters were used for all samples. Within a range of regularization parameter values, the spectrum does not change significantly. Ref. [17] contains further details on fitting and consistency checks.

The normalization of $f(\tau)$ in Eq. (5.1) was chosen for convenient analysis on a logarithmic scale [17, 21] since the time constants spanned several orders of magnitude. $\varepsilon_{an}(t=0)/\varepsilon_{el}^{0} = \int_{0}^{\infty} f(\tau) d\ln\tau$. $\int_{\tau_1}^{\tau_2} f(\tau) \mathrm{d}\ln\tau$ is equal to the normalized anelastic strain with time constants in the range (τ_1, τ_2). According to Ref. [17], this latter integral is also equal to the volume fraction

occupied by *potential* STZs with time constants in the corresponding range. *Potential* STZs are clusters of atoms capable of undergoing a shear transformation. Finally, peak properties were determined from an average over all samples for a given temperature history. The error bars are the standard deviations of the mean.

5.3 Results and Discussion

Figure 5.2 shows representative normalized anelastic strain relaxation data, $\varepsilon_{an}(t)/\varepsilon_{el}^{0}$, for $La_{70}Cu_{15}Al_{15}$ and $La_{70}Ni_{15}Al_{15}$ ribbons, aged for different lengths of time, with and without cryogenic cycling treatment prior to bending. One observes a remarkable decrease of $\varepsilon_{an}(t=0)/\varepsilon_{el}^{0}$ with structural relaxation: The "youngest" sample, aged $1.9{\cdot}10^{6}$ s, exhibits the largest value of $\varepsilon_{an}(0)/\varepsilon_{el}^{0}$, 1.24 and 0.67 for $La_{70}Cu_{15}Al_{15}$ and $La_{70}Ni_{15}Al_{15}$, respectively, as

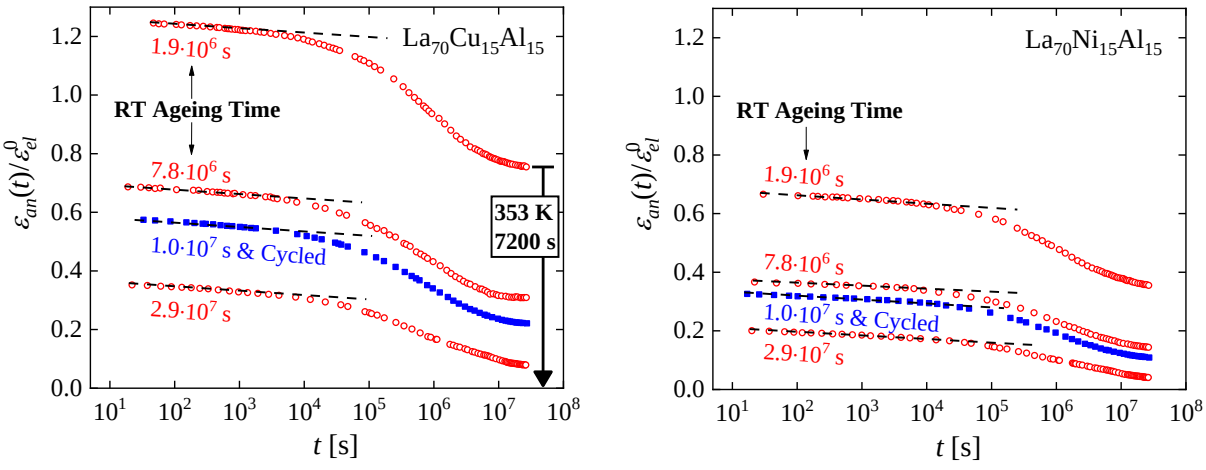

Figure 5.2. Normalized anelastic strain of $La_{70}Cu_{15}Al_{15}$ and $La_{70}Ni_{15}Al_{15}$ as a function of time for different ageing times prior to bending, as indicated. Open circles and filled squares correspond, respectively, to measurements without and with cryogenic cycling after ageing, prior to bending. Curves are not shifted. The dashed lines are all drawn with the same slope. Note that the entire strain is anelastic, as verified by annealing at temperature above RT (bold arrow).

compared with 0.35 and 0.20 for ageing time of $2.9 \cdot 10^7$ s. This observation implies that structural relaxation leads to a significant decrease of the volume fraction occupied by *potential* STZs. It is noteworthy that the initial anelastic strain of the "youngest" $La_{70}Cu_{15}Al_{15}$ sample is greater than the elastic strain, ε_{el}^0. Cryogenic cycling does not affect $\varepsilon_{an}(0)/\varepsilon_{el}^0$, as discussed further below.

The following discussion addresses the details of the effect of ageing on *potential* STZs, as resolved by their size/time constant. At short measurement time, up to ~ 10^4 s, the absolute strain relaxation rate is the same for varying prior thermal history, as indicated by the dashed lines, all drawn with the same slope. However, the strain evolution at longer time depends on the prior ageing time, as "younger" samples have higher strain that decreases faster. Comparing the two alloys at the same ageing time, the overall strain magnitude of $La_{70}Cu_{15}Al_{15}$ is higher than that of $La_{70}Ni_{15}Al_{15}$. However, the slope at short measurement time is very similar for both alloys, as indicated by the dashed lines. This indicates that the difference in strain between the two alloys is mainly due to STZs with large time constants. The large amount of strain at the end of the measurement time could be either permanent or anelastic with time constants greater than those measured. However, annealing for 7200 s at 353 K restored the radius of curvature to its initial value, r_0 (See Fig. 5.2), proving that the entire strain measured is anelastic. These observations are a manifestation of the fact that anelastic processes with large time constants can be induced during a much shorter time. In summary, we observe a significant effect of alloy composition and structural relaxation on the anelastic strain magnitude, and on its evolution rate for $t \geq 10^4$ s.

The effect of cryogenic cycling on anelastic relaxation is not obvious in Fig. 5.2. Ideally, one would compare samples aged for the same duration with and without subsequent cryogenic cycling treatment. We have observed the same value, within error, of $\varepsilon_{an}(t=0)/\varepsilon_{el}^{0}$ for samples aged $6.2{\cdot}10^{7}$ s with and without cryogenic cycling. Among samples for which we have full $\varepsilon_{an}(t)$ data, the ageing time of samples with cryogenic cycling is $1.0{\cdot}10^{7}$ s, and the closest ageing time of samples without cycling is $7.8{\cdot}10^{6}$ s. The trends with ageing time will allow us to further examine the effect of cycling. In Ref. [8], the compressive plastic strain of MGs increases significantly by successive cryogenic cycles. This effect is strongest for partially relaxed samples, and insignificant for fully relaxed samples. In contrast, in the present study, in which all samples are partially relaxed, cycling does not cause any noticeable deviation from the trend in anelastic strain magnitude with ageing. Further details are now examined by computing the spectra corresponding to Fig. 5.2.

Figure 5.3 shows the relaxation-time spectra computed from Fig. 5.2, shifted vertically for clarity. Two representative spectra are shown for each temperature history, demonstrating reproducibility. All spectra exhibit distinct peaks, which we associate with distinct STZ types, numbered *m*=1, 2, …, 6 (see below), based on shape similarity between spectra. It should be noted that 3 out of 8 samples with cryogenic cycling show subtle shoulders at large time constants for each alloy. Because of uncertainty in the spectra, we do not consider these shoulders significant.

With increasing ageing time, for samples without cryogenic cycling, the peak positions shift to longer time, while their intensities decrease. The last two peaks also become more distinct. The

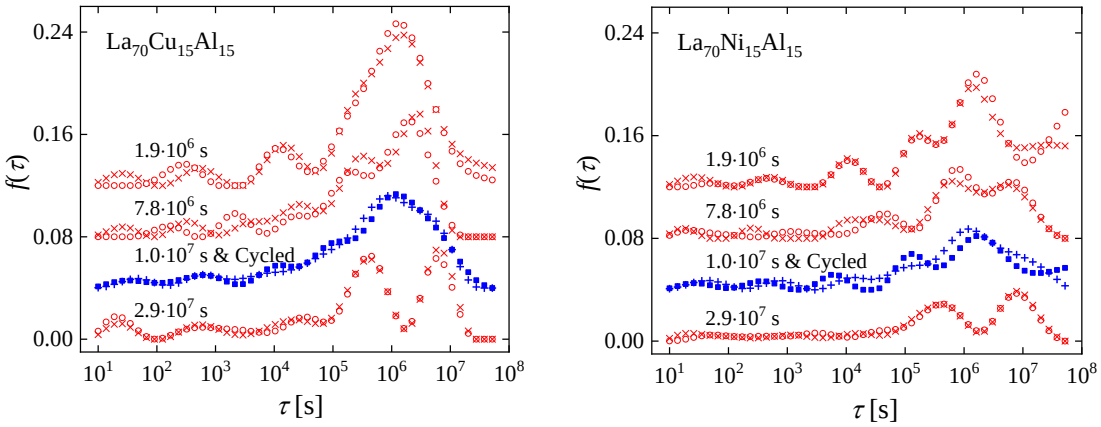

Figure 5.3. Relaxation-time spectra for $La_{70}Cu_{15}Al_{15}$ and $La_{70}Ni_{15}Al_{15}$ with different ageing times, as indicated. For each condition, representative data for two independent samples are shown. Open circles and crosses, vs. filled squares and pluses, correspond to samples without, vs. with, cryogenic cycling, respectively. The curves are shifted vertically for clarity.

spectra for samples aged $1.0 \cdot 10^7$ s and cryogenically cycled resemble those for the "youngest" samples (aged $1.9 \cdot 10^6$ s) in peak position and shape: cycling has reversed the ageing-induced increase in time constants, and for $La_{70}Cu_{15}Al_{15}$, it also re-blurred the peaks. It should be noted that this is not an artifact of data quality or spectrum computation: samples with cryogenic cycling yield fits of equal quality, and similar regularization parameters are used for all samples.

In agreement with the strain curves, the peak intensities for large time constants for $La_{70}Cu_{15}Al_{15}$ in Fig. 5.3 are in general higher than for $La_{70}Ni_{15}Al_{15}$. As an aside, this is the reason that the high frequency beta relaxation in the loss modulus appears more pronounced in $La_{70}Ni_{15}Al_{15}$ than in $La_{70}Cu_{15}Al_{15}$ [22], since it is common to normalize loss modulus data by the peak height of the slower alpha relaxation. The spectra in Fig. 5.3 correspond to the slow alpha relaxation, whereas the faster beta relaxation has τ values generally below those in Fig. 5.3. Spectra corresponding to

such τ values have been obtained from nanoindenter cantilever measurements, and will be presented elsewhere [23].

As in Ref. [17], we interpret the spectrum peaks as representing an atomically quantized hierarchy of STZs, and expect further peaks above 10^8 s, if measured. Ju *et al.* [17] showed that the area of peak *m*, $c_m = \int_m f(\tau) d \ln \tau$, is equal to the volume fraction occupied by *potential m*-type STZs. As seen in Figs. 5.2 & 5.3, the main contributions to the anelastic strain are due to the high end of the spectrum, above ~10^4 s, plus the yet slower STZs represented by the constant term, $c_\infty (= \sum_{m>6} c_m)$, used in the spectrum fit for $\varepsilon_{an}(t)/\varepsilon_{el}^0$. The latter STZs would only be visibly reversed over times longer than the measurement time used, or at elevated temperature (see above).

In order to further examine the effect of ageing and cryogenic cycling, the following are shown in Fig. 5.4 as a function of RT ageing time: a) the volume fraction occupied by *potential* STZs of all types, *m*, given by $c_{total} = \varepsilon_{an}(t = 0)/\varepsilon_{el}^0$, which is equal to c_∞ *plus* the integrated area of the entire spectrum [17]; b) the volume fraction occupied by *potential m*=5 & *m*=6 STZs, $c_{5,6}$, equal to the integrated area of the corresponding peaks; c) the volume fraction, c_∞, occupied by *potential* STZs with $\tau > \tau_{max}$. Note that $c_{total} > 1$ for $La_{70}Cu_{15}Al_{15}$ (Fig. 5.2) is physically meaningful, as discussed in Ref. [17], since the definition of *c* is based on multiple counting of volume elements contained in more than one *potential* STZ. The error bars in Fig. 5.4 are small, indicating reproducibility. All curves decrease with increasing ageing time, but c_∞, the contribution due to time constants larger than those included in the spectrum, clearly decreases at a higher absolute or relative rate than $c_{5,6}$ does. Samples with cryogenic cycling fit well the trend of each curve,

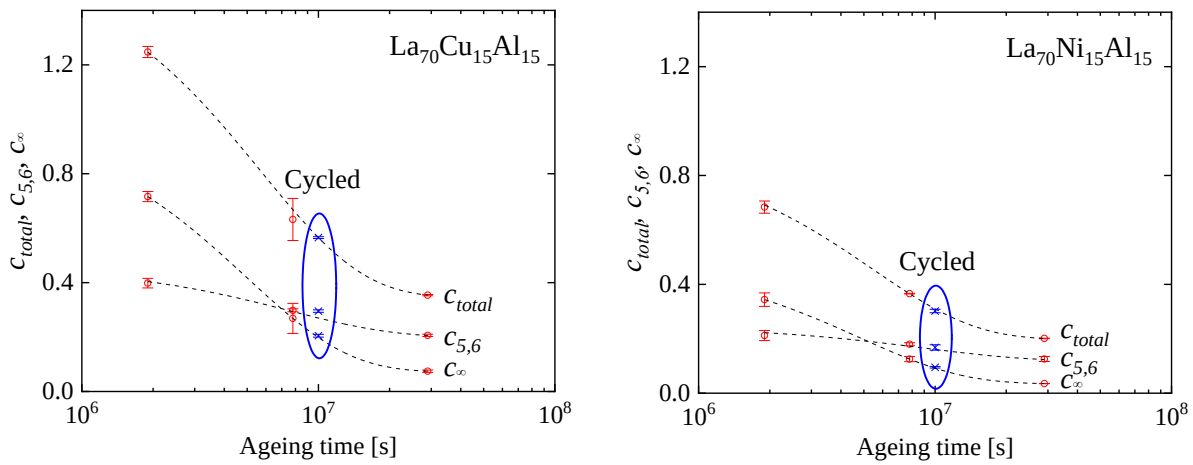

Figure 5.4. c_{total}, the integrated area of the entire spectrum plus the constant in the spectrum fit, $c_{5,6}$, the integrated area of the last two peaks and c_∞ vs. aging time for $La_{70}Cu_{15}Al_{15}$ and $La_{70}Ni_{15}Al_{15}$ MGs. Lines are a guide to the eye.

indicating that cryogenic cycling prior to bending has not noticeably affected the volume fraction occupied by *potential* STZs of any type/size. Also, as mentioned above, for samples aged $6.2 \cdot 10^7$ s, cryogenic cycling does not affect $c_{total} = \varepsilon_{an}(t = 0)/\varepsilon_{el}^0$.

It is likely that each c_m evolves with ageing time, t_a, as $c_{m,\infty}^0 + g_m(t_a)$, where $c_{m,\infty}^0$ is the limiting value for the glass at internal equilibrium, and $g_m(t_a)$ is a function that decays to zero at long time. The small number of data points in Fig. 5.4 is insufficient for determining detailed ageing kinetics for each STZ type or range of τ. However, it is clear that $g_m(t_a)$ consists of contributions with time constants much longer than the corresponding τ_m. For example, c_∞, the sum of the contributions with time constants $\tau > \tau_{max}$ decreases dramatically during ageing times shorter than 10^7 s. In other words, one cannot directly associate the time constant for a particular anelastic process with its time constant for ageing. We note that while $c_\infty = (\sum_{m>6} c_m) > (c_5 + c_6)$ for

short ageing times, the reverse is true for long ageing times, and it appears that $\sum_{m>6} c^0_{m,\infty} \ll \left(c^0_{5,\infty} + c^0_{6,\infty}\right)$.

The analysis we present above assumes implicitly that all anelastic processes reach mechanical equilibrium during the constraining period. Since the constraining time is shorter than the largest time constants that affect measured evolution, it is important to consider the effect of deviations from mechanical equilibrium at the end of the constraining time on *c* values. We first note that the deviation should be smaller than expected from the time constants: Ju *et. al*. [17] calculated the correction to c_8 for the linear solid model used, but later measurements [24] showed that this correction was a large overestimate. (This suggests that the behavior under constraint cannot be perfectly described by the linear solid model.) For RT ageing times less than $2.9 \cdot 10^7$ s, the time constants are smaller than the constraining time, so equilibration can be assumed. For both alloy compositions with RT ageing time $2.9 \cdot 10^7$ s, one expects m=6 STZs to not equilibrate with the elastic strain within the constraining time $t_c << \tau_6$. As a result, the data corresponding to that ageing condition are underestimated in Fig. 5.4. However, the underestimation is insignificant, as we conclude from the cryogenically cycled sample: *c* values (c_{total}, $c_{5,6}$, and c_∞) corresponding to samples with cryogenic cycling still follow the trend of the samples without cryogenic cycling even though their time constants decreased by cryogenic cycling. Based on this discussion, we can also safely assume that for τ_i with $i \leq 5$, their shift does not affect the measured c_i.

Figure 5.5 shows the evolution with ageing of the time constants, τ_m, obtained as the median of each spectrum peak *m*. As mentioned above, *m* values were assigned based on the similar shape of spectra corresponding to different ageing times. The time constants increase with increasing ageing time for samples without cycling. The effect of cryogenic cycling is indicated with arrows, except when *m* assignment is too uncertain for small *m* for $La_{70}Cu_{15}Al_{15}$. A clear trend of decreasing time constants with cryogenic cycling is seen, reversing the prior ageing effect, as also seen in the qualitative features of the spectra.

Ref. [24] reports that for an Al-based MG, annealing at 383 K for 3600 s prior to anelastic relaxation measurement only decreased c_m, but left the peak position unchanged. It followed that structural relaxation only decreased the number of *potential* STZs, without changing their properties. In the present study, too, we observe a decrease in number of *potential* STZs with ageing. This trend is *not* reversed by cryogenic cycling. Unlike in Ref. [24], the time constants

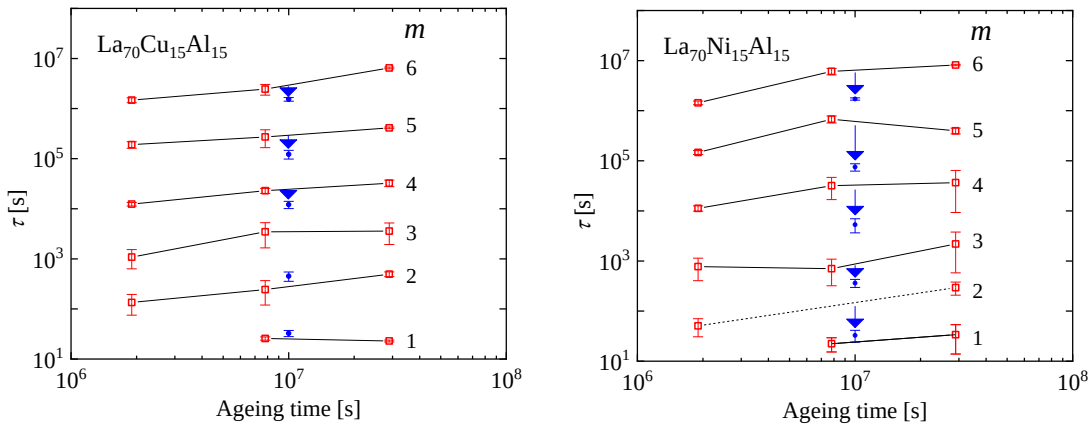

Figure 5.5. The evolution of time constants of different STZ types, *m*, with ageing time for $La_{70}Cu_{15}Al_{15}$ and $La_{70}Ni_{15}Al_{15}$ MGs. Arrows indicate the effect of cryogenic cycling.

increase with increasing ageing time for the present La-based MGs. This increase is completely reversed after cryogenic cycling, pointing to a rejuvenation effect.

The cause of the observed changes in time constant are discussed next. The time constant for anelastic relaxation due to STZs of volume Ω_m is given by [25] as:

$$\tau_m = \frac{3\eta'_m}{E'_m} = \frac{1}{\mu\Omega_m} \cdot \frac{3kT}{2(1+\nu)\gamma_0^c \nu_G \gamma_0^T} \cdot \exp\left(\mu\Omega_m \cdot \left\{\frac{\gamma_0^T}{kT} \cdot \left[\left(\frac{(7-5\nu)}{30(1-\nu)} + \frac{2(1+\nu)}{9(1-\nu)}\bar{\beta}^2\right)\gamma_0^T + \frac{1}{2} \cdot \frac{\overline{\sigma_{STZ}}}{\mu}\right]\right\}\right), \quad (5.2)$$

where η'_m is the effective shear viscosity, E'_m is the effective Young's modulus. $\gamma_0^c = [2(4-5\nu)/15(1-\nu)]\gamma_0^T$ is the transformation shear strain of a constrained STZ with $\gamma_0^T = 0.2$ being the unconstrained transformation shear strain. ν_G is the attempt frequency, k is the Boltzmann's constant and T is the temperature. ν is Poisson's ratio, $\bar{\beta}^2$ is the dilatancy factor, $\overline{\sigma_{STZ}}$ is the shear resistance of the STZ and μ is the shear modulus. Since structural relaxation involves insignificant volume changes, the most likely cause of a shift in time constants is a change in the shear modulus. Based on Eq. (5.2), the present results are consistent with an increase of ~ 5% in shear modulus [23,26].

In order to confirm the role of the shear modulus, Young's modulus was measured. In essentially identical samples, it was lower by 3-7% for samples subjected to cryogenic cycling. No clear trend in this change with composition was observed. Since relative changes in Young's modulus and shear modulus upon structural relaxation have been shown to be very similar [27], this result supports an interpretation that the changes in time constants are due to changes in the shear modulus. In light of the report by Ketov *et al.* [8] that cryogenic cycling of $La_{55}Ni_{20}Al_{25}$ MG did

not change its Young's modulus, further support is given by our observation [23] that cycling led to slight broadening, but no shift, in spectrum peaks for the same alloy. This points to a significant dependence of the behavior on composition.

While a quantitative evaluation of peak widths is not possible for the present data, we observe for $La_{70}Cu_{15}Al_{15}$ evolution toward more-distinct peaks with ageing, which is reversed by cycling. This trend could be influenced by differential changes in position, height and shape of each peak. The latter would point to structural homogenization due to ageing, and the reverse upon cryogenic cycling.

Atzmon and Ju [24] modeled the details of the spectrum of time constants and its change with structural relaxation on the basis of a single parameter – the free volume. The present complex observations are a strong reminder that structural relaxation and rejuvenation cannot be described with a single parameter [28]. We finally note that for a given shear modulus, the present data also yield an STZ volume value for each spectrum peak, as in Ref. [17]. When cantilever measurements of smaller time constants are included, two regimes of volume increment are observed in the STZ hierarchy, which is important for understanding the beta relaxation. This aspect of the study will be published elsewhere [23].

It would be highly desirable to model the observed behavior with atomistic simulations. Since STZs are thermally activated, the time scale accessible by conventional molecular dynamics is far too short for this purpose. Recent work [16,29] has demonstrated progress in atomistic simulations

of glass behavior on longer time scale, and the authors hope it would lead to future simulations of the phenomena they report.

5.4 Conclusions

An unprecedented, detailed, description of the effects of structural relaxation, and rejuvenation by cryogenic cycling, has been obtained. Some of the effects of RT ageing are reversed by cycling, but others are not. RT ageing increases the time constants for anelastic relaxation significantly. It also de-blurs the spectrum features for $La_{70}Cu_{15}Al_{15}$ for long time constants, 10^5 to $>10^7$ s at room temperature. Both effects are reversed by cryogenic cycling, thus exhibiting a rejuvenation effect. The observed changes in time constants are likely due to changes in the shear modulus. Ageing also significantly reduces the volume fraction occupied by *potential* STZs, especially of those with time constants greater than the measurement duration of $2.6 \cdot 10^7$ s. This loss is not recovered by cryogenic cycling. These detailed results are expected to provide important insights into the effects of both ageing and cryogenic cycling on the ductility of metallic glasses.

5.5 References

[5.1] T. C. Hufnagel, C. A. Schuh, M. L. Falk, *Acta Mater.* **109**, 375 (2016).

[5.2] C. C. Hays, C. P. Kim, W. L. Johnson, *Phys. Rev. Lett.* **84**, 2901 (2000).

[5.3] P. M. Derlet, R. Maaβ, *J. Mater. Res.* **32**, 2668 (2017).

[5.4] D. V Louzguine-Luzgin, V. Y. Zadorozhnyy, S. V Ketov, Z. Wang, A. A. Tsarkov, A. L. Greer, *Acta Mater.* **129**, 343 (2017).

[5.5] J. Pan, Y. X. Wang, Q. Guo, D. Zhang, A. L. Greer, Y. Li, *Nat Commun.* **9**, 560 (2018).

[5.6] D. J. Magagnosc, G. Kumar, J. Schroers, P. Felfer, J. M. Cairney, D. S. Gianola, *Acta Mater.* **74**, 165 (2014).

[5.7] J. Heo, S. Kim, S. Ryu, D. Jang, *Sci Rep.* **6**, 23244 (2016).

[5.8] S. V Ketov, Y. H. Sun, S. Nachum, Z. Lu, A. Checchi, A. R. Beraldin, H. Y. Bai, W. H. Wang, D. V Louzguine-Luzgin, M. A. Carpenter, A. L. Greer, *Nature* **524**, 200 (2015).

[5.9] N. Miyazaki, M. Wakeda, Y. J. Wang, S. Ogata, *Npj Comput. Mater.* **2**, 16013 (2016).

[5.10] S. V Madge, D. V Louzguine-Luzgin, A. Kawashima, A. L. Greer, A. Inoue, *Mater. Des.* **101**, 146 (2016).

[5.11] D. Grell, F. Dabrock, E. Kerscher, *Fat. Fract. Eng. Mater. Struct.* **41**, 1330 (2018).

[5.12] A. S. Argon, *Acta Metall.* **27**, 47 (1979).

[5.13] M. L. Falk, J. S. Langer, *Phys. Rev. E.* **57**, 7192 (1998).

[5.14] A. S. Argon, L. T. Shi, *Acta Metall.* **31**, 499 (1983).

[5.15] C. A. Schuh, A. C. Lund, T. G. Nieh, *Acta Mater.* **52**, 5879 (2014).

[5.16] Y. Fan, T. Iwashita, T. Egami, *Nat Commun.* **5**, 5083 (2014).

[5.17] J. D. Ju, D. Jang, A. Nwankpa, M. Atzmon, *J. Appl. Phys.* **109**, 53522 (2011).

[5.18] X. D. Wang , B. Ruta, L. H. Xiong, D. W. Zhang, Y. Chushkin, H. W. Sheng, H. B. Lou, Q. P. Cao, J. Z. Jiang, *Acta Mater.* **99**, 290 (2015).

[5.19] S. W. Provencher, *Comput. Phys. Commun.* **27**, 213 (1982).

[5.20] S. W. Provencher, *Comput. Phys. Commun.* **27**, 229 (1982).

[5.21] R. S. Lakes, Viscoelastic Materials, Cambridge University Press, Cambridge, 2009.

[5.22] H. B. Yu, X. Shen, Z. Wang , L. Gu, W. H. Wang, H. Y. Bai, *Phys Rev Lett.* **108**, 15504 (2012).

[5.23] T. Lei and M. Atzmon, *Unpublished reuslts*.

[5.24] M. Atzmon and J. D. Ju, *Phys. Rev. E* **90**, 042313 (2014).

[5.25] J. D. Ju and M. Atzmon, *MRS Commun.* **4**, 63 (2014).

[5.26] H. S. Chen, *J. Appl. Phys.* **49**, 3289 (1978).

[5.27] W. H. Wang, *Prog. Mater. Sci.* **57**, 487 (2012).

[5.28] A. L. Greer, J. A. Leake, *J. Non-Cryst. Solids* **33**, 291 (1979).

[5.29] P. Das, D. Parmar, S. Sastry, *arXiv preprint arXiv:1805.12476* (2018).

CHAPTER 6

Composition Effect on α and β Relaxations for La-based Metallic Glasses from a Viewpoint of Shear Transformation Zone Properties

6.1 Introduction

The strength of metallic glasses (MGs) is significantly higher than that of polycrystals with comparable composition [1]. However, structural applications of MGs are often limited by their little macroscopic plasticity, resulting from strain localization within dominant shear bands due to shear softening [2]. MG plasticity has been correlated with the secondary (β) relaxation in loss modulus data at high frequency and/or low temperature [3]. For some MGs, the β relaxation manifests as a broad peak/excess wing, which overlaps the main (α) relaxation at low frequency and/or high temperature [4]. Recently, Yu *et al.* [5] reported a La-based MG with a distinct and pronounced β relaxation, which also exhibits relatively large tensile ductility. They argued that the β relaxation is a manifestation of the activation of shear transformation zones (STZs, atomic clusters that have been sheared), implying that the α relaxation corresponds to a different mechanism [6]. While α vs. β relaxation in molecular glasses have been attributed to inter- vs. intramolecular motion, such a distinction cannot be made in MGs, posing a challenge in the identification of the relaxation mechanism.

Chemical composition can significantly affect the intensity of the β relaxation. For example, La-Cu-Al and La-Ni-Al are two alloy systems with similarly wide supercooled liquid region [7,8], but with dramatically different β relaxation behavior – by substituting Ni with Cu atoms, which have similar atomic size, the strong β peak transitions to a shoulder [9]. Yu *et al.* [10] speculated that large similar negative enthalpy of mixing among all constituting atoms results in a pronounced β relaxation, while positive or significantly varying pairwise values of mixing enthalpy suppress the β relaxation, and usually associate with excess wings. However, the microscopic mechanism of the composition effect on relaxation behavior is still not clear.

In a previous work [11], an atomically quantized hierarchy of STZs for an Al-rich MG were resolved, with a volume increment corresponding to the atomic value of Al, the majority element. We later identified the effects of cryogenic cycling and room temperature (RT) ageing on properties of slow and large STZs, corresponding to α relaxation, for $La_{70}Cu_{15}Al_{15}$ and $La_{70}Ni_{15}Al_{15}$ MGs, resolved by STZ size [12]. The present work focuses on the composition effect on both α and β relaxations, by comparing the properties of *both* slow and large *and* fast and small STZs between these two alloys. Similar to a La-based MG studied before [13], two regimes of STZ activation volume are observed – fast and small STZs, corresponding to the β relaxation, more likely include the smaller atoms – Al plus Cu/Ni, while La plus Cu vs. all elements are respectively more likely involved in slow and large STZs associated with the α relaxation for $La_{70}Cu_{15}Al_{15}$ vs. $La_{70}Ni_{15}Al_{15}$ MGs. The pronounced β relaxation, observed in the loss modulus vs. temperature/frequency for $La_{70}Ni_{15}Al_{15}$, but not $La_{70}Cu_{15}Al_{15}$, is a result of two contributions – the former exhibits a larger volume fraction of fast and small *potential* STZs (i.e., atomic clusters capable of shear transformation) and a smaller volume fraction of slow and large *potential* STZs.

6.2 Experimental Details

Amorphous $La_{70}Cu_{15}Al_{15}$ and $La_{70}Ni_{15}Al_{15}$ (at.%) thin ribbons ~ 40 μm thick and 1 mm wide were obtained by single-wheel melt-spinning under the same condition as Ref. 13. The glass transition temperature of which are 391 K and 431 K [9], respectively. The amorphous structure was confirmed by X-ray diffraction. All sample were aged at room temperature (RT) for $3.0 \cdot 10^7$ s before RT anelastic relaxation measurements. The anelastic strain vs. time were obtained from a combination of two measurement techniques – 1) nanoindenter cantilever bending, from ~ 0 s to 200 s, by applying a fixed load of 200 μN and monitoring the corresponding displacement, and 2) stress-free bend relaxation ("mandrel") measurements, from ~ 20 s to $4.2 \cdot 10^7$ s, by monitoring the evolution in radius of curvature of one sample after being constrained around a mandrel for $t_c = 2 \cdot 10^6$ s. The two techniques are detailed in Refs. 11&13. For cantilever bending, three samples were tested, with 20 measurements for each. For mandrel measurements, three and two samples, corresponding to $La_{70}Cu_{15}Al_{15}$ and $La_{70}Ni_{15}Al_{15}$, respectively, were used.

As in Refs. 11,12,13, relaxation-time spectra, $f(\tau)$, were computed from the strain vs. time data, by employing a standard linear solid model and a portable package for inverse problems, CONTIN [14,15], which gives stable and consistent fitting of $\varepsilon_{an}(t)/\varepsilon_{el}^0$. Details on spectrum computation and consistency check are provided in Ref. 11. Spectrum peak properties were determined as the average over all samples of the same composition, and the random error was estimated from standard deviations of the mean.

6.3 Results and Discussion

Figure 6.1 shows the anelastic strain normalized by the equilibrium elastic strain vs. time, obtained from both measurement techniques, for each alloy after prior RT ageing time of $3.0 \cdot 10^7$ s. For cantilever bending, an average curve of all tests is shown for each alloy. Due to the large number of data points (~ 60000) for one measurement cycle, each point in Fig. 6.1a is an average of every 500 data points. For the mandrel measurements (Fig. 6.1b), data corresponding to all samples are presented, showing high reproducibility. At short measurement time (Fig. 6.1a), i.e., from 0.1 to 10 s, the slope for $La_{70}Ni_{15}Al_{15}$ is much larger than for $La_{70}Cu_{15}Al_{15}$. At longer time (Fig. 6.1b), the strain curves are discussed in detail in Ref. 12 for both alloys, also in terms of effects of RT ageing and cryogenic cycling, and briefly reviewed as follow: 1) the strain magnitude is much higher for $La_{70}Cu_{15}Al_{15}$ than for $La_{70}Ni_{15}Al_{15}$, 2) the absolute strain relaxation rate is similar for

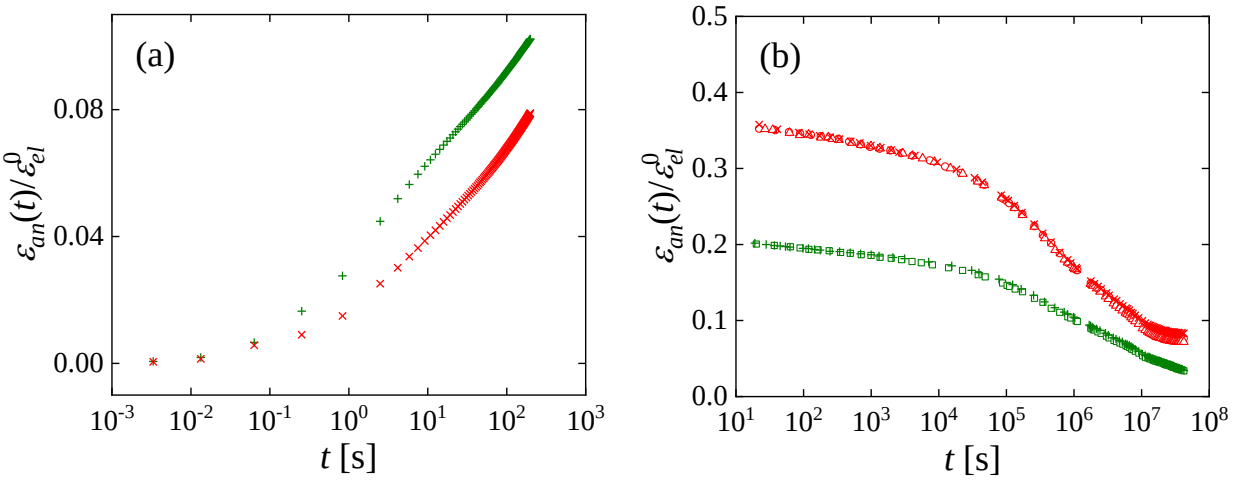

Figure 6.1. Anelastic strain normalized by the corresponding equilibrium elastic strain vs. time for (a) cantilever bending and (b) mandrel measurements of $La_{70}Cu_{15}Al_{15}$ (crosses, circles and triangles) and $La_{70}Ni_{15}Al_{15}$ (pluses and squares) with a RT ageing time of $3.0 \cdot 10^7$ s. For nanoindenter cantilever, each curve is an average of all tests for the same composition, and each point is an average of every 500 experimental data points. For mandrel measurements, curves corresponding to all samples are shown.

both alloys at measurement time up to 10^4 s ~ 10^5 s, while it differs at longer measurement time. This implies that the difference in the strain magnitude is mainly due to the large-time-constant processes, 3) all the measured strain is anelastic, as verified by reversal strain of samples after annealing treatment for 7200 s at 353 K.

Figure 6.2 shows the relaxation-time spectra computed from the strain vs. time data in Fig. 6.1. Similar to Fig. 6.1, for cantilever bending, an average spectrum of all tests is shown for each alloy. It is noted that spectrum shape is the same for all samples and runs. For the mandrel measurements, all spectra are shown. Reference 12 focused on the effect of structural relaxation and cryogenic rejuvenation on large-time-constant spectra for $La_{70}Cu_{15}Al_{15}$ and $La_{70}Ni_{15}Al_{15}$. In the present chapter, we mainly investigate the chemical composition effect on both small- and large-time-constant spectra for these two alloys. Similar to previous studies [11,12,13], all spectra consist of

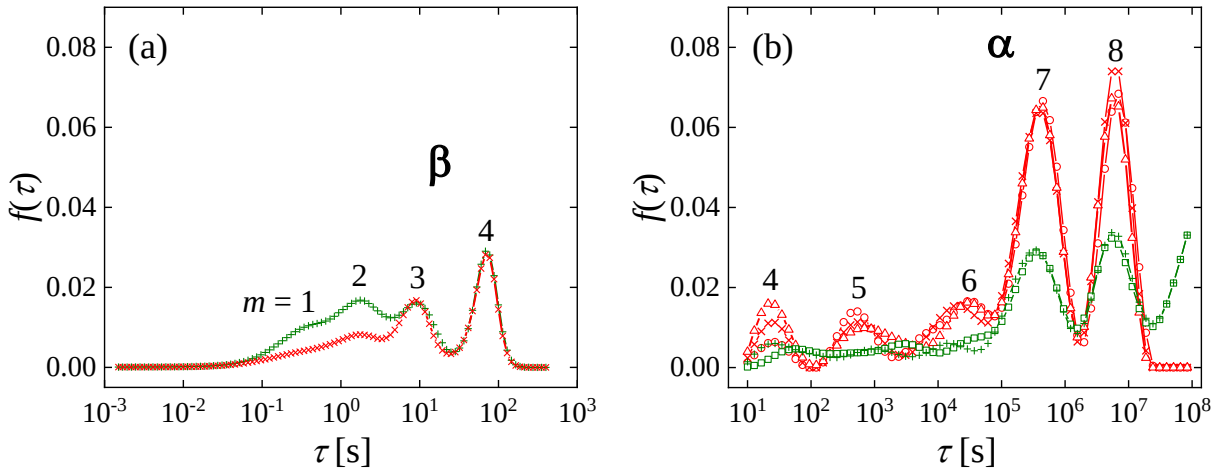

Figure 6.2. Relaxation-time spectra computed from the normalized anelastic strain vs. time data in Fig. 6.1, of $La_{70}Cu_{15}Al_{15}$ (crosses, circles, and triangles) and $La_{70}Ni_{15}Al_{15}$ (pluses and squares) aged at RT for $3.0 \cdot 10^7$ s, for (a) cantilever bending, and (b) mandrel measurements. For cantilever bending, an average of all spectra is shown for each alloy, while all spectra are shown for mandrel measurements. Peaks are number as m=1,…,8, corresponding to different STZ types.

distinct peaks, the number of which is the same. Based on a standard linear solid model [16], these peaks are associated with different STZ types, labeled $m = 1,\ldots,8$. As mentioned in Ref. 13, the last peak from nanoindenter cantilever and the first peak from mandrel measurement should correspond to the same STZ type, $m = 4$. However, their different intensities are possibly because of the inability of the standard linear model to distinguish between fixed-load and stress-free relaxation.

In Fig. 6.2, the peak positions are similar for both alloys, while the peak intensities are different. At small time constants, from ~ 0.1 s to 10 s, corresponding to the β relaxation, the peak intensity is much higher in $La_{70}Ni_{15}Al_{15}$ than in $La_{70}Cu_{15}Al_{15}$. This is consistent with the slope difference in Fig. 6.1a from t ~ 0.1 s to 10 s. At larger time constants, especially for $t > 10^4$ s - 10^5 s, which corresponds to the slower α relaxation, the peak intensity is much higher for $La_{70}Cu_{15}Al_{15}$ than for $La_{70}Ni_{15}Al_{15}$. It has been reported that the La-Ni-Al system shows a pronounced peak in loss modulus at high-frequency and/or low-temperature peak [17,18], while the La-Cu-Al system only exhibits a shoulder within the same range [18]. Therefore, emphasis has been placed on the magnitude of β relaxation in $La_{70}Ni_{15}Al_{15}$ being larger than in $La_{70}Cu_{15}Al_{15}$. The normalization of the loss modulus plots by the intensity of the α peak washed, however, a larger difference in the α intensity. Figure 6.2 clearly shows that a difference in magnitude of both α and β relaxations between the alloys. Consequently, the pronounced β peak in the loss modulus for $La_{70}Ni_{15}Al_{15}$ rather than for $La_{70}Cu_{15}Al_{15}$ is a result of differences in both β and α relaxations.

By employing the standard linear solid model [16] and constitutive laws [19], STZ properties are obtained and compared between $La_{70}Cu_{15}Al_{15}$ and $La_{70}Ni_{15}Al_{15}$. Figure 6.3 shows the relaxation time constants, τ_m, and the corresponding STZ volume, Ω_m. The τ_m value in Fig. 6.3a is determined as the median of each peak m in Fig. 6.2, and similar values are observed for both alloys, indicated by the similar peak position in Fig. 6.2. Then, the Ω_m value is determined from the expression of the time constants [20],

$$\tau_m = \frac{3\eta'_m}{E'_m} = \frac{1}{\Omega_m \gamma_0^T} \cdot \frac{3kT}{2\mu(1+\nu)\gamma_0^c \nu_G} \cdot \exp\left(\mu\Omega_m \left\{\frac{\gamma_0^T}{kT}\left[\left(\frac{(7-5\nu)}{30(1-\nu)} + \frac{2(1+\nu)}{9(1-\nu)}\bar{\beta}^2\right)\gamma_0^T + \frac{1}{2}\frac{\overline{\sigma_{STZ}}}{\mu}\right]\right\}\right). \quad (6.1)$$

η'_m and E'_m are the effective viscosity and effective Young's modulus, respectively, of the m-type STZs. γ_0^T is the unconstrained transformation shear strain, and $\gamma_0^c = [2(4-5\nu)/15(1-\nu)]\gamma_0^T$ is its constrained value. Based on Ref. 11, $\gamma_0^T = 0.2$ is used. $\nu = 0.324$ [21] is Poisson's ratio. $\bar{\beta}^2 \sim 1$ is the dilatancy factor. ν_G is the attempt frequency, k is the Boltzmann constant, and T is the temperature. $\overline{\sigma_{STZ}}$ is the shear resistance of STZs, μ is the shear modulus, and $\overline{\sigma_{STZ}}/\mu = 0.025$ [22].

The shear modulus for each alloy composition is obtained from its Young's modulus, E, by using $\mu = E/[2 \times (1+\nu)]$, and the Young's modulus is assumed from a rule of mixture as [23],

$$M^{-1} = \sum f_i M_i^{-1}, \quad (6.2)$$

where M is the Young's modulus of the alloy, and f_i and M_i are the atomic percentage and Young's modulus of each constituent element, respectively. The E values for La, Al, Ni and Cu are 37 GPa, 70 GPa, 200 GPa, and 130 GPa, respectively [24], which yields the elastic moduli for

$La_{70}Cu_{15}Al_{15}$ and $La_{70}Ni_{15}Al_{15}$ of 45 GPa and 46 GPa, respectively. Young's modulus for $La_{70}Ni_{15}Al_{15}$ is consistent with the value reported in Ref. 21, which validates the use of Eq. (6.2).

Figure 6.3b shows that both alloys exhibit two regimes of STZs, indicated by the two fit lines, similar to $La_{55}Ni_{20}Al_{25}$ MG in Ref. 13. The table insert in Fig. 6.3b lists the slope and intercept of each fit line. The slope for the first regime is smaller than that for the second regime, indicating that smaller atoms are more likely involved in fast and small STZs, while slower and larger STZs more likely comprise larger atoms. It is noted that the slope difference cannot be attributed to the measurement method, as seen in Ref. 11 for an Al-based metallic glass. For $La_{70}Cu_{15}Al_{15}$, the slope for the first regime, $0.151 \cdot 10^{-28}$ m^3, is close to the average atomic volume of Cu ($0.118 \cdot 10^{-28}$ m^3)

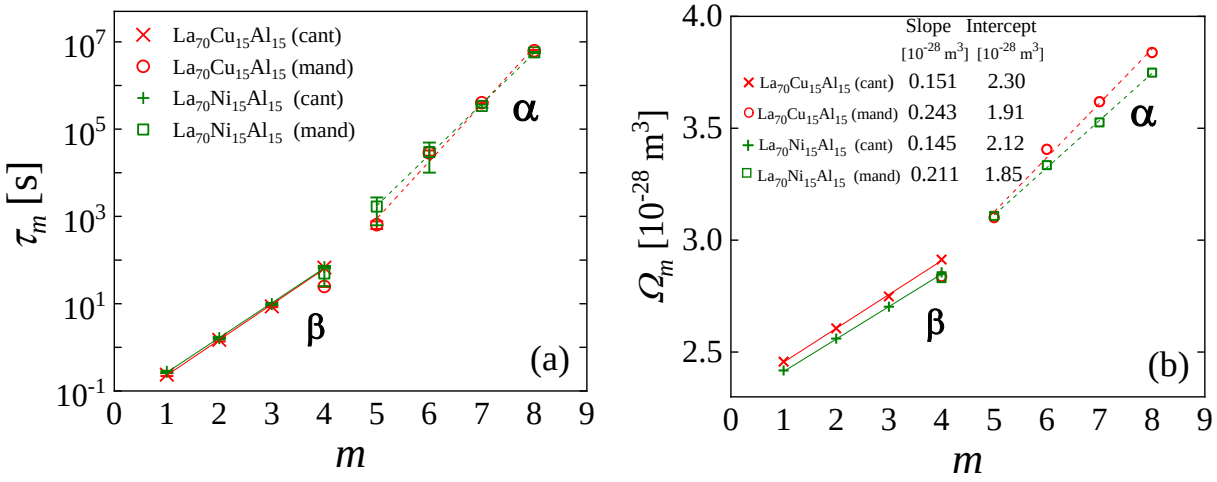

Figure 6.3. (a) Relaxation time constants (τ_m), obtained as median of the spectrum peak, for each STZ type (m) for $La_{70}Cu_{15}Al_{15}$ (crosses and circles) and $La_{70}Ni_{15}Al_{15}$ (pluses and squares) aged at RT for $3.0 \cdot 10^7$ s. (b) STZ volume (Ω_m) for each STZ type (m) for $La_{70}Cu_{15}Al_{15}$ and $La_{70}Ni_{15}Al_{15}$, aged at RT for $3.0 \cdot 10^7$ s. $m = 1,\ldots,4$ (crosses and pluses) correspond to cantilever measurements, while $m = 4,\ldots,8$ (circles and squares) correspond to mandrel measurements.

and Al ($0.166 \cdot 10^{-28}$ m^3), which equals $0.142 \cdot 10^{-28}$ m^3, while the slope of the second regime, $0.243 \cdot 10^{-28}$ m^3, approximately equals the average atomic volume of Cu and La ($0.372 \cdot 10^{-28}$ m^3), $0.245 \cdot 10^{-28}$ m^3. For $La_{70}Ni_{15}Al_{15}$, the slope of the first regime is $0.145 \cdot 10^{-28}$ m^3 and close to the average atomic volume of Ni and Al, $0.138 \cdot 10^{-28}$ m^3, while that of the second regime is $0.211 \cdot 10^{-28}$ m^3 and close to the average atomic volume of the alloy, $0.216 \cdot 10^{-28}$ m^3. Therefore, as in Ref. 13, a possible chemical composition dependence of STZ volume is observed for both alloys.

Yu *et al.* [5] reported that the atomic structure of $La_{68.5}Ni_{15}Al_{14}Co_{1.5}$ MG is composed of two regions, light regions ranging from 50 to 200 nm enveloped by dark boundary regions of about 5 to 20 nm, from scanning transmission electron microscopy images. The dark regions contain excess Ni at the expense of less La, while the distribution of Al atoms is relatively homogeneous. They speculated that this heterogeneous structure may play an important role in the β relaxation. The present result of $La_{70}Ni_{15}Al_{15}$ is consistent with Ref. 5 in terms of 1) the inhomogeneous distribution of La and Ni atoms as the volume increment for small and fast STZs is more likely due to Ni atoms not La atoms, while both Ni and La atoms are more likely involved in larger and slower STZs, and 2) the homogeneous distribution of Al atoms as Al atoms are likely involved in all STZ types. It should be noted that Young's modulus plays an important role in computing STZ volumes (Eq. 6.1), and the value used in the present study is an estimate based on the rule of mixture (Eq. 6.2). It is also noted that MGs exhibit a wide distribution of local elastic properties, e.g., the local indentation modulus M shows $\Delta M/M \approx 30\%$ on a scale below 10 nm [25]. The STZ volume calculated from the data will depend on the assumed modulus. However, the existence of two regimes of the STZ volumes is independent of this uncertainty. In Ref. 13, we observed for a different La-based MG that the time constants for the α relaxation increased with room-

temperature ageing. This increase was attributed to observed increases in the elastic constants. However, the time constants for the faster relaxations did not change with ageing. This behavior may be due to spatial heterogeneity in the evolution of elastic constants with ageing.

Figure 6.4 shows the volume fraction of *potential* STZs (c_m) as a function of the activation free energy (ΔF) for shear transformation divided by kT, for $La_{70}Cu_{15}Al_{15}$ and $La_{70}Ni_{15}Al_{15}$. The activation energy [26],

$$\Delta F_m = \left[\left(\frac{(7-5\nu)}{30(1-\nu)} + \frac{2(1+\nu)}{9(1-\nu)}\bar{\beta}^2\right)\gamma_0^T + \frac{1}{2}\frac{\overline{\sigma_{STZ}}}{\mu}\right]\mu\gamma_0^T\Omega_m, \tag{6.3}$$

is a function of both STZ volume and shear modulus. As mentioned in Ref. 11,12,13, the c_8 values

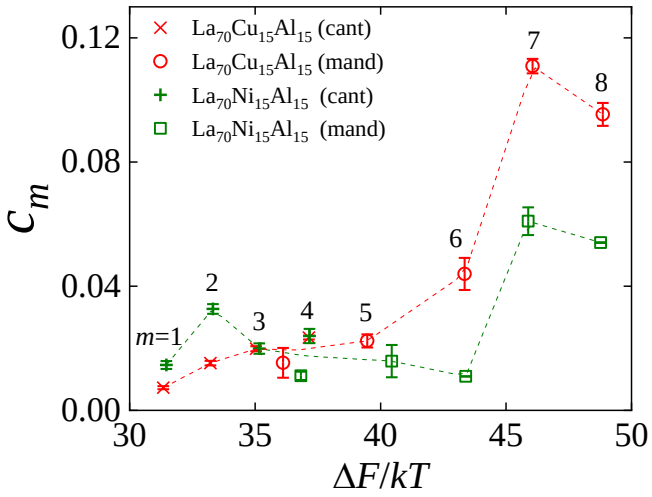

Figure 6.4. Volume fraction of *potential* STZs for $La_{70}Cu_{15}Al_{15}$ (crosses and circles) and $La_{70}Ni_{15}Al_{15}$ (pluses and squares) with a RT ageing time of $3.0\cdot10^7$ s as a function of activation free energy for shear transformation divided by kT. The error bars for ΔF/kT are smaller than the symbol. For m=4, the cantilever bending and mandrel measurements yield slightly different values of c_m and ΔF/kT, which may be due to the limitation of the standard linear solid model used for the analysis.

for both $La_{70}Cu_{15}Al_{15}$ and $La_{70}Ni_{15}Al_{15}$ are underestimated due to the fact that m = 8 STZs did not reach mechanical equilibrium at the end of constraining period ($\tau_8 > t_c$). Since the present study focuses on the composition effect, and the underestimation should be similar for both alloys because of their similar τ_8 values, the underestimation will not be further considered here.

For $La_{70}Cu_{15}Al_{15}$, c_m increases with increasing m and corresponding activation energy. However, for $La_{70}Ni_{15}Al_{15}$, an obvious peak occurs at small ΔF values, similar to that for $La_{55}Ni_{20}Al_{25}$ in Ref. 13. When comparing the two present alloys, noticeable differences in c_m are observed for $\Delta F/\mathrm{k}T < 35$ and $\Delta F/\mathrm{k}T > 40$, which correspond to the β and α relaxations, respectively. The c_m values are larger for $La_{70}Ni_{15}Al_{15}$ than for $La_{70}Cu_{15}Al_{15}$ at lower activation energy, while the reverse holds at higher activation energy. This indicates that $La_{70}Ni_{15}Al_{15}$ possesses larger volume fraction of fast and small *potential* STZs (PSTZs), while the volume fraction of slow and large PSTZs is larger in $La_{70}Cu_{15}Al_{15}$. In Ref. 5, the authors proposed that MGs with pronounced β relaxation may possess abundant PSTZs. Since a quantized hierarchy of STZs is obtained for MGs with and without strong β relaxation in the present study, further details can be added to the previous proposition – MGs with pronounced β relaxation have *more* small and fast PSTZs and *fewer* large and slow PSTZs than MGs without a strong β peak. The time constants of the small vs. large PSTZs are < 100 s vs. > 10^4 s - 10^5 s, respectively. The volume increments corresponding to the small vs. large PSTZs are likely due to Cu and Al vs. Cu and La for $La_{70}Cu_{15}Al_{15}$, and Ni and Al vs. all constituent atoms for $La_{70}Ni_{15}Al_{15}$, respectively. Reference [5] reported, in addition, a correlation between pronounced β peak and large macroscopic plasticity, as La-based MGs exhibit a stronger β relaxation and greater ductility than other MGs. However, this correlation is not universal. In the present study, RT tensile tests at strain rate of 10^{-5} s^{-1} and 10^{-6} s^{-1} for both

alloys revealed an opposite trend, showing much larger plasticity for $La_{70}Cu_{15}Al_{15}$ than for $La_{70}Ni_{15}Al_{15}$. These observations suggest that dynamic mechanical analysis may not always be a useful screening tool in the development of MGs with large plasticity.

6.4 Conclusions

The present study provides a detailed description of the composition effect on both α and β relaxations by comparing STZ properties of $La_{70}Cu_{15}Al_{15}$ and $La_{70}Ni_{15}Al_{15}$ from anelastic relaxation from less than one second to more than one year. Similar to $La_{55}Ni_{20}Al_{25}$ MG in our previous study, both alloys show two regimes of STZ volumes – the volume increment for STZs corresponding to β relaxation is smaller than that corresponding to α relaxation. The pronounced β relaxation in normalized dynamic-mechanical measurements, observed in $La_{70}Ni_{15}Al_{15}$ but not in $La_{70}Cu_{15}Al_{15}$, is due to both the larger volume fraction of fast and small *potential* STZs, corresponding to β relaxation, and the smaller volume fraction of slow and large *potential* STZs, corresponding to α relaxation in $La_{70}Ni_{15}Al_{15}$ than in $La_{70}Cu_{15}Al_{15}$. The tensile result that $La_{70}Cu_{15}Al_{15}$ shows a much higher plasticity than $La_{70}Ni_{15}Al_{15}$ implies there is no clear correlation between the intensity of the β relaxation and macroscopic plasticity.

6.5 References

[6.1] C. A. Schuh, T. C. Hufnagel, and U. Ramamurty, *Acta Mater.* **55**, 4067 (2007).

[6.2] A. L. Greer and E. Ma, *MRS Bull.* **32**, 611 (2007).

[6.3] H. B. Yu, W. H. Wang, and K. Samwer, *Mater. Today* **16**, 183 (2013).

[6.4] J. Qiao, J. -M. Pelletier, and R. Casalini, *J. Phys. Chem. B* **117**, 13658 (2013).

[6.5] H. B. Yu, X. Shen, Z. Wang, L. Gu, W. H. Wang, and H. Y. Bai, *Phys. Rev. Lett.* **108**, 015504 (2012).

[6.6] H. B. Yu, W. H. Wang, H. Y. Bai, Y. Wu, and M. W. Chen, *Phys. Rev. B* **81**, 220201 (2010).

[6.7] A. Inoue, H. Yamaguchi, T. Zhang, and T. Masumoto, *Mater. Trans. JIM* **31**, 104 (1990).

[6.8] A. Inoue, T. Zhang, and T. Masumoto, *Mater. Trans. JIM* **30**, 965 (1989).

[6.9] X. D. Wang, B. Ruta, L. H. Xiong, D. W. Zhang, Y. Chushkin, H. W. Sheng, H. B. Lou, Q. P. Cao and J. Z. Jiang, *Acta Mater.* **99**, 290 (2015).

[6.10] H. B. Yu, K. Samwer, H. W. Wang, and H. Y. Bai, *Nat. Commun.* **4**, 2204 (2013).

[6.11] J. D. Ju,, D. Jang, A. Nwankpa, and M. Atzmon, *J. Appl. Phys.* **109**, 053522 (2011).

[6.12] T. J. Lei, L. Rangel DaCosta, M. Liu, W. H. Wang, Y. H. Sum, A. L. Greer, and M. Atzmon, *Acta Mater.* **164**, 165 (2019).

[6.13] T. J. Lei, L. Rangel DaCosta, M. Liu, W. H. Wang, Y. H. Sun, A. L. Greer, and M. Atzmon, *Phys. Rev. E* **100**, 033001 (2019).

[6.14] S. W. Provencher, *Comput. Phys. Commun.* **27**, 213 (1982).

[6.15] S. W. Provencher, *Comput. Phys. Commun.* **27**, 229 (1982).

[6.16] A. S. Nowick and B. S. Berry, Anelastic relaxation in crystalline solids, Academic Press, New York and London, 1972.

[6.17] H. Okumura, H. S. Chen, A. Inoue, and T. Masumoto, *J. Non-Cryst. Solids* **130**, 304 (1991).

[6.18] Z. Wang, H. B. Yu, P. Wen, H. Y. Bai, and W. H. Wang, *J. Phys.: Condens. Matter* **23** 142202 (2011).

[6.19] A. S. Argon, *Acta Metall.* **27**, 47 (1979).

[6.20] J. D. Ju and M. Atzmon, *MRS Commun.* **4**, 63 (2014).

[6.21] S. T. Liu, Z. Wang, H. L. Peng, H. B. Yu, and W. H. Wang, *Scr. Mater.* **67**, 9 (2012).

[6.22] H. Kato, H. Igarashi, and A. Inoue, *Mater. Lett.* **62**, 1592 (2008).

[6.23] Z. Zhang, R. J. Wang, L. Xia, B. C. Wei, D. Q. Zhao, M. X. Pan, and W. H. Wang, *J. Phys.: Condens. Matter* **15**, 4503 (2003).

[6.24] W. H. Wang, *Prog. Mater. Sci.* **57**, 487 (2012).

[6.25] H. Wagner, D. Bedorf, S. Küchemann, M. Schwabe, B. Zhang, W. Arnold, and K. Samwer, *Nat. Mater.* **10**, 439 (2011).

[6.26] A. S. Argon and L. T. Shi, *Acta Metall.* **31**, 499-507 (1983).

CHAPTER 7

Activation Volume Details from Nonlinear Anelastic Deformation of a Metallic Glass

Reprinted from T. J. Lei and M. Atzmon, "Activation volume details from nonlinear anelastic deformation of a metallic glass," J. Appl. Phys. 126, 185104 (2019), with permission of AIP Publishing. DOI: https://doi.org/ 10.1063/1.5122973.

7.1 Introduction

Metallic glasses (MGs) have drawn considerable attention due to their high strength and elastic limit [1]. However, they experience flow localization resulting in little macroscopic plasticity [2], which limits their structural application. Understanding the deformation mechanism of MGs is necessary to identify ways to improve their plasticity. Unlike for crystalline alloys, knowledge of the microscopic origin of plastic deformation of MGs is incomplete due to their disordered structure. Physical analogs [3,4] have shown that macroscopic deformation is accommodated by cooperative shearing of atomic clusters, termed shear transformation zones (STZs) [5,6,7,8].

Plastic deformation of metallic glasses involves a large volume fraction of STZs in an activated flow state, for which STZ interactions are complex. In contrast, at small strain, the STZ volume fraction is small, in the dilute limit, so they are isolated. They can be reversed upon removal of

external stress due to back stress in the elastic matrix, which leads to anelastic behavior [9]. In crystalline metals, several mechanisms of anelastic relaxation have been studied. We consider the STZ mechanism to dominate anelasticity in metallic glasses, based on the following points: a) The Snoek effect of small interstitial solutes [10] is unlikely in a metallic glass in the absence of, e.g., hydrogen or carbon atoms. b) Chemical order-disorder effects [11], if any, are weak in amorphous metals. c) Any local jumps of constituent atoms are likely to be STZ mediated. d) The present experiments involve a single phase and isothermal conditions [11].

Anelastic deformation in the small-strain regime offers an opportunity to understand plasticity. Ju *et al.* [12] performed quasi-static anelastic relaxation measurements of $Al_{86.8}Ni_{3.7}Y_{9.5}$ (at.%) over a time range spanning seven orders of magnitude. The corresponding relaxation-time spectra were computed, which exhibited distinct peaks, representing an atomically quantized hierarchy of STZs, consisting of 14 to 21 atoms for the kinetic window observed. The measurements involved small anelastic strain and correspondingly small STZ volume fraction, 1-2% [12,13]. Linear dependence of the equilibrated anelastic strain under constraint on the applied stress was observed, which also implied a linear anelastic strain profile across the sample thickness. Consequently, there was no residual stress upon constraint removal.

In the present work, anelastic relaxation is studied at higher strain than in our prior work, such that the viscosity under constraint is non-Newtonian, but STZ volume fractions are still small, $\leq 7.2\%$. Unlike in the linear regime, this approach allows for an independent determination of the STZ volume and transformation strain for the largest activated STZs.

7.2 Background

Ju *et al.* [12] obtained time-constant spectra for anelastic relaxation for amorphous $Al_{86.8}Ni_{3.7}Y_{9.5}$, which exhibited a set of distinct peaks. They modeled the behavior with a standard linear solid model (Fig. 7.1) – a spring in series with several Voigt units, each of which represents one peak and STZ size, and contributes additively to the total strain. Analysis of the data, assuming a transformation shear strain of 0.2 [3,4], revealed that each peak corresponded to an STZ size that comprises a discrete number of Al atoms. A size increment of one atom corresponds to about an order of magnitude larger time constants. Under constraint for 2×10^6 s at a fixed strain, all but the largest and slowest active STZs, those comprising n = 21 atoms, essentially reach mechanical equilibrium with each other and the elastic matrix, then track the slow evolution of the n = 21 STZs. (For longer constraining time, n = 22 STZs were also activated [13].) After constraint removal, each STZ size evolves independently in this model.

In Ref. [12], the shear strain rate due to STZs indexed with the integer m under an applied shear stress, σ, was expressed as [3]

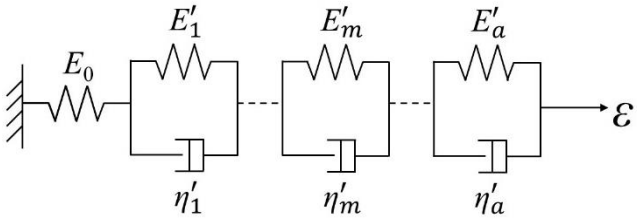

Figure 7.1. Schematic illustration of the standard linear solid model employed – a spring with Young's modulus E_0 in series with Voigt units, each of which represents one STZ size. E_m' and η_m' are the effective Young's modulus and effective viscosity, respectively, of m-type STZs, where m = 1-8 for the range of time values in the experiment [12]. Reproduced with permission from Ju *et al.*, J. Appl. Phys. 109, 053522 (2011). Copyright 2011 AIP Publishing LLC.

$$\dot{\gamma}_m = 2c_m\gamma_o^c\nu_G\exp\left(-\frac{\Delta F_m}{kT}\right)\sinh\left(\frac{\sigma\gamma_o^T\Omega_m}{2kT}\right), \quad (7.1)$$

m=1,…,8. c_m is the volume fraction occupied by *potential m*-type STZs, where a *potential* STZ is an atomic cluster that is capable of shear transformation. γ_o^T is the transformation shear strain, and $\gamma_o^c = \left[2(4-5\nu)/\left(15(1-\nu)\right)\right] \times \gamma_o^T$ is its value under constraint by the surrounding matrix with ν being Poisson's ratio. ν_G is the attempt frequency. Ω_m is the volume of *m*-type STZs. The product $\gamma_o^T \times \Omega_m$ is the activation volume for a shear transformation, i.e., the conjugate of the stress. *k, T* have the usual meaning. For small σ values, the hyperbolic sine term can be linearized, so that the strain rate is proportional to σ. ΔF_m is the activation free energy for shear transformation of *m*-type STZs [14]:

$$\Delta F_m = \left[\left(\frac{7-5\nu}{30(1-\nu)} + \frac{2(1+\nu)}{9(1-\nu)}\bar{\beta}^2\right) \times \gamma_o^T + \frac{1}{2} \times \frac{\overline{\sigma_{STZ}}}{\mu}\right]\mu\gamma_o^T\Omega_m. \quad (7.2)$$

$\bar{\beta}^2$ is the dilatancy factor and approximately equal to 1, μ is the shear modulus and expressed as $E_0/[2(1+\nu)]$, and E_0 is Young's modulus. $\overline{\sigma_{STZ}}$ is the shear resistance of an STZ if it were not embedded in the matrix. The three terms in Eq. (7.2) correspond, respectively, to the a) shear strain energy; b) dilatation strain energy and c) shear energy of the STZ if it were not embedded in the matrix [15]. The parameters in Eqs. (7.1)&(7.2), their values and sources are summarized in Table 7.1 and the appendix.

In the linear, i.e., Newtonian regime, the product $(\gamma_0^T)^2 \times \Omega_m$ can be determined, but not each factor independently. An estimated value of $\gamma_0^T = 0.2$, based on physical analogs [3,4], was used to obtain Ω_m, *m* = 1,…,8 in Refs. [12,13]. These values were spaced by a single atomic volume. Each Ω_m value is associated with an integer multiple of the atomic value of Al: $\Omega_n = n \times \Omega_{Al}$,

Table 7.1. Parameter definitions in the expression of shear strain rate (Eq. 7.1) and activation free energy (Eq. 7.2)

Symbol	Physical meaning	Value/Expression
c_m	Volume fraction occupied by *potential m*-type STZs	Area of corresponding spectrum peak from experiments, Refs. [12,13]
m	Index of spectrum peaks	1,…,8 * Note: $n = 13 + m$ = number of atoms in STZ is used as a subscript in Eq. (7.9) and below it
γ_o^c	Transformation shear strain under constraint by surrounding matrix	$\gamma_o^c = \left[2(4-5\nu)/\left(15(1-\nu)\right)\right] \times \gamma_o^T$
ν_G	Attempt frequency	10^{13} s^{-1} (Ref. [16])
T	Temperature	295.15 K
ΔF_m	Activation barrier associated with *m*-type STZs	Eq. (7.2)
σ	Applied shear stress	Expressed in Eq. (7.8)&(7.16)
Ω_m	Volume of *m*-type STZs	To be determined
$\bar{\beta}^2$	Dilatancy factor	~1 (Ref. [14])
$\overline{\sigma_{STZ}}$	Peak interatomic shear stress between atoms in a regular lattice	$\overline{\sigma_{STZ}}/\mu$ = 0.025 [17]
ν	Poisson's ratio	0.35 (Ref. [18])
E_0	Young's modulus of the matrix	48.2 GPa [19]
μ	Shear modulus of the matrix	$E_0/[2(1+\nu)]$
γ_o^T	Transformation shear strain in the absence of constraint by the surrounding matrix	To be determined

where $n = 13 + m$. The range of n values, $14 \leq n \leq 21$, is determined by the range of experimental time scales. In order to determine γ_0^T and $\Omega_{n=21}$ independently, it is necessary to perform measurements at higher stress, in the non-Newtonian regime, where Eq. (7.1) is not linear in σ. Such an approach was reported for large tensile strains, up to 0.08, using strain-rate jumps and assuming a single STZ size [14]. The present work involves anelasticity measurements in the non-Newtonian regime, but in contrast to Ref. [14], we employ a maximum bending strain of 0.0155, with maximum anelastic shear strain of 0.0060, such that the volume fraction occupied by STZs is still small, ≤ 7.2 %. Therefore, STZ properties are obtained for an inherent state, i.e., a local minimum of the energy landscape. While uniaxial geometry offers zero residual stress and far simpler analysis, experiments in bending geometry, not being instrumented, allow for high precision in a wide dynamic range of time, ~ 10^2 s - 3.0×10^7 s for the present work. Using the constitutive law (Eq. 7.1) for n = 21 STZs and zero-bending-moment condition after constraint removal and complete reversal of STZs with n < 21, strain data for $Al_{86.8}Ni_{3.7}Y_{9.5}$ are analyzed, accounting for residual stresses. The volume of the largest and slowest active STZ size, for a constraining period of 2×10^6 s, $\Omega_{n=21}$, and the transformation shear strain are obtained independently.

7.3 Experimental Details

Amorphous $Al_{86.8}Ni_{3.7}Y_{9.5}$ (at.%) ribbons, 22 μm thick and 1 mm wide, were produced by single-wheel melt-spinning using a Cr-coated Cu wheel at a tangential velocity of 40 m/s in vacuum. In previous bend relaxation measurements [12], samples were constrained by wrapping around mandrels with radii ranging from 0.35 to 0.49 cm, corresponding to equilibrium elastic bending strain values from 0.00158 to 0.00303 at the surface. To obtain higher bending strain, up to 0.0155,

a constraining method was developed for smaller radii, as illustrated in Fig. 7.2a: a sample is placed between a mandrel (radius 0.09 or 0.11 cm) and neoprene block. A machined device is used to press the mandrel until the two ends of the sample just touch each other, so that a well-characterized geometry is obtained. A peephole on the side surface of the machined device is used to observe the two touching ends of the sample during constraining (Fig. 7.2b). Because of the low modulus of the neoprene, the pressure on the sample is negligible compared to the bending stress. A lubricant was applied between the sample and neoprene to minimize friction. In contrast to the constraining configuration in Ref. [12], in which the entire sample was under constraint, in the present work, only a small section is under constraint, with the two free ends allowing for a reliable determination of the radius of curvature. The detailed constraining geometry is shown in Fig. 7.3a. 1 cm long samples were used, and all measurements were performed at room temperature.

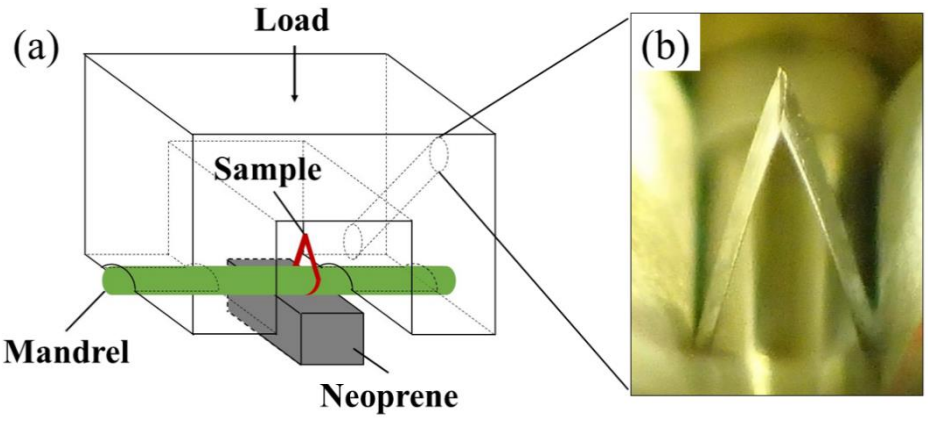

Figure 7.2. (a) Schematic illustration of the constraining method – the sample is placed between a mandrel and neoprene block, and a machined device is used to press the mandrel until two stress-free ends of the sample just touching each other. (b) Photograph showing the two touching ends of a sample under constraint.

As in Ref. [12], samples were constrained for t_c^{total} = 2·10^6 s, then relaxed stress-free for up to 3·10^7 s. The evolution in the angle between the two ends during stress-free relaxation (Fig. 7.3b) was recorded with a digital camera, and used to determine the curvature of the previously bent section. A stage micrometer was used for calibration, and the optical axis of the camera was aligned perpendicular to the sample stage.

The total constraining strain at a distance *y* from the sample midplane is

$$\varepsilon_{constr}(y) = y \cdot (1/R - 1/r_0), \tag{7.3}$$

where R is mandrel radius, and r_0 is the initial radius of curvature for the sample before constraining. At the end of the constraining period, lasting t_c^{total}, $\varepsilon_{constr}(y)$ includes both an elastic and an anelastic component. We can determine apparent strain values, based on linear variation with *y*. The apparent elastic strain is

$$\varepsilon_{el,constr}^{app}(y, t_c^{total}) = y \cdot [1/R - 1/r(0)], \tag{7.4}$$

where $r(t)$ is the radius of curvature of the previously constrained section at time t after constraint removal. The apparent anelastic strain is

$$\varepsilon_{an,constr}^{app}(y, t_c^{total}) = y \cdot [1/r(0) - 1/r_0]. \tag{7.5}$$

Note that unlike the elastic strain, the apparent anelastic strain at the end of the constraining period is equal to its value at *t* = 0 after constraint removal, $\varepsilon_{an}^{app}(y, t = 0)$.

Substitution of $r(t)$ for $r(0)$ in Eq. (7.5) provides the apparent anelastic strain at time t after constraint removal. In the case of Newtonian behavior, when the strain profile across the sample thickness is linear, the expressions for the apparent strains are equal to the actual values. However, in the nonlinear regime, the anelastic strain is superlinear close to the surface. As a result, there is residual stress near each surface in the unconstrained state, with signs opposite of those under constraint. $\varepsilon_{an}^{app}(d/2, t)$, d being the sample thickness, is then lower than the actual anelastic strain at the surface.

While it would be challenging to directly measure the radius of curvature of the small constrained section during unconstrained relaxation, the well-characterized geometry (Fig. 7.3) allows for a reliable determination of $r(t)$ from the angle between two fit lines to the free ends (dashed lines in

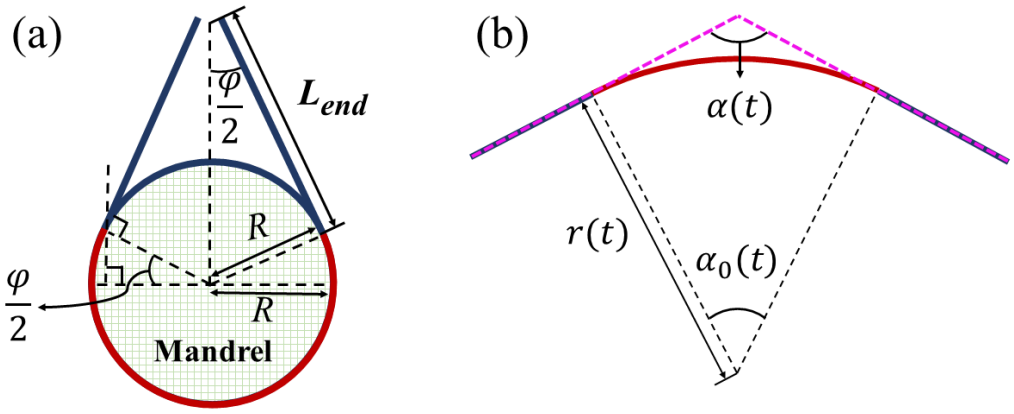

Figure 7.3. Sample geometry (a) under constraint, (b) during unconstrained relaxation (not to scale). $\alpha(t)$ is used to determine the evolution of the curvature of the previously bent section during unconstrained relaxation. The length of the constrained section (red) is equal to $(\pi + \varphi) \times (R + d/2)$, where R is the mandrel radius, and d is the sample thickness. Dashed lines are fits to the unconstrained ends. The small curvature of the free ends is neglected in these plots.

Fig. 7.3b). For different mandrel radii used, the maximum constraining strain ranges from 0.0079 to 0.0155, below the yield point (~ 0.02) [20]. This was verified by the observation that constraining for a short duration did not lead to permanent deformation. The estimated volume fraction occupied by STZs, based on the anelastic strain, is between 3% and 7%, still in the dilute limit.

It was shown in Ref. [12] that the time constant for anelastic recovery of the largest active STZs (consisting of 21 Al atoms) is $\tau_{21} = 1.25\times10^7$ s, significantly longer than the total constraining time (t_c^{total}=2×10^6 s). All other τ_i, $i \leq 20$, are smaller than 10^6 s [12]. It follows that all but the $n = 21$ STZs nearly equilibrate by the end of the constraining period. Since nonlinearity affects the kinetics but not the mechanical equilibrium state, it therefore only affects the contribution of n=21 STZs, as these do not equilibrate during the constraining time. In order to isolate this contribution, the apparent anelastic strain after $t = 4\times10^6$ s unconstrained relaxation is shown in Fig. 7.4 as a function of the apparent elastic strain at the end of the constraining period, both computed for the sample surface. The contribution of STZs with $n \leq 20$ atoms to the anelastic strain is negligible at this point ($t = 4\times10^6$ s), since these have essentially been fully reversed. The five small-strain data points in Fig. 7.4, which lie on a straight line, are taken from Ref. [12]. Significant deviation from linearity is observed at high strain and stress. The decrease of the anelastic strain due to $n = 21$ STZs from its value at the end of the constraining period, about 27% during unconstrained relaxation for $4\cdot10^6$ s, is accounted for in the analysis.

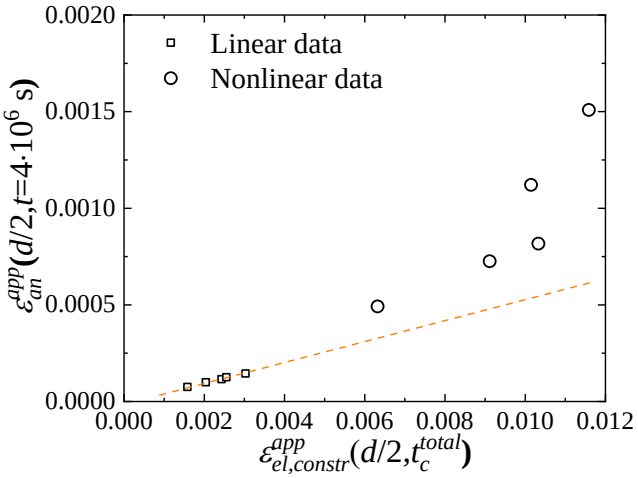

Figure 7.4. Apparent anelastic strain after unconstrained relaxation for $t = 4\times10^6$ s as a function of the apparent elastic strain at the end of the constraining period for varying constraining radii. Both are computed for the sample surface. Each symbol represents one sample. Deviation from linearity occurs at high strain. The dashed line is a fit to the linear portion.

7.4 Overview of the Data Analysis

"Apparent" strain values below are those determined from curvature by using linear variation across the sample. The term "actual" is used to distinguish strain and stress values from their apparent values. The appendix contains a summary of the notation used below.

1. Applying the condition of zero total bending moment after constraint removal, a relationship between the apparent anelastic strain at the sample surface at $t = 4 \times 10^6$ s after constraint removal, $\varepsilon_{an}^{app}(d/2, t = 4 \times 10^6\ \mathrm{s})$, and the position-dependent anelastic strain due to $n = 21$ STZs at the end of the constraining period, $\varepsilon_{21,constr}(y, t_c^{total})$, is obtained.

2. $\varepsilon_{an}^{app}(d/2, t = 4 \times 10^6 \text{ s})$ is directly determined from curvature measurements (Eq. 7.5). An expression for $\varepsilon_{21,constr}(y, t_c^{total})$, in terms of the apparent elastic strain at the sample surface at the end of the constraining period, $\varepsilon_{el,constr}^{app}(d/2, t_c^{total})$, is obtained from time integration of the position- and time-dependent macroscopic shear strain rate due to n = 21 STZs under constraint, $\dot{\gamma}_{21,constr}(y, t_c)$. Approximations used in this step are detailed below.

3. Substituting the expression for $\varepsilon_{21,constr}(y, t_c^{total})$ into the relationship between $\varepsilon_{an}^{app}(d/2, t = 4 \times 10^6 \text{ s})$ and $\varepsilon_{21,constr}(y, t_c^{total})$, obtained in step 1 above, yields a fitting equation for $\varepsilon_{an}^{app}(d/2, t = 4 \times 10^6 \text{ s})$ vs. $\varepsilon_{el,constr}^{app}(d/2, t_c^{total})$. This equation contains two fitting parameters: the transformation shear strain, γ_0^T, and the volume of n = 21 STZs, Ω_{21}.

4. A simultaneous two-parameter fit is performed on all data. The linear portion, which has smaller error, is not fitted as well as with a separate linear fit. A revised two-step fit is performed as follows: first, the linear regime is fitted, which yields the value of $(\gamma_0^T)^2 \times \Omega_{21}$ with small random error. This value is then used as a constraint for the entire data set to obtain Ω_{21} and γ_0^T.

7.5 Analysis Details

We first note that for the presently used bending-strain values ≤ 0.0155, nonlinear *elastic* behavior [21] is likely to be minimal, especially since the long-range elastic field of an STZ dominates ΔF in Eq. (7.2). Since nonlinearity is observed in Fig. 7.4, nonlinear kinetics (Eq. 7.1) now will be used. After constraint removal, the total bending moment is zero:

$$M(t=0) = \int_{-\frac{d}{2}}^{\frac{d}{2}} [\sigma_{constr}(y, t_c^{total}) - \sigma_u(y, t=0)] \times y dy = 0, \quad (7.6)$$

where $\sigma_{constr}(y, t_c^{total})$ is the applied stress at a distance y from the sample midplane at the end of the constraining period. $\sigma_u(y, t=0)$ is the unloading stress immediately upon constraint removal, which varies linearly across the sample thickness:

$$\sigma_u(y, t=0) = y \times \left[\frac{1}{R} - \frac{1}{r(0)}\right] \cdot \frac{E_0}{2(1-\nu^2)}. \quad (7.7)$$

The position-dependent applied stress at the end of the constraining period is:

$$\sigma_{constr}(y, t_c^{total}) = \left[\varepsilon_{constr}(y) - \varepsilon_{an,constr}(y, t_c^{total})\right] \times \frac{E_0}{2(1-\nu^2)}, \quad (7.8)$$

where $\varepsilon_{constr}(y)$ is the position-dependent total constraining strain, $y \times [1/R - 1/r_0]$. $\varepsilon_{an,constr}(y, t_c^{total})$ is the sum of the position-dependent anelastic strain due to all active STZ sizes at the end of the constraining period. It consists of contributions: a) due to STZs comprising *n* atoms, $\varepsilon^0_{n,constr}(y, t_c^{total})$, *n* = 14-20, which reached mechanical equilibrium during constraining, and b) due to *n* = 21 STZs, $\varepsilon_{21,constr}(y, t_c^{total})$ – these did not reach mechanical equilibrium. Therefore, $\varepsilon_{an,constr}(y, t_c^{total})$ is expressed as:

$$\varepsilon_{an,constr}(y, t_c^{total}) = \sum_{n=14}^{20} \varepsilon^0_{n,constr}(y, t_c^{total}) + \varepsilon_{21,constr}(y, t_c^{total}) =$$

$$= \sum_{n=14}^{20} c_n \times \varepsilon_{el,constr}(y, t_c^{total}) + \varepsilon_{21,constr}(y, t_c^{total}). \quad (7.9)$$

$\varepsilon^0_{n,constr}(y, t_c^{total})$ equals $c_n \times \varepsilon_{el,constr}(y, t_c^{total})$ [12], where c_n is the volume fraction occupied by *potential* STZs comprising *n* atoms, and $\varepsilon_{el,constr}(y, t_c^{total})$ is the position-dependent elastic strain at the end of the constraining period. The values of c_n were obtained in Refs. [12,13].

Substituting Eqs. (7.7)-(7.9) into Eq. (7.6), and since $\sigma_{constr}\left(y, t_c^{total}\right)$ and $\sigma_u(y, t = 0)$ are antisymmetric, Eq. (7.6) immediately after constraint removal becomes:

$$\int_0^{\frac{d}{2}} y \times \left[\frac{1}{r(0)} - \frac{1}{r_0}\right] \times y dy = \int_0^{\frac{d}{2}} \sum_{n=14}^{20} c_n \times \varepsilon_{el,constr}(y, t_c^{total}) \times y dy + \int_0^{\frac{d}{2}} \varepsilon_{21,constr}(y, t_c^{total}) \times y dy. \quad (7.10)$$

After $t = 4 \cdot 10^6$ s of stress-free relaxation, the contribution of STZs with $14 \leq n \leq 20$ vanishes, and with $\tau_{21} = 1.25 \times 10^7$ s [12], the anelastic strain due to $n = 21$ decreases by a factor of 0.73. Consequently, at $t = 4 \times 10^6$ s, the zero-moment condition becomes:

$$\varepsilon_{an}^{app}(d/2, t = 4 \times 10^6 \text{ s}) = 0.73 \times \frac{12}{d^2} \times \int_0^{\frac{d}{2}} \varepsilon_{21,constr}(y, t_c^{total}) \times y dy. \quad (7.11)$$

The position-dependent anelastic bending strain due to $n = 21$ STZs at the end of the constraining period is:

$$\varepsilon_{21,constr}(y, t_c^{total}) = (1 - \nu) \times \int_0^{t_c^{total}} \dot{\gamma}_{21,constr}(y, t_c)\, dt_c, \quad (7.12)$$

where $(1 - \nu)$ is the ratio of bending to shear strain. $\dot{\gamma}_{21,constr}(y, t_c)$ is the actual position-dependent macroscopic shear strain rate due to $n = 21$ STZs after time t_c under constraint. Similar to the total anelastic strain, $\varepsilon_{21,constr}\left(y, t_c^{total}\right)$ is also equal to the anelastic strain due to $n = 21$ STZs immediately following constraint removal, $\varepsilon_{21}(y, t = 0)$. Using Eq. (7.1) with $n = 21$ corresponding to $m = 8$, the actual position-dependent macroscopic shear strain rate due to $n = 21$ STZs as function of time under constraint is,

$$\dot{\gamma}_{21,constr}(y, t_c) = 2c_{21}\gamma_0^c \nu_G \exp\left[-\frac{\Delta F_{21}}{kT}\right] \sinh\left[\frac{\sigma_{constr}(y,t_c)\gamma_0^T \Omega_{21}}{2kT}\right]. \quad (7.13)$$

The last term in Eq. (7.2), the shear resistance of an STZ isolated from the matrix, can be neglected [14], yielding

$$\Delta F_{21} = \left[\frac{(7-5\nu)}{30(1-\nu)} + \frac{2(1+\nu)}{9(1-\nu)} \times \bar{\beta}^2\right] \mu (\gamma_0^T)^2 \Omega_{21}. \quad (7.14)$$

Substituting Eq. (7.14) into Eq. (7.13), the position-dependent strain rate due to $n = 21$ STZs under constraint lasting t_c, $0 \le t_c \le t_c^{total}$, becomes:

$$\dot{\gamma}_{21,constr}(y,t_c) = 2c_{21}\gamma_0^c\nu_G \times \exp\left[-\left[\frac{(7-5\nu)}{30(1-\nu)} + \frac{2(1+\nu)}{9(1-\nu)} \times \bar{\beta}^2\right] \times \frac{\mu(\gamma_0^T)^2\Omega_{21}}{kT}\right] \times \sinh\left[\frac{\sigma_{constr}(y,t_c)\gamma_0^T\Omega_{21}}{2kT}\right]. \quad (7.15)$$

In Eq. (7.15), the only parameter expected to change significantly with time is the applied stress $\sigma_{constr}(y,t_c)$, since the constraint imposes a fixed total strain. However, since the apparent elastic strain at the sample surface at the end of the constraining period remains within ~ 25% of its value at the beginning, $\sigma_{constr}(y,t_c)$ will be approximated by the latter value, $\sigma_{constr}(y,t_c) \approx \sigma_{constr}(y,t_c^{total})$. Consequently, $\dot{\gamma}_{21,constr}(y,t_c)$ is approximated as time independent. This is one of the two approximations used to estimate Eq. (7.15). The second approximation is based on the apparent elastic strain, as detailed below.

The position-dependent applied stress at the end of the constraining period, $\sigma_{constr}(y,t_c^{total})$, is proportional to the actual position-dependent elastic strain at that point, $\varepsilon_{el,constr}(y,t_c^{total}) = \varepsilon_{constr}(y) - \varepsilon_{an,constr}(y,t_c^{total})$. It will be approximated by its apparent value, Eq. (7.4), since $\varepsilon_{el,constr}^{app}(d/2,t_c^{total})$ is within ~ 25% of $\varepsilon_{constr}(d/2)$. Therefore,

$$\sigma_{constr}(y,t_c^{total}) \approx \varepsilon_{el,constr}^{app}(y,t_c^{total}) \times \frac{E_0}{2(1-\nu^2)}. \quad (7.16)$$

Substituting the values of all known parameters, listed above, and Eq. (7.16) into Eq. (7.15) yields the approximate position-dependent macroscopic shear strain rate due to $n = 21$ STZs at the end of the constraining period,

$$\dot{\gamma}_{21,constr}^{appr}(y, t_c^{total}) \approx 1.2 \times 10^{12} \times \gamma_0^T \times \exp[-3.20 \times 10^{30} \times (\gamma_0^T)^2 \times \Omega_{21}] \times$$

$$\times \sinh\left[3.37 \times 10^{30} \times \varepsilon_{el,constr}^{app}(y, t_c^{total}) \times \gamma_0^T \times \Omega_{21}\right], \quad (7.17)$$

with Ω_{21} in m^3 here and below. Substituting Eq. (7.17) into Eq. (7.12) yields,

$$\varepsilon_{21,constr}(y, t_c^{total}) = 2 \times 10^6 \times 0.65 \times 1.2 \cdot 10^{12} \times \gamma_0^T \times \exp[-3.20 \times 10^{30} \times (\gamma_0^T)^2 \times \Omega_{21}] \times$$

$$\times \sinh\left[3.37 \times 10^{30} \times \varepsilon_{el,constr}^{app}(y, t_c^{total}) \times \gamma_0^T \times \Omega_{21}\right]. \quad (7.18)$$

Substituting Eq. (7.18) into Eq. (7.11) results in:

$$\varepsilon_{an}^{app}(d/2, t = 4 \times 10^6 \text{ s}) = 3.42 \times 10^{18} \times \gamma_0^T \times \exp[-3.20 \times 10^{30} \times (\gamma_0^T)^2 \times \Omega_{21}] \times$$

$$\times \int_0^1 \sinh[3.37 \times 10^{30} \times \varepsilon_{el,constr}^{app}(d/2, t_c^{total}) \times z \times \gamma_0^T \times \Omega_{21}]\, z dz, \quad (7.19)$$

where $z = 2y/d$. Equation (7.19) is the fitting equation for measured values of $\varepsilon_{an}^{app}(d/2, t = 4 \times 10^6 \text{ s})$ as a function of $\varepsilon_{el,constr}^{app}(d/2, t_c^{total})$ (Fig. 7.4), with γ_0^T and Ω_{21} being the fitting parameters. A Taylor series up to the 11th order (six terms) is used as a good approximation of the hyperbolic sine function.

A two-parameter fit is performed on the entire-range of data simultaneously, with equal weight to all points. It is shown in Fig. 7.5, which displays the data of Fig. 7.4 on logarithmic scales. The fit yields $\gamma_0^T = 0.17$ and $\Omega_{21} = 5.2 \times 10^{-28}$ m^3 with a R-squared value of 0.982. The fit sensitivity to each γ_0^T and Ω_{21} is determined by fixing one at different values and using the other as a single fitting parameter. This yields estimated random errors in γ_0^T and Ω_{21} of ± 3% and ± 6%, respectively. The main approximation has been to express the applied stress that drives anelastic

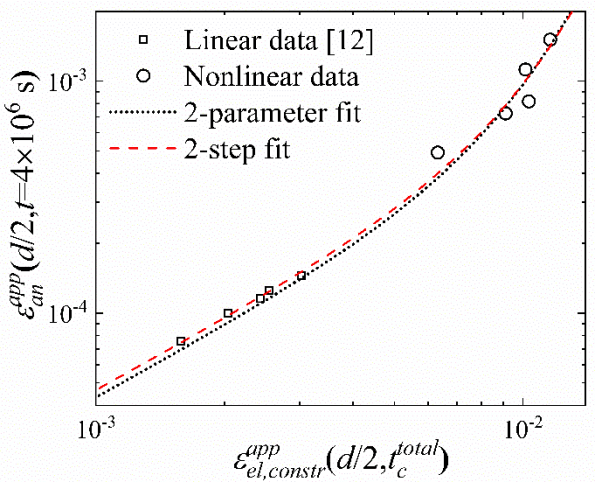

Figure 7.5. Data of Fig. 7.4 on a log-log scale. Comparison between the two-parameter fit (dotted line) and two-step fit (dashed line). The latter yields a better fit for the small-strain data than the former.

deformation as linearly varying in *y* and constant in time. An attempt at fit improvement was made by using the resulting strain distribution to update the applied stress and iterate to obtain a revised fit. The iteration yields a very small change in γ_0^T and Ω_{21}. Moreover, it leads to a slightly worse fit of the (low-scatter) linear portion, and is not considered useful. We conclude that the scatter of the data limits any further improvement in the two-parameter fit.

In Fig. 7.5, it is apparent that the two-parameter fit deviates from the linear portion of the data. Since this portion is more reliable, a revised two-step fit is now employed. For the linear regime, the hyperbolic sine term in Eq. (7.19) can be linearized,

$$\varepsilon_{an}^{app}(d/2\,, t = 4\times10^6\ \mathrm{s}) = 3.84\times10^{48}\times(\gamma_0^T)^2\times\Omega_{21}\times$$

$$\times\exp[-3.20\times10^{30}\times(\gamma_0^T)^2\times\Omega_{21}]\times\varepsilon_{el,constr}^{app}(d/2, t_c^{total}). \qquad (7.20)$$

Fitting Eq. (7.20) to the small-strain data yields a slope of 0.0482, which, when substituted into Eq. (7.20) yields,

$$(\gamma_0^T)^2\Omega_{21} = 1.517 \times 10^{-29}\ \mathrm{m}^3, \tag{7.21}$$

with a random error of only a small fraction of a percent because this term appears in the exponent in Eq. (7.19). Substituting Eq. (7.21) into Eq. (7.19) and fitting the entire range of data yields $\gamma_0^T = 0.18$ and $\Omega_{21} = 4.8 \cdot 10^{-28}\ \mathrm{m}^3$ with random errors of 1.5% and 3%, respectively. Since the error in $(\gamma_0^T)^2\Omega_{21}$ is much smaller, these two errors are strongly correlated. The R-squared value of the fit is 0.982, which equals that for the two-parameter fit.

The implication of these new results, $\gamma_0^T = 0.18$ and $\Omega_{21} = 4.8 \times 10^{-28}\ \mathrm{m}^3$ (~ 29 Al atoms), for Ref. [12] are now discussed. If one assumes $\gamma_0^T = 0.18$ to be independent of STZ size, it can be used to re-calculate the results of Ref. [12]. While the previous quantized hierarchy still stands, the present numerical values result in a volume increment of 2.08×10^{-29} m^3, in contrast to Ref. [12], which was fortuitously close to the volume of an Al atom ($V_{\mathrm{Al}} = 1.66\times10^{-29}$ m^3). This possibly highlights the limitation of the model of Fig. 7.1 and constitutive law of Refs. [12,14] (Eq. 7.1). The present results provide a confirmation of the magnitude of γ_0^T, for which an approximate value of 0.2, obtained from physical analogs [3,4], was used in our prior work.

Interestingly, despite the lower strain and corresponding STZ volume fraction in the present work, the activation volume we obtain, $\gamma_0^T \times \Omega_{21} = 8.6 \times 10^{-29}\ \mathrm{m}^3$, is similar to values obtained from creep in $Pd_{80}Si_{20}$ [14], 10.5×10^{-29} m^3, and from viscosity measurements in undercooled melts, 8×10^{-29} to 1.9×10^{-28} m^3 [22]. Because of the different assumptions in Ref. [22], its STZ volume

values are about a factor of 5 greater than that of the largest active STZ in the present work. Ref. [22] follows Ref. [23] in equating the transformation strain to the universal macroscopic yield strain observed, 0.036. We suggest that the former is greater than the latter for the following reasons: a) Physical analogs (Refs. [3,4]) indicate larger transformation strains, > 0.1. b) This may be explained by the expectation that macroscopic yield involves autocatalytic STZ avalanches, which likely begin at weak spots and for which local strains are higher than the macroscopic strain [12]. When comparing results, one should note that our data were obtained at room temperature, and larger STZs are expected to become active with increasing temperature.

We further reiterate the distinction between data obtained at low strain, when STZs are isolated, and at higher strain, when back stress is lost and STZ interactions with each other are significant. Following Ref. [14], the latter activated flow state is reached for a total volume fraction of ~40 % occupied by STZs, corresponding to macroscopic permanent or anelastic shear strains > 0.033 for our value of γ_o^T. While the present study expands our work into the nonlinear regime, the macroscopic anelastic shear strain is below 0.0060, with corresponding STZ volume fractions that are still small, ≤ 7.2 %. Reported processes such as stress overshoot [24,25] and loss of neighbors [26] occur at far higher strains.

7.6 Conclusions

In conclusion, a method of constraining samples in bending geometry with bending strains up to 0.0155 was developed. The anelastic strain rate was nonlinear in the applied stress due to the high value of the latter. Combining the constitutive law and zero bending moment condition, the

nonlinear regime allows us to determine the transformation shear strain and atomic volume of the largest active STZs independently, which are 0.18 and 4.8×10^{-28} m^3, respectively. The respective random errors, 1.5 % and 3 %, are small because these parameters appear in the exponent in the constitutive law.

7.7 Appendix: Symbol Definitions

"Apparent" strain values below are those determined from curvature by assuming linear variation across the sample. The term "actual" is used to distinguish strain and stress values from their apparent values.

d: sample thickness

y: distance from sample midplane

z: normalized distance from sample midplane, $2y/d$

R: mandrel radius

r_0: initial radius of curvature of the sample before constraint

t: time during unconstrained relaxation after constraint removal

$r(t)$: radius of curvature of the previously constrained section at time t

$\bar{\beta}^2$: dilatancy factor (≈ 1 [14])

ν_G: attempt frequency ($= 10^{13}$ s^{-1} [16])

$\overline{\sigma_{STZ}}$: shear resistance of STZs

μ: shear modulus, equal to $E_0/[2(1+\nu)]$

$\overline{\sigma_{STZ}}/\mu$ = 0.025 [17]

ν: Poisson's ratio (= 0.35 [18])

E_0: Young's modulus (= 48.2 GPa [19])

m = 1,…8 index denoting spectrum peaks

Ω_m: Volume of m-type STZs

ΔF_m: Activation barrier associated with m-type STZs

$n = 13 + m$: number of atoms an m-type STZ comprises. Used as a subscript in Eq. (7.9) and below

τ_n, n = 14,…,21: time constant for unconstrained anelastic relaxation associated with STZs comprising n atoms

c_n: volume fraction of *potential* STZs comprising n atoms

t_c: time under constraint

t_c^{total}: total constraining time, equal to 2×10^6 s

γ_0^T: unconstrained transformation shear strain

γ_0^c: constrained transformation shear strain, equal to $\left[2(4-5\nu)/\left(15(1-\nu)\right)\right]\times\gamma_0^T$

k: Boltzmann constant

T: temperature (= 295.15 K)

Ω_{21}: volume of STZs comprising n = 21 atoms

ΔF_{21}: activation free energy for shear transformation of n = 21 STZs

$\varepsilon_{constr}(y)$: position-dependent constraining strain (Eq. 7.3)

$\varepsilon_{el,constr}^{app}(y, t_c^{total})$: apparent position-dependent elastic strain at the end of the constraining period, obtained from curvature by assuming a linear dependence of the elastic strain on y (Eq. 7.4). Actual value is defined below

$\varepsilon_{an,constr}^{app}(y, t_c^{total})$: apparent position-dependent anelastic strain at the end of the constraining period, obtained from curvature by assuming a linear dependence of the anelastic strain on y (Eq. 7.5). Actual value is defined below

$M(t = 0)$: total bending moment immediately after constraint removal (Eq. 7.6)

$\sigma_u(y, t = 0)$: position-dependent unloading stress immediately after constraint removal (Eq. 7.7)

$\sigma_{constr}(y, t_c^{total})$: position-dependent applied stress at the end of the constraining period (Eq. 7.8)

$\varepsilon_{an,constr}(y, t_c^{total})$: total position-dependent anelastic strain due to all active STZ sizes at the end of the constraining period (Eq. 7.9)

$\varepsilon_{n,constr}^{0}(y, t_c^{total})$: equilibrium position-dependent anelastic strain due to STZs comprising n atoms (n = 14 to 20) at the end of the constraining period

$\varepsilon_{21,constr}(y, t_c^{total})$: position-dependent anelastic strain due to n = 21 STZs, which did not reach mechanical equilibrium, at the end of the constraining period (Eqs. 7.12 and 7.18)

$\varepsilon_{el,constr}(y, t_c^{total})$: actual position-dependent elastic strain at the end of the constraining period

$\dot{\gamma}_{21,constr}(y, t_c)$: actual position-dependent macroscopic shear strain rate due to n = 21 STZs as a function of time under constraint (Eqs. 7.13 and 7.15)

$\dot{\gamma}_{21,constr}^{appr}(y, t_c^{total})$: position-dependent macroscopic shear strain rate due to n = 21 STZs at the end of the constraining period approximated as constant in time (Eq. 7.17)

$\varepsilon_{an}^{app}(y, t)$: apparent position-dependent anelastic strain at time t after constraint removal, obtained from curvature by assuming a linear dependence of the anelastic strain on y (Eq. 7.19)

7.8 References

[7.1] M. F. Ashby, A. L. Greer, *Scr. Mater.* **54**, 321 (2006).

[7.2] H. J. Leamy, H. S. Chen, and T. T. Wang, *Metall. Trans.* **3**, 699 (1972).

[7.3] A. S. Argon, *Acta Metall.* **27**, 47 (1979).

[7.4] P. Schall, D. A. Weitz, and F. Spaepen, *Science* **318**, 1895 (2007).

[7.5] L. Li, E. R. Homer, and C. A. Schuh, *Acta Mater.* **61**, 3347 (2013).

[7.6] M. L. Falk and J. S. Langer, *Annu. Rev. Condens. Matter Phys.* **2**, 353 (2011).

[7.7] M. L. Falk and J. S. Langer, *Phys. Rev. E* **57**, 7192 (1998).

[7.8] C. A. Schuh, T. C. Hufnagel, and U. Ramamurty, *Acta Mater.* **55**, 4067 (2007).

[7.9] E. Orowan, *Proceedings of the First US National Congress of Applied Mechanics ASME* **453** (1952).

[7.10] A. J. Dijkastra and J. Sladekr, *Trans. Metall. Soc. A .I. M.E.* **197**, 69 (1953).

[7.11] C. Zener, Elasticity and Anelasticity of metals, University of Chicago Press, Chicago, 1948.

[7.12] J. D. Ju, D. Jang, A. Nwankpa, and M. Atzmon, *J. Appl. Phys.* **109**, 053522 (2011).

[7.13] M. Atzmon and J. D. Ju, *Phys. Rev. E* **90**, 042313 (2014).

[7.14] A. S. Argon and L. T. Shi, *Acta Metall.* **31**, 499 (1983).

[7.15] J. D. Eshelby, *Proc. R. Soc. A* **241**, 376 (1957).

[7.16] A. S. Nowick and B. S. Berry, Anelastic relaxation in crystalline solids, Academic, New York and London, 1972.

[7.17] H. Kato, H. Igarashi, A. Inoue, *Mater. Lett.* **62**, 1592 (2008).

[7.18] W. H. Wang, *Prog. Mater. Sci.* **57**, 487 (2012).

[7.19] J. M. Freitag, R. G. Koknaev, R. Sabet-Sharghi, M. Kokneava, and Z. Altounian, *J. Appl. Phys.* **79**, 3967 (1996).

[7.20] B. J. Yang, J. H. Yao, J. Zhang, H. W. Yang, J. Q. Wang, and E. Ma, *Scripta Materialia* **61** 423 (2009).

[7.21] J. Das, M. Boström, N. Mattern, Å. Kvick, A. R. Yavari, A. L. Greer, and J. Eckert, *Phys. Rev. B* **76**, 092203 (2007).

[7.22] J. Krausser, K. H. Samwer and A. Zaccone, *Proc. Natl. Acad. Sci.* **112**, 13762 (2015).

[7.23] W. L. Johnson and K. Samwer, *Phys. Rev. Lett.* **95**, 195501 (2005).

[7.24] P. De Hey, J. Sietsma and A. Van den Beukel, *Acta Mater*. 46 (1998) 5873.

[7.25] A. Zaccone, P. Schall and E. M. Terentjev, *Phys. Rev. B* **90**, 140203(R) (2014).

[7.26] M. Laurati, P. Maβhoff, K. J. Mutch, S. U. Egelhaaf and A. Zaccone, *Phys. Rev. Lett.* **118**, 018002 (2017).

CHAPTER 8
Summary and Future Work

8.1 Summary

The present study offers microscopic details of α vs. β relaxation by characterizing STZ spectra over ten orders of magnitude in time constants for MGs with and without a pronounced β relaxation. $La_{55}Ni_{20}Al_{25}$ and $La_{70}(Ni_xCu_{1-x})_{15}Al_{15}$, x=0,1 were investigated. Similar to an Al-based MG in a previous study, a quantized hierarchy of STZs were observed. However, the results suggest that the chemical composition of STZs corresponding to α vs. β relaxation is different, indicated by two regimes of STZ activation volumes, which are not observed in the Al-based MG, where the STZ volume increment between two adjacent STZ types is very close to the atomic volume of Al. The activation-volume increment in the hierarchy is smaller for β relaxation than for α relaxation, suggesting that small atoms (Al for $La_{55}Ni_{20}Al_{25}$, and Al plus Cu/Ni for $La_{70}Cu_{15}Al_{15}$/$La_{70}Ni_{15}Al_{15}$, respectively) dominate the STZs associated with the β relaxation, whereas Cu plus La vs. all atoms possibly participate in STZs associated with the α relaxation for $La_{70}Cu_{15}Al_{15}$ vs. $La_{55}Ni_{20}Al_{25}$ and $La_{70}Ni_{15}Al_{15}$, respectively. The pronounced β peak observed in the normalized loss modulus of $La_{70}Ni_{15}Al_{15}$ but not $La_{70}Cu_{15}Al_{15}$ is a result of *both* a larger volume fraction of fast and small *potential* STZs *and* a smaller volume fraction of slow and large *potential* STZs in $La_{70}Ni_{15}Al_{15}$ vs. $La_{70}Cu_{15}Al_{15}$, and no general correlation exists between the pronounced β peak and macroscopic plasticity.

A detailed microscopic picture of the effect of structural relaxation and cryogenic cycling was also revealed by performing anelastic relaxation measurements on samples aged at room temperature for various amounts of time with or without subsequent cryogenic cycling. The results show that for $La_{55}Ni_{20}Al_{25}$ and $La_{70}(Ni_xCu_{1-x})_{15}Al_{15}$, x=0,1, room-temperature ageing decreases the volume fraction of *potential* large and slow STZs, corresponding to α relaxation, while increasing their corresponding relaxation time constants, which can be explained with the observed increase in Young's modulus during structural relaxation. The dominant structural relaxation effect is on the observed largest and slowest STZs. On the other hand, the small and fast STZs, corresponding to the β relaxation, are not obviously affect by RT ageing. For partially relaxed $La_{70}(Ni_xCu_{1-x})_{15}Al_{15}$, x=0,1, ten cryogenic cycles between liquid nitrogen temperature and room temperature, performed after RT ageing and before anelastic relaxation measurements, reverse the increase in large time constants corresponding to the α relaxation in $La_{70}(Ni_xCu_{1-x})_{15}Al_{15}$, x=0,1, but do not significantly affect the small time constants corresponding to β relaxation. The decreasing time constants after cycling treatment point to a rejuvenation effect. However, the treatment does not significantly affect the volume fraction of the corresponding *potential* STZs. It should be noted that the same effect of cycling treatment was not observed for $La_{70}(Ni_xCu_{1-x})_{15}Al_{15}$, x=0,1, aged at RT for two years or for $La_{55}Ni_{20}Al_{25}$, which indicates that the cryogenic cycling effect changes with the structural state of samples and alloy compositions. Similar observations have been reported in other studies [1,2]. Therefore, one should exercise caution when applying the present result to other alloy systems.

Both the composition difference between STZs corresponding to α vs. β relaxation, and the obvious effects of RT ageing and cryogenic cycling only on the large and slow STZs are consistent

with alloy heterogeneity. Recently, it has been reported that some metallic glasses exhibit heterogeneity on a nanoscale – different domains showing different compositions [3] and moduli [4]. Even though to the author's knowledge, heterogeneity has not been reported for the present alloys, it is important to consider such a possible effect on the present results. In the present study, assuming a single shear modulus value for all STZ types, two regimes of apparent STZ volume vs. *m* (Figs. 4.6 & 6.3) corresponding to α vs. β relaxation were obtained. However, these two regimes are possibly due to anelastic relaxation in different domains with different shear moduli. The observation that only processes corresponding to α relaxation are affected by RT ageing and cryogenic cycling further supports this hypothesis, since the structural relaxation rate is likely composition dependent: Due to the decreasing glass transition temperature with increasing La concentration[*] [1,5], the structural relaxation rate of the La-rich domains is expected to be higher than that of the low-La domains.

In addition to the above-mentioned linear anelasticity, nonlinear anelastic relaxation measurements were performed on $Al_{86.8}Ni_{3.7}Y_{9.5}$ metallic glass by developing a constraining method with a bending strain up to 0.0155. A deviation from linearity of the anelastic strain rate in the applied stress was observed, which is a result of the non-Newtonian viscosity. By combining the constitutive law and zero bending moment condition, the transformation shear strain and atomic volume of the largest active STZs were obtained independently, 0.18 and 4.8×10^{-28} m^3, respectively, with a random error of 1.5% and 3%, respectively. This observation helps rule out the common assumption that the transformation strain is equal to the macroscopic yield strain [6].

[*] T_g is 475 K for $La_{55}Ni_{20}Al_{25}$, and 431 K for $La_{70}Ni_{15}Al_{15}$, and 391 K for $La_{70}Cu_{15}Al_{15}$.

In the present work, the α vs. β relaxation, structural relaxation vs. cryogenic rejuvenation, and nonlinear anelastic relaxation have been studied in terms of STZ properties. The details revealed enable a more comprehensive understanding of the relaxation behavior in MGs. To obtain a more complete picture of the MG relaxation, future works are suggested below.

8.2 Future Work

8.2.1 Structural Relaxation Kinetics

Metallic glasses have a frozen-in melt structure and undergo thermally activated structural relaxation toward an internal equilibrium state. This relaxation is manifested by changes in various properties, e.g., an obvious increase in Young's modulus. In the present study, microscopic details of room-temperature structural relaxation were obtained, e.g., Chapter 4 shows that structural relaxation increases the time constants of the largest and slowest observed STZs while decreasing the volume fraction of the corresponding *potential* STZs the most. In addition, Chapter 5 offers insights on the structural relaxation kinetics, which deserve further investigation since that information would be very helpful for predicting material property evolution as a function of relaxation time.

In Chapter 5, it was observed that the volume fraction occupied by different *potential* STZ types, c_m, evolves differently with RT ageing time, t_a, as shown in Fig. 5.4, reproduced below. The volume fraction occupied by *potential* STZs with time constants larger than the measurement range, c_∞, decreases at a higher absolute or relative rate than that occupied by STZ types corresponding to the last two spectrum peaks, c_5+c_6. In addition, it was noted that while $c_\infty > (c_5+c_6)$ for short

ageing times, the reverse holds for longer ageing times. Therefore, the kinetics of structural relaxation seem different for different STZ types. However, the small number of ageing times and c_m values (c_5+c_6 instead of c_1, …, c_6) in Fig. 5.4 is insufficient to reliably determine the kinetics associated with each STZ type. Therefore, a future plan is suggested as below.

Relaxation time spectra corresponding to larger number of RT ageing times, e.g., equal to or more than ten, will provide useful information on relaxation kinetics. The shortest ageing time should be as short as possible, so that the relaxation kinetics of small and fast STZs could be studied. For the present work, the shortest ageing time was 1.9×10^6 s because of sample shipping time. The longest ageing time should be much longer than 2.9×10^7 s for the present alloys to determine the limiting value of c_m. It should be noted that the time constant of large and slow STZs increases with increasing ageing time. Therefore, an appropriate range of anelastic relaxation measurement

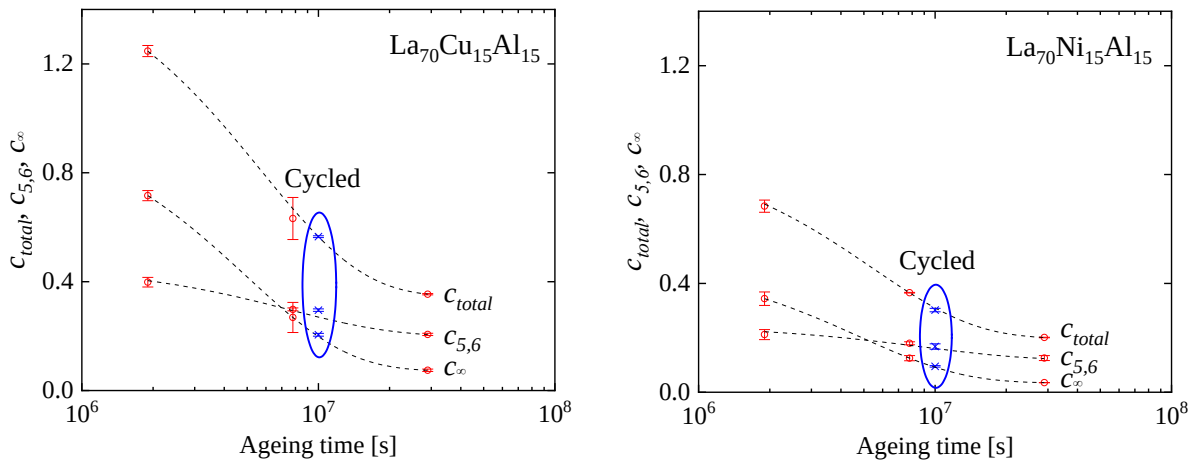

Figure 5.4. c_{total}, the integrated area of the entire spectrum plus the constant in the spectrum fit, $c_{5,6}$, the integrated area of the last two peaks and c_∞ vs. aging time for $La_{70}Cu_{15}Al_{15}$ and $La_{70}Ni_{15}Al_{15}$ MGs. Lines are a guide to the eye.

corresponding to each ageing time should be planned ahead so that the largest and slowest STZs observed in the "youngest" sample can also be observed in the "oldest" sample.

8.2.2 Effect of Ni vs. Cu on Mechanical Behavior in Different Alloy Systems

As mentioned in Chapter 2, in the $La_{70}(Ni_xCu_{1-x})_{15}Al_{15}$, x=0 or 1 system, Ni tends to promote the β relaxation while Cu reduces it. The opposite trend exists in the $Pd_{40}Ni_{10}(Ni_xCu_{1-x})_{30}P_{20}$, x=0 or 1 system. Therefore, it would be instructive to study the effect of Cu vs. Ni in different alloy systems, which may offer valuable details for alloy design. Chapter 6 provides a microscopic characterization of the composition effect on both α and β relaxations in $La_{70}(Ni_xCu_{1-x})_{15}Al_{15}$, x=0 or 1. Two regimes of STZ activation volumes were observed – fast and small STZs, corresponding to β relaxation, more likely include Al plus Cu/Ni for $La_{70}Cu_{15}Al_{15}$/$La_{70}Ni_{15}Al_{15}$, respectively, while all atoms more likely participate in slow and large STZs, corresponding to α relaxation. In addition, the pronounced β relaxation in normalized dynamic-mechanical measurements, observed in $La_{70}Ni_{15}Al_{15}$ but not in $La_{70}Cu_{15}Al_{15}$, is due to both the larger volume fraction of fast and small *potential* STZs and the smaller volume fraction of slow and large *potential* STZs in $La_{70}Ni_{15}Al_{15}$ than $La_{70}Cu_{15}Al_{15}$.

Due to the opposite effect of Ni vs. Cu in $La_{70}(Ni_xCu_{1-x})_{15}Al_{15}$ vs. $Pd_{40}Ni_{10}(Ni_xCu_{1-x})_{30}P_{20}$, x=0 or 1, investigating the latter may offer valuable insights, as detailed below. One difference between the two systems is that all elements in the former are metallic, while the latter is composed of both metal and nonmetal elements. In addition, in $La_{70}(Ni_xCu_{1-x})_{15}Al_{15}$, x=0 or 1, the concentration of La, which has the largest atomic volume, is much greater than those of the other elements. Therefore, it is likely that La is involved in larger and slower STZs, because the volume fraction

of the corresponding *potential* STZs is large and unlikely to exclude La. However, in $Pd_{40}Ni_{10}(Ni_xCu_{1-x})_{30}P_{20}$, x=0 or 1, the concentration of the largest atom, Pd (atomic volume = $0.15\cdot10^{-28}$ m^3), is similar or equal to that of the smaller atoms, e.g., Ni (atomic volume = $0.11\cdot10^{-28}$ m^3) in $Pd_{40}Ni_{40}P_{20}$. It would be instructive to obtain the STZ properties, e.g., STZ volume and volume fraction occupied by *potential* STZs, for the Pd-based alloy, and to examine which element more likely involved in STZs corresponding to α vs. β relaxation. A comparison of STZ properties between $La_{70}(Ni_xCu_{1-x})_{15}Al_{15}$ vs. $Pd_{40}Ni_{10}(Ni_xCu_{1-x})_{30}P_{20}$, x=0 or 1 may offer a more comprehensive understanding of the composition effect on α vs. β relaxation.

In addition, the opposite effect of the same element in different systems indicates that the interaction with other elements plays an important role in the α and β relaxations. Therefore, techniques that are able to provide atomic-scale information, e.g., below one nanometer, may be useful for studying local properties, such as nearest neighbor distribution. Such techniques include atom probe tomography and scanning transmission electron microscopy.

8.3 References

[8.1] S. V. Ketov, Y. H. Sun, S. Nachum, Z. Lu, A. Checchi, A. R. Beraldin, H. Y. Bai, W. H. Wang, D. V. Louzguine-Luzgin, M. A. Carpenter, and A. L. Greer, *Nature* **524**, 200 (2015).

[8.2] J. Ketkaew, R. Yamada, H. Wang, D. Kuldinow, B. S. Schroers, W. Dmowski, T. Egami, and J. Schroers, *Acta Mater.* **184**, 100 (2020).

[8.3] H. B. Yu, X. Shen, Z. Wang, L. Gu, W. H. Wang, and H. Y. Bai, *Phys. Rev. Lett.* **108**, 015504 (2012).

[8.4] P. Tsai, K. Kranjc, K. M. Flores, *Acta Mater.* **139**, 11 (2017).

[8.5] X. D. Wang, B. Ruta, L. H. Xiong, D. W. Zhang, Y. Chushkin, H. W. Sheng, H. B. Lou, Q. P. Cao, and J. Z. Jiang, *Acta Mater.* **99**, 290 (2015).

[8.6] W. L. Johnson and K. Samwer, *Phys. Rev. Lett.* **95**, 195501 (2005).

APPENDIX A

Large-Curvature Sample Constraining and Curvature Measurement After Its Release

A.1 Experimental Setup for Large-Curvature Constraint

In order to conduct mandrel measurements of $Al_{86.8}Ni_{3.7}Y_{9.5}$ in the nonlinear anelastic regime, higher stress was applied by developing a new constraining method with smaller mandrel radius, 0.09 cm or 0.11 cm. The constraining setup is shown in Fig. A.1: A vise was used to apply load on the constraining components, which include a machined device, a mandrel, a neoprene block, and a sample. The sample was placed between the mandrel and neoprene block. The machined device was used to press the mandrel until two constraint-free ends of the sample just touching each other, so that a well-characterized geometry was obtained, as detailed below. A peephole on the side surface of the machined device was used to observe the two touching ends during constraining, and one photograph of the two touching ends of a sample under constraint is shown in Fig. A.1 (top right).

Since only a small section of the sample was under constraint, it would be challenging to directly measure the radius of curvature of the previously constrained section at time t after constraint removal, $r(t)$. The well-characterized geometry allows for a reliable determination of $r(t)$, which is used to determine the anelastic strain (Eq. 7.5). In this appendix, the procedure to determine $r(t)$ in the nonlinear anelastic deformation is detailed.

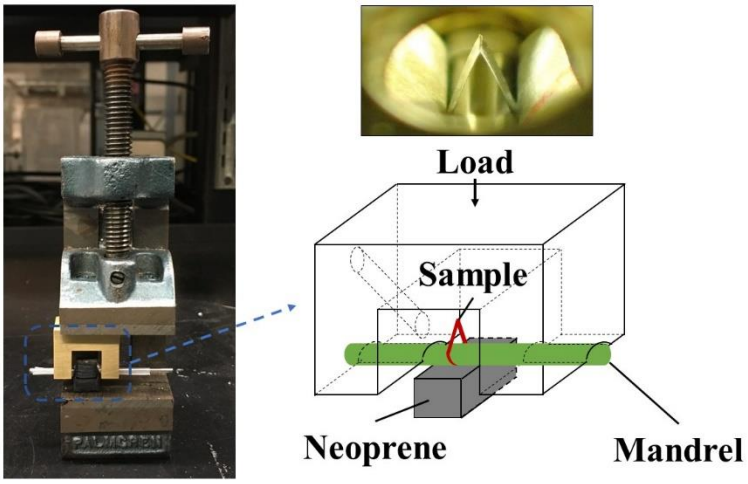

Figure A.1. Constraining setup for the nonlinear-regime mandrel measurement. A vise is used to apply load on the constraining component – a sample placed between a mandrel and neoprene block, and a machined device to press the mandrel until two constraint-free ends of the sample just touching each other. A peephole on the side surface is to observe the two touching ends during constraining. One photograph of the two touching ends of one sample under constraint is shown in the upper-right corner.

A.2 Determination of the Radius of Curvature after Constraint Removal

Figure A.2 illustrates the sample geometry under constraint and after constraint removal (not to scale). The red arc in Fig. A.2a and Fig. A.2b corresponds to the section under constraint and previously constrained section, respectively. The blue lines/curves correspond to the free ends, and

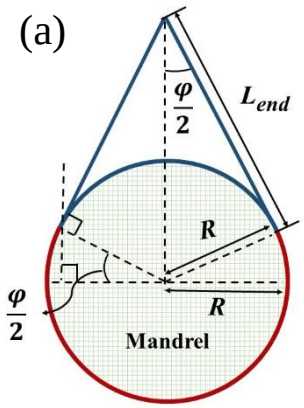

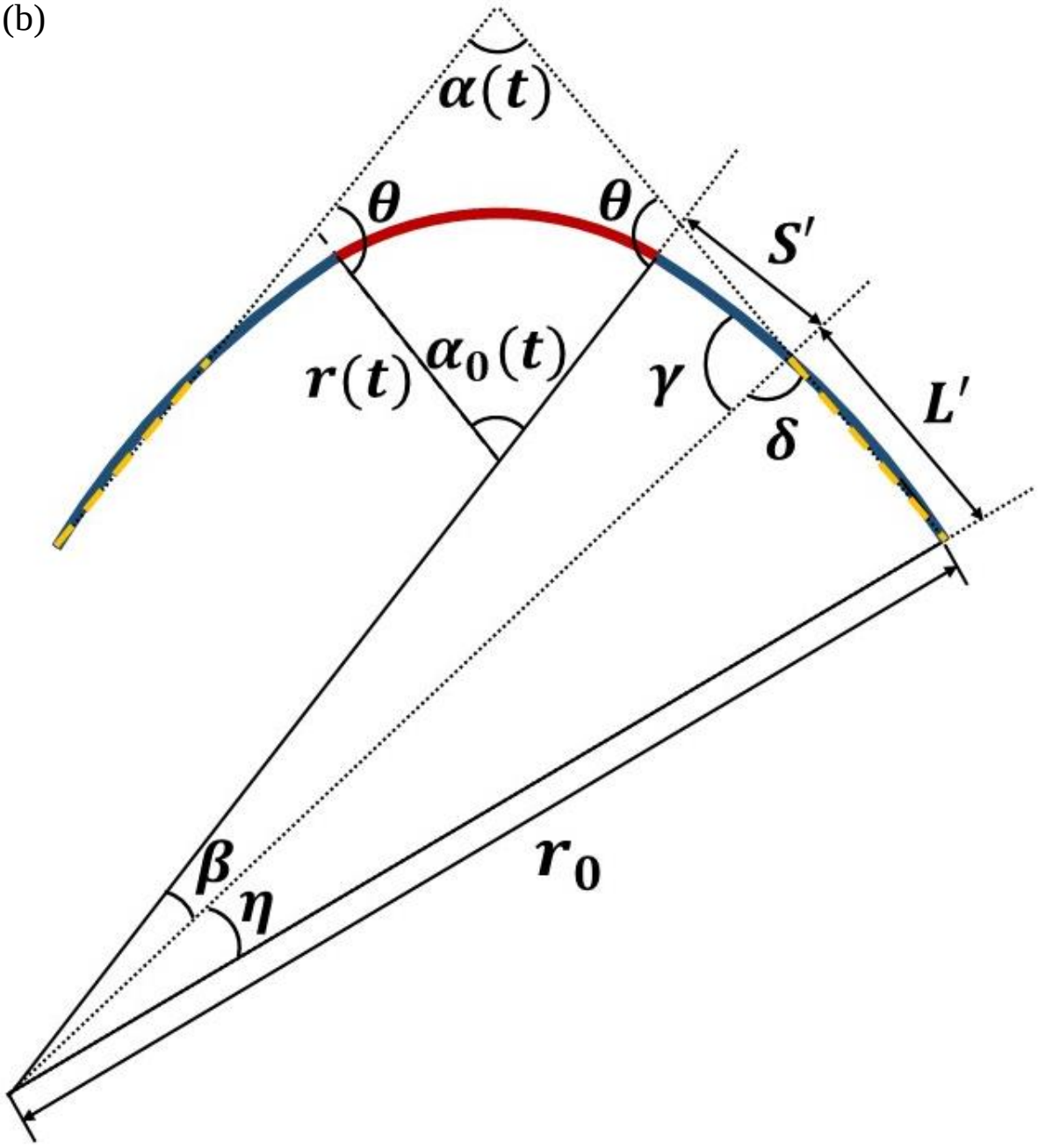

Figure A.2. Sample geometry (a) under constraint (the small curvature of the free ends is neglected), (b) during constraint-free relaxation (not to scale). $\alpha(t)$, the angle between the two free ends, is used to determine the evolution of the radius of curvature of the previously bent section during constraint-free relaxation. The length of the constrained section (red) is equal to $(\pi + \varphi) \times (R + d/2)$, where R is the mandrel radius, and d is the sample thickness. The segment corresponding to the angle β is the part of the free end that is not part of the determination of $\alpha(t)$. Dashed lines are fits to the free ends.

the yellow dashed lines in Fig. A.2b are fits to the ends. Figure A.2a shows the sample geometry under constraint, where the two free ends just touch each other. In Fig. A.2b, one can directly measure $\alpha(t)$, the angle between the two fit lines at time *t* after constraint removal. The segment corresponding to the angle β is the part of the free end that is not part of the determination of $\alpha(t)$. The following details how these are used to determine the radius of curvature of the previously constrained section as a function of constraint-free time.

Firstly, it is noted that the ends are slightly curved, because the sample before constraining has an initial radius of curvature, r_0. Therefore, the length of each end equals,

$$L_{end}{}' = 2r_0 \times \arcsin(L_{end}/2r_0), \quad \text{(A1)}$$

where L_{end} is the length of the line segment corresponding to the end. From Fig. A.2a, the following two relationships can be obtained,

$$2L_{end}{}' + (\pi + \varphi) \times (R + d/2) = L_{total}, \quad \text{(A2)}$$

and,

$$\tan(\varphi/2) = (R + d/2)/L_{end}, \quad \text{(A3)}$$

where $(\pi + \varphi) \times (R + d/2)$ is the total length of the constrained section with φ being the angle between the two free ends, *R* is the mandrel radius, d is the sample thickness, and L_{total} is the total length of the sample. Combining Eqs. (A1), (A2), and (A3) yields the values of $L_{end}{}'$, L_{end}, and φ, since all other parameters can be directly measured.

Figure A.2b shows the sample geometry after constraint removal, where the two dashed lines are fits to the free ends. The radius of curvature of the previously constrained section at time *t* after constraint removal, *r*(*t*), can be obtained from the corresponding angle between the two fit lines, $\alpha(t)$, as detailed below. In Fig. A.2b, the length of the previously constrained section is,

$$r(t) \times \alpha_0(t) = (\pi + \varphi) \times (R + d/2), \tag{A4}$$

where $\alpha_0(t)$ is the angle corresponding to the previously constrained section at time *t* after constraint removal. In Eq. (A4), all parameters on the right-hand side are known. Therefore, $\alpha_0(t)$ is the only parameter that needs to be obtained in order to determine $r(t)$.

Employing the geometry in Fig. A.2b, the following angle relationship is obtained,

$$\alpha_0(t) = 2\pi - 2\theta - \alpha(t) = 2\pi - 2(\beta + \gamma) - \alpha(t). \tag{A5}$$

$\alpha(t)$ is the angle between the line segments corresponding to the free ends. Furthermore,

$$\beta = S/r_0, \tag{A6}$$

where S is the arc length corresponding to the angle β and equal to,

$$S = [L_{total} - (\pi + \varphi) \times (R + d/2) - 2L]/2. \tag{A7}$$

L is the arc length corresponding to the angle η. Substituting Eq. (A7) into Eq. (A6) yields,

$$\beta = [L_{total} - (\pi + \varphi) \times (R + d/2) - 2L]/2r_0. \tag{A8}$$

The angle γ can be obtained as,

$$\gamma = \pi - \delta = \pi - \arccos(L'/2r_0). \tag{A9}$$

where L' is the length of the fit line, and its relationship with L is,

$$L = 2r_0 \arcsin(L'/2r_0). \tag{A10}$$

Substituting Eqs. (A8), (A9), and (A10) into Eq. (A5) yields,

$$\alpha_0(t) = 2\pi - 2(\beta + \gamma) - \alpha(t),$$

$$= 2\pi - 2 \times \left[\frac{L_{total} - (\pi+\varphi)\times(R+d/2) - 2L}{2r_0} + \pi - \arccos\left(\frac{L'}{2r_0}\right)\right] - \alpha(t),$$

$$= -\frac{L_{total}}{r_0} + \frac{(\pi+\varphi)\times(R+d/2)}{r_0} + \frac{2L}{r_0} + 2\arccos\left(\frac{L'}{2r_0}\right) - \alpha(t),$$

$$= 4\arcsin\left(\frac{L'}{2r_0}\right) + 2\arccos\left(\frac{L'}{2r_0}\right) + \frac{(\pi+\varphi)\times(R+d/2)}{r_0} - \frac{L_{total}}{r_0} - \alpha(t). \tag{A11}$$

Substituting Eq. (A11) into Eq. (A4) yields the expression of the time-dependent radius of curvature of the previously constrained section at *t* after constraint removal as,

$$r(t) = (\pi + \varphi) \times (R + d/2)/\alpha_0(t)$$

$$= [(\pi + \varphi) \times (R + d/2)] \times$$

$$\times \left[4\arcsin\left(\frac{L'}{2r_0}\right) + 2\arccos\left(\frac{L'}{2r_0}\right) + \frac{(\pi+\varphi)\times(R+d/2)}{r_0} - \frac{L_{total}}{r_0} - \alpha(t)\right]^{-1}. \tag{A12}$$

In Eq. (A12), φ is obtained from the sample geometry under constraint. R, d, r_0, L', and L_{total} can be directly measured. Therefore, by measuring the angle between the two fit lines at time *t* after constraint removal, $\alpha(t)$, the corresponding radius of curvature of the previously constrained section, $r(t)$, can be determined from Eq. (A12), which yields the corresponding anelastic strain.

APPENDIX B

MATLAB® Code Commands of Image Digitization for Obtaining the Radius of Curvature of Samples During Constraint-Free Relaxation in the Linear Anelastic Regime

B.1 Introduction

In order to study room-temperature anelastic relaxation for a sufficient long time, mandrel measurements were employed, as shown in Fig. B.1. Samples were constrained around mandrels of radii R ranging from 0.348 cm to 0.802 cm for $2.0 \cdot 10^6$ s, then relaxed constraint-free for up to one year. The radius of curvature, $r(t)$, as a function of constraint-free relaxation time, t, was monitored by taking snapshots using a digital camera. The equilibrium elastic strain at the end of the constraining period, and the maximum bending strain at time t after constraint removal, both attained at the surface, were determined from the curvature evolution. Therefore, determination of $r(t)$ is an important step, which affects the strain data quality. In the present study, an automated image analysis and curvature fitting method was developed, which significantly reduces the error in the strain data relative to the visual fitting employed in a previous study. In this appendix, the code commands of image digitization, part of the automated image analysis and curvature fitting method, are explained. They were developed by an undergraduate student Luis Rangel DaCosta. The purpose of the code commands is to convert a sample image taken during constraint-free relaxation into an excel file, which includes the coordinates of the pixels corresponding to the sample. Then, the coordinates can be fitted to obtain the corresponding radius of curvature.

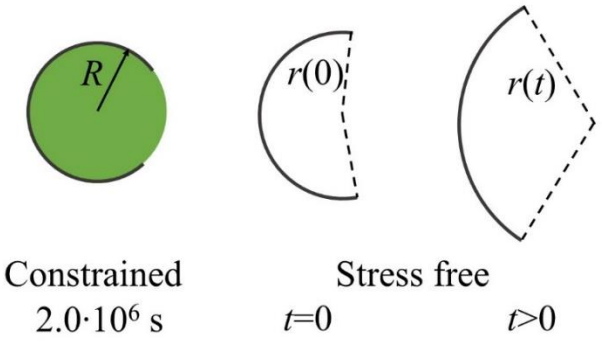

Figure B.1. Schematic illustration of mandrel measurements. A sample was constrained around a mandrel of a radius R for $2.0 \cdot 10^6$ s, then relaxed constraint-free for up to one year. The evolution of radius of curvature at time t after constraint removal, $r(t)$, was monitored.

Compared to the previously employed visual-fitting method [B.1], the code commands not only significantly reduce the error bars in the strain data, but also significantly shorten the fitting time.

B.2 Code Commands and Explanation

In this section, the code commands of image digitization, written in MATLAB®, are explained. Code commands and comments are in Calibri and Time New Roman font, respectively. Code commands mentioned within the comments are placed between asterisk symbols.

The following commands 1) remove all variables from the system memory, 2) remove all text from the command window, 3) set the output format to long fixed-decimal, and 4) prepare the user to input the information of the image file that needs to be analyzed.

```
clear

clc
```

```
format long;

answer = 'Y';
```

The following commands ask the user to input the name and extension of the image file, and write the output file as “image name.csv”

```
while(answer == 'Y')
    answer = 'N';
    nprompt = 'Enter file name: ';
    iname = input(nprompt, 's');
    eprompt = 'Enter file extension: ';
    extension = input(eprompt, 's');
    csv = '.csv';
    oname = strcat(iname, csv);
    iImage = strcat(iname, extension);
```

The following commands open the image file as a matrix, convert the values in the matrix to double precision, and then obtain the matrix size.

```
    image = imread(iImage);
    image = double(image);
```

```
[rows, col, ~] = size(image);
```

The image file is stored in an *x*-by-*y*-by-3 array, where *x* and *y* correspond to the row and column in the matrix, respectively, and 3 corresponds to the intensity of 3 colors, red, blue, or green. The commands below create a grayscale image by averaging the three colors. Since the sample image has the best contrast in green color, green is overweighed, i.e., *7×image(1:1:rows, 1:1:col, 3)* in the present example, so that pixels corresponding to the sample can be easily selected.

```
bwIm2(1:1:rows, 1:1:col) = (image(1:1:rows, 1:1:col, 1) + image(1:1:rows, 1:1:col, 2) +
7×image(1:1:rows, 1:1:col, 3))/3;
bwIm2 = uint8(bwIm2);
```

The commands below count the number of pixels that are below the user-specified threshold brightness, i.e., *180* in the present example.

```
k = 0;
for i = (1:1:rows)
  for j = (1:1:col)
    if bwIm2(i,j) < 180
      k = k + 1;
    end
```

```
    end
end
```

The commands below create storage vectors for pixel locations in *x* and *y*.

```
xVec = 1:1:k;
yVec = 1:1:k;
xVec = xVec';
yVec = yVec';
```

The commands below determine whether the intensity of each pixel is below the threshold brightness. If it is, its coordinate is added to the output file.

```
s = 1;
for i = (1:1:rows)
  for j = (1:1:col)
    if bwIm2(i,j) < 180
    xVec(s, 1) = j;
    yVec(s, 1) = i;
    s = s +1;
```

```
        end
      end
  end
```

The command below uses matrix m to store the coordinate of the pixels corresponding to the sample.

```
m = [xVec yVec];
```

The command below writes matrix m to a CSV file named “oname”.

```
csvwrite(oname,m);
```

The commands below prompts user to run analysis for another image file.

```
repeat = 'Would you like to run another picture? (Y/N): ';
answer = input(repeat, 's');
end
```

B.3 References

[B.1] J. D. Ju, D. Jang, A. Nwankpa, and M. Atzmon, *J. Appl. Phys.* **109**, 053522 (2011).

APPENDIX C

Details of Time-Constant Spectrum Computation from Anelastic Strain Using CONTIN

C.1 Introduction

The present study employs CONTIN [C.1,C.2], a FORTRAN software package for inverse problems, to compute time-constant spectra from anelastic strain data. Based on the standard linear solid model, the fitting equations corresponding to cantilever bending (for short measurement time from ~ 0 s to 200 s) and mandrel measurements (for longer measurement time of up to one year) are,

$$\varepsilon_{an}(t)/\varepsilon_{el}^{0} = c_{\infty} + A \cdot t + \sum_{i=1}^{N_1} \varepsilon_i [1 - \exp(-t/\tau_i)], \quad \text{(C1)}$$

and,

$$\varepsilon_{an}(t)/\varepsilon_{el}^{0} = c_{\infty} + \sum_{i=1}^{N_2} \varepsilon_i \exp(-t/\tau_i), \quad \text{(C2)}$$

respectively. $\varepsilon_{an}(t)/\varepsilon_{el}^{0}$ represents the time-dependent anelastic strain normalized by the corresponding equilibrium elastic strain. N_1 and N_2 are less than the number of experimental data points. c_{∞}, A, and ε_i are fitting parameters. τ_i are fixed, logarithmically spaced relaxation time values. The linear term in Eq. (C1) and the constant term in Eqs. (C1)&(C2) account for processes with time constants longer than the measurement duration. The continuous spectra can be approximated as,

$$f(\tau_i) = \varepsilon_i/\Delta \ln \tau, \quad \text{(C3)}$$

where,

$$\Delta \ln \tau = \ln[\tau_{max}/\tau_{min}]\ /(N-1). \quad \text{(C4)}$$

τ_{min} and τ_{max} are the minimum and maximum relaxation time values, respectively. N equals N_1 or N_2 for cantilever bending or mandrel measurements, respectively. In this appendix, the details of the spectrum computation are provided by 1) giving an overview of CONTIN, and 2) explaining two sample input files (corresponding to cantilever bending and mandrel measurements) for spectrum computation using CONTIN.

C.2 Overview of CONTIN

Input file structure

The input file for CONTIN, written in Fortran, includes control variables for specifying a problem and experimental data. For details, see Section C.3.

Basic equations

Note that all equations in this section are from the CONTIN manual [C.3].

CONTIN was developed by Stephen W. Provencher [C1,C2]. It can convert linear integral equations, e.g., Fredholm equation of the first kind [C.4],

$$y_k \approx \int_a^b K(g,t_k)\, s(g) dg + \sum_{i=1}^{N_L} \beta_i L_i(t_k), \quad k = 1, \dots, N_y, \quad \text{(C5)}$$

to a form,

$$y_k \approx \sum_{j=1}^{N_x} A_{kj} x_j, \quad k = 1, \dots, N_y. \quad \text{(C6)}$$

In Eq. (C5), $K(g, t_k)$ is a kernel function, $s(g)$ is to be determined, and t_k are known independent variables. The second term with unknown β_i and known $L_i(t_k)$ is optional in case additional terms are needed. In Eq. (C6), the y_k are experimental data, which usually contain noise, A_{kj} are known, and x_j are to be determined by using either the trapezoidal or Simpson's rule to approximate the integral in Eq. (C5) [C.5]. Therefore, Eq. (C5) becomes,

$$y_k \approx \sum_{m=1}^{N_g} c_m K(g_m, t_k) s(g_m) + \sum_{i=1}^{N_L} \beta_i L_i(t_k), \quad k = 1, \ldots, N_y, \tag{C7}$$

where the coefficient c_m are always equal to 1 *in the present spectrum computation*, and the g_m, $m = 1,\ldots, N_g$, are grid points. Then, the solution x_j, $j = 1, \ldots, N_x$, in Eq. (C6) equals the set $s(g_m)$, plus the set β_i, $i = 1, \ldots, N_L$ in Eq. (C7). In the present spectrum computation, $K(g_m, t_k)$ corresponds to $1 - \exp(-t/\tau_i)$ in Eq. (C1) and $-\exp(-t/\tau_i)$ in Eq. (C2) for cantilever bending and mandrel measurements, respectively. $s(g_m)$ correspond to the ε_i in Eqs. (C1)&(C2) with the g_m corresponding to the τ_i. t_k, $k = 1,\ldots, N_y$ correspond to experimental time values. The second term in Eq. (C7) becomes a constant plus a linear term or just a constant for cantilever bending or mandrel measurements, respectively.

Constraints can be added on the solution x_j in Eq. (C6), such as,

$$\sum_{j=1}^{N_x} D_{ij} x_j \geq d_i, \; i = 1, \ldots, N_{ineq} \tag{C8}$$

$$\sum_{j=1}^{N_x} E_{ij} x_j = e_i, \; i = 1, \ldots, N_{eq} \tag{C9}$$

where $N_x = N_g + N_L$, and D_{ij}, E_{ij}, d_i, and e_i are specified by users. N_{ineq} and N_{eq} correspond to the number of inequality constraints and number of equality constraints, respectively. In the present work, these are not used.

Solving Eqs. (C5), (C6) or (C7) is an inverse problem, which is often ill-posed — even for a small noise level, there are a large amount of different solutions that all fit the data within the noise level. One example is the linear least-squares solution of Eq. (C6), i.e., x_j satisfies,

$$\text{variance} \equiv \sum_{k=1}^{N_y} w_k \left(y_k - \sum_{j=1}^{N_x} A_{kj} x_j\right)^2 = \text{minimum}, \tag{C10}$$

where w_k are weights specified by the users. However, there is no guarantee that this is the correct answer. On the other hand, CONTIN computes a constrained regularized solution, where x_j satisfies,

$$\text{variance} + \alpha^2 \sum_{i=1}^{N_{reg}} \left(r_i - \sum_{j=1}^{N_x} R_{ij} x_j\right)^2 = \text{minimum}, \tag{C11}$$

subject to Eqs. (C8) and (C9). The second term in Eq. (C11) is a regularizor, the form and strength of which are determined by r_i & R_{ij} and the regularization parameter α, respectively. The advantage of the regularizor is to penalize a solution due to its deviation from expected behavior based on known information, e.g., the expected smooth variation of $f(\tau)$ with τ, or the principle of parsimony, as detailed in Refs. [C.1,C.2].

Execution

To compute a spectrum using CONTIN, the user needs to download the CONTIN source code, which can be found on the website – http://s-provencher.com/contin.shtml. Then, compile the source code to create an executable program by using the Linux command, "gfortran -fmax-stack-var-size=10 -O3 -o contin contin.for", where "contin" is the file name of the executable program, and "contin.for" is the file name of the source code. Subsequently, create an input file named "problem1.in" to specify the problem to be solved, and two example input files corresponding to mandrel measurements and cantilever bending are explained in detail in the next section. At last, run CONTIN with the input file by using the Linux command "./contin <problem1.in" >problem1.out", and an output file named "problem1.out" is generated, which includes solutions corresponding to various regularization parameters and the chosen solution (i.e., the optimal solution selected by CONTIN), all of which are detailed in the next section.

C.3 The Input File for Spectrum Computation Using CONTIN

In this section, the components of the input file, written in FORTRAN, for spectrum computation using CONTIN are detailed. The input file includes 1) control variables (for various purposes, such as specifying input data format, setting up grid points and regularization parameters) and their corresponding values specified for the present study, and 2) experimental time and strain data, which follow the control variables. There are more than 40 control variables, which are set to default values in the CONTIN source code if not specified in the input file. Reference [C.2] shows the default values of all control variables. In principle, only the control variables, the values of which need to be changed, are written in the input file. However, in the following two sections,

some control variables, the values of which are the same as their default values, are written in the example input files and explained due to their importance. The input file should be placed in the same folder with CONTIN software. Below, the code commands in the input file are written in Calibri font, and explanations are in Times New Roman font. The code commands mentioned in the comment are placed between asterisk symbols.

C.3.1 Sample Input File for the Mandrel Measurements

In an input file, the user needs to first input the control variables that specify one problem, then input the experimental data corresponding to the problem. Sometimes, for convenience, the user can create an input file including control variables and experimental data, corresponding to multiple problems. For example, consider two problems –"problem1" vs. "problem2", the control variable and experimental data of which are named "variable1" and "data1" vs. "variable2" and "data2", respectively. The user can write an input file to solve both problems, and the structure of the input file is "variable1" followed by "data1", then "variable2" followed by "data2". For each data set, the control variable *LAST* specifies if it is the last data set to be analyzed or not. *LAST x.000000E+00*, x=1 or -1, correspond to the respective data set being the last one or not. *1.000000E+00* is the value of this variable set by the user, which is in scientific format and equal to $1\times10^{0}=1$. This format applies to the values of all control variables discussed below. Therefore, for "data1", *LAST -1.000000E+00* is used, because it is followed by another data set ("data2") in the same input file, and for "data2", *LAST 1.000000E+00* is used, indicating it is the last data set in the input file. In the present example for mandrel measurements, *LAST 1.000000E+00* is used because there is only one data set in the input file.

LAST 1.000000E+00

NINTT is a control variable that determines how to input N_y and t_k in Eq. (C7), the number of experimental data points and the time values for the spectrum computation, respectively. *NINTT -1.000000E+00* means that the data are to be input directly.

NINTT -1.000000E+00

IQUAD is a control variable that specifies which equation, i.e., Eq. (C5), (C6), or (C7), is to be solved. *IQUAD 1.000000E+00* corresponds to solving Eq. (C6) directly with no quadrature. *IQUAD 2.000000E+00* and *IQUAD 3.000000E+00* correspond to approximating Eq. (C5) with Eq. (C7) using the trapezoidal and Simpson's rule, respectively. In the present example, the trapezoidal rule is employed.

IQUAD 2.000000E+00

IGRID is a control variable that specifies the spacing of the grid point in the quadrature, e.g., τ_i in Eq. (C2). *IGRID 1.000000E+00* means that the grid points are equally spaced on a linear scale. *IGRID 2.000000E+00* means that the grid points are equally spaced in a function defined in the source code. For the spectrum computation, τ_i are equally spaced on a logarithmically scale. Therefore, *IGRID 2.000000E+00* is used with the function in the source code set to be ln (τ_i),

see line number 1211-1223 in the source code which are accompanied by many comment lines for details.

IGRID 2.000000E+00

To set up the quadrature grid points, e.g., τ_i in Eq. (C2), the control variables *NG* and *GMNMX* are employed. *NG* corresponds to the number of τ_i values, e.g., N_2 in Eq. (C2) for the mandrel measurements. *GMNMX 1* and *GMNMX 2* correspond to the τ_{min} and τ_{max} values in Eq. (C4), respectively. In the present example, 50 τ_i values are used, and τ_{min} and τ_{max} are 10 s and 3×10^7 s, respectively.

NG 5.000000E+01

GMNMX 1 1.000000E+01

GMNMX 2 3.000000E+07

All ε_i values in Eq. (C2) are nonnegative. Therefore, a control variable *NONNEG* is employed, which sets constraints on ε_i. *NONNEG 1.000000E+00* constrains ε_i to be nonnegative.

NONNEG 1.000000E+00

To specify the least-squares weights, the control variables *IWT* and *NERFIT* are used. *IWT* corresponds to the "w_k", $k = 1,\ldots, N_y$ in Eq. (C10), which equals $1/{\sigma_k}^2$ with σ_k being the standard deviation of the noise at data point k [C.3]. If the noise is independent of k, then *IWT

1.000000E+00*. *IWT 2.000000E+00* means that $w_k = 1/{\sigma_k}^2 = 1/y(t_k)$ with $y(t_k)$ being the noise-free value of y_k. This applies when the data follow Poisson statistics [C. 6], *IWT 3.000000E+00* means that $w_k = 1/{\sigma_k}^2 = 1/y^2(t_k)$, and *IWT 4.000000E+00* means that the weights are entered directly [C.1]. However, $y(t_k)$ is unknown. Therefore, for *IWT 2.000000E+00* and *IWT 3.000000E+00*, CONTIN performs a PRELIMINARY UNWEIGHTED ANALYSIS to yield an estimation (not the final value) of $y(t_k)$, which is the fit to the y_k and termed "YFIT_k". Then, the improved value of $y(t_k)$ used for computing w_k is $\max\{|\text{YFIT}_k|, \text{ERRFIT}\}$, where ERRFIT is a maximum safety margin to prevent a very large w_k [C.3]. To compute ERRFIT, the user needs to find the *k* at which $|\text{YFIT}_k|$ is minimum. Then, compute residuals (the residual at datum *k* is y_k-YFIT_k) at adjacent*NERFIT* data points centered at *k*. Lastly, ERRFIT equals the root mean square of the *NERFIT* residuals. For example, if *NERFIT* equals 10, then the residuals at 10 data points centered at *k*, are used to compute ERRFIT. For the present spectrum computation with uniform weighting, *IWT 1.000000E+00* is used, and therefore no safety margin is needed, which leads to *NERFIT 0.000000E+00*.

```
IWT         1.000000E+00

NERFIT      0.000000E+00
```

The control variable *NLINF* corresponds to N_L in Eq. (C7), which is the number of coefficients in the $\sum_{i=1}^{N_L} \beta_i \, L_i(t_k)$ term. For the mandrel experiment, this term consists of a constant only, so *NLINF* is one.

```
NLINF       1.000000E+00
```

NENDZ is a variable that controls the behavior of the solution at the edges of the grid. It includes two parameters, *NENDZ 1* and *NENDZ 2*, which are the number of extra zeros before the first data point (e.g., $i = 1$ in Eq. (C2)) and after the last point (e.g., $i = N_2$ in Eq. (C2)) of the solution, respectively. When extra zeros are added, the solution tends to approach zero more smoothly at the respective edge of the grid. For the mandrel experiment, it is unlikely that the spectrum peak with time constants shorter than the first measurement time will be revealed with the technique used. Therefore, *NENDZ 1* is set to its default value, which is 2, as *NENDZ 1 0.000000E+00*, and this command is not written in the input file. Since there are spectrum peaks with larger time constants than those observed, no extra zero will be placed after ε_{N_2}, and therefore *NENDZ 2 0.000000E+00* is used.

```
NENDZ    2  0.000000E+00
```

As mentioned above, CONTIN computes constrained regularized solutions by minimizing the sum of the variance and regularizor (Eq. (C11)), and the strength of the regularizor is determined by the regularization parameter, α. In order to determine the optimal spectrum, CONTIN first computes spectra for a range of logarithmically spaced α values on a coarse grid. Then, it selects a region of interest and computes spectra for a range of logarithmically spaced α values corresponding to the region of interest on a fine grid. Lastly, CONTIN determines the optimal spectrum by using a default selection criterion. The whole procedure is detailed below.

To specify the regularization parameter, α, on both coarse and fine grids, the control variables *RSVMNX* and *NQPROG* are employed. *RSVMNX* includes four values, the first/last two of

which specify the α ranges on the coarse/fine girds, respectively. *NQPROG* includes two parameters, *NQPROG 1* and *NQPROG 2*, which correspond to the number of α values on coarse and fine grids, respectively. In the default setting, CONTIN first scans *NQPROG 1* α values on a coarse grid, e.g., six (i.e., *NQPROG 1 6.000000E+00*) α values from 10^{-8} to 10^{2}, which are 10^{-8}, 10^{-6}, 10^{-4}, 10^{-2}, 10^{-0}, 10^{2}, and computes the corresponding solution. Then, CONTIN determines the region of interest, defined by the two adjacent α values on the coarse grid, based on the default selection criterion in CONTIN – the PROB1 TO REJECT criterion. The PROB1 TO REJECT value of each solution (and therefore of each α value) is a value obtained from Fisher's *F*-distribution function associated with that solution [C.3]. Two α values selected, the PROB1 TO REJECT values of which are closest to 0.5. For example, if the PROB1 TO REJECT values corresponding to $\alpha = 10^{-8}$, 10^{-6}, 10^{-4}, 10^{-2}, 10^{-0}, 10^{2}, are 0, 0, 0.4, 0.6, 0.7, 0.8, 1, respectively, CONTIN chooses the range $\alpha = 10^{-4}$ to 10^{-2} as the region of interest, due to PROB1 TO REJECT values being closest to 0.5. Subsequently, CONTIN scans *NQPROG 2* α values over a fine grid between $\alpha = 10^{-4}$ and 10^{-2}, e.g., six (i.e., *NQPROG 2 6.000000E+00*) α values, to determine the CHOSEN SOLUTION, the PROB1 TO REJECT value of which is closest to 0.5.

When the PROB1 TO REJECT criterion does not yield a reasonable result as judged by the user performing the computation, the two control variables *RSVMNX* and *NQPROG* need to be manually modified, as detailed below. For spectrum computation, the first and second values after *RSVMNX*, corresponding to the lower and upper limit of the coarse grid, are always set to *1.E0*, equal to $1\times10^{0}=1$, which means that the coarse grid starts with a very small α value and ends with a very large α. Then, in the output file, the user needs to identify two α values on the coarse grid,

named "α_{low}" and "α_{upper}", the spectra associated with which are more physically meaningful than others. Therefore, the region of interest can be determined with "α_{low}" and "α_{upper}" being the lower and upper limit of the fine grid. However, the third and fourth input values after *RSVMNX*, i.e., *3.1E+6* and *1.38E-7* in this example, are not simply equal to "α_{low}" and "α_{upper}". To determine the third and fourth values, the user needs to, firstly, in the output file, find the two values of the parameter named "ALPHA/S(1)" (highlighted in Fig. C1) corresponding to "α_{low}" and "α_{upper}", which are termed "α_1" and "α_2", respectively. The "ALPHA" (highlighted in Fig. C1) equals α_{low} or α_{upper}, and "S(1)" is a scaled singular value and equal to the first value in the "SINGULAR VALUES" section of the output file. For details of "S(1)", refer to Sec. 3.5 in Ref. [C.1]. Then, the third and fourth values after *RSVMNX* equal $\alpha_1/(1.49 \times 10^{-15})$ and α_2, respectively.

```
      Interface input file

    ALPHA     ALPHA/S(1)     OBJ. FCTN.       VARIANCE       STD. DEV.    DEG FREEDOM    PROB1 TO REJECT
* 3.21E-10     1.49E-15    1.53642E-06    1.53642E-06      2.095E-04         18.000              0.000

 ORDINATE    ERROR  ABSCISSA
0.000E+00  2.4D-18  1.00E+01X
1.400E-03  3.6D-02  1.47E+01.X.........................
1.737E-02  3.1D-02  2.15E+01.............X.....................
0.000E+00  1.3D-17  3.15E+01X
0.000E+00  3.0D-17  4.62E+01X
3.172E-02  1.1D-02  6.77E+01               .........X........
0.000E+00  4.2D-17  9.92E+01X
0.000E+00  6.7D-17  1.45E+02X
2.065E-02  2.6D-02  2.13E+02................X.................
3.530E-02  2.7D-02  3.12E+02      ..................X.....................
0.000E+00  2.0D-16  4.58E+02X
0.000E+00  2.3D-16  6.71E+02X
8.795E-04  2.2D-02  9.84E+02X.................
4.107E-02  1.8D-02  1.44E+03                 ..............X.............
0.000E+00  3.5D-16  2.11E+03X
0.000E+00  4.6D-16  3.10E+03X
0.000E+00  5.2D-16  4.54E+03X
0.000E+00  3.6D-16  6.66E+03X
2.188E-02  1.3D-02  9.76E+03       .........X..........
1.431E-02  1.3D-02  1.43E+04 .........X..........
0.000E+00  6.8D-16  2.10E+04X
0.000E+00  5.8D-16  3.07E+04X
```

Figure C.1. Screenshot of one sample output file.

RSVMNX

1.E0 1.E0 3.1E+6 1.38E-7

NQPROG 1 6.000000E+00

NQPROG 2 6.000000E+00

IFORMY controls the input format for the y_k in Eq.(C7), corresponding to the strain data in the spectrum computation. *1E11.4* represents the format and follows one Fortran variable format type – the E format, the syntax of which is "rEw.d". This format allows the user to enter the data in scientific form. "E" is the exponent of 10, "w" is the total number of decimal places and "d" is the number of decimal places to the right of the decimal point. "rEw.d" "r" being an integer, is equivalent to repeating "Ew.d" "r" times.

IFORMY

(1E11.4)

IFORMT controls the input format for the t_k in Eq.(C7). *1E11.4* has the same meaning as that explained above.

IFORMT

(1E11.4)

END

NY corresponds to the number of experimental data points, which is *66* in this example.

NY 66

The section below inputs the experimental time data first, 60 points from *2.2000E+01* to *1.5044E+07* in the present sample, then it inputs the corresponding strain values, from *3.5227E-01* to *8.6018E-02*. The format of each datum follows *1E11.4* as defined above. Based on the number of data points (*NY 66* above), these are identified.

2.2000E+01

…

1.5044E+07

3.5227E-01

…

8.6018E-02

C.3.2 Sample Input File for the Cantilever Bending

Below is a sample input file for the cantilever bending measurement. Note that the code commands that are essentially the same as that for mandrel measurements have the same purpose, and explanations are only added below only for features that are different.

```
LAST        1.000000E+00

NINTT       -1.000000E+00

NG          5.000000E+01

IQUAD        2.000000E+00
```

The control variables *GMNMX 1* and *GMNMX 2*, which correspond to τ_{min} and τ_{max} values in Eq. (C1) for cantilever measurements, are 0.0015 s and 400 s, respectively.

```
GMNMX    1   1.500000E-03

GMNMX    2   4.000000E+02
```

```
IWT         1.000000E+00

NERFIT      0.000000E+00
```

The control variable *NLINF* specifies the number of the linear and constant terms in Eq. (C1), which equals 2. Therefore, *NLINF 2.000000E+00* is used.

NLINF 2.000000E+00

IFORMT

(1E11.4)

IFORMY

(1E11.4)

PRY is a control variable which specifies whether to print the experimental data, i.e., time and strain values, in the output file or not. *PRY 1.000000E+00* or *PRY -1.000000E+00* correspond to printing or suppressing this output, respectively. The default value of *PRY* is 1. However, due to the large number of data points of the cantilever measurement, ~ 60000, * PRY -1.000000E+00* is employed.

PRY -1.000000E+00

The control parameter *IPLRES 2* specifies whether to plot the weighted residuals or not. *IPLRES 2* has four options, where are *IPLRES 2 x.000000E+00*, x=0,1,2,3, corresponding to never plotting the residuals, plotting them only after plotting the Peak-Constrained Solutions [C.3] (not employed in the spectrum computation), plotting them just before plotting the CHOSEN SOLUTION (the solution CONTIN automatically selected based on its default setting, see Section C.3.1), and plotting them after plotting every solution, respectively. For the cantilever

measurement, due to the large amount number of data points, the weighted residuals are not plotted, and therefore *IPLRES 2 0.000000E+00* is used.

```
IPLRES   2    0.000000E+00
```

The control parameter *IPLFIT 2* determines whether to plot the fit to the data or not. The options and their corresponding explanation are the same as those of *IPLRES 2* as detailed above. For the cantilever measurement, due to the large amount number of data points, the fit to the data is not plotted, and therefore *IPLFIT 2 0.000000E+00* is used. (If a plot is desired, one uses a different value, e.g., *IPLFIT   2   3.000000E+00*.)

```
IPLFIT   2    0.000000E+00


NONNEG       1.000000E+00
IGRID        2.000000E+00
NQPROG    2   6.000000E+00
END
```

NY corresponds to the number of data points of cantilever bending, which is *59990* in this example.

```
NY    59990
```

Then, the data are entered as detailed above for the mandrel measurements.

C.4 References

[C.1] S. W. Provencher, *Comput. Phys. Commun.* **27**, 213 (1982).

[C.2] S. W. Provencher, *Comput. Phys. Commun.* **27**, 229 (1982).

[C. 3] S. W. Provencher, *CONTIN Users Manual, EMBL Technical Report DA05,* European Molecular Biology Laboratory (1982)

[C.4] L. Landweber, *Amer. J. Math.* **73**, 615 (1951).

[C.5] D. Cruz-Uribe and C. J. Neugebauer, *J. Inequal. Pure Appl. Math* **3** (2002).

[C.6] P. F. Price, *Acta Cryst.* **A35**, 57 (1979).